NTNU
Norwegian University of
Science and Technology

Surface Acoustic Wave Acoustophoresis for Microfluidic Based Micron and Submicron Particle Separation

Ole-Andreas Kvivik Kavli

Preface

The work presented in this book is a Master thesis in biophysics, conducted at the Department of Physics at the Norwegian University of Science and Technology (NTNU). The thesis was carried out within the international Master of Science (MSc) programme in physics. This work started in August 2015 and ended in Mai 2016, and has been carried out under guidance of professor Bjørn Torger Stokke and PhD candidate Jonas Myren Ribe.

During my bachelors degree in physics at NTNU I came in contact with Jonas and PhD candidate Armend Gazmeno Håti. They were so kind to sit down and talk to me about their research within the Microfluidics Research Group at Department of Physics. I contacted their supervisor Bjørn Torger about the possibility of doing my master thesis as a part of Jonas' research on Lab-on-a-chip technology for Exosome Isolation. The first year of my MSc in physics at NTNU I studied abroad at the University of California, Berkeley (UCB) where I studied microfluidics and BioMEMS technology, inspired by my talks with Jonas and Armend. To gain more experience within the field I worked as a research assistance at Luke P. Lee's bioPOETS laboratory, under supervision of Professor Lee and Jun Ho Son. After returning to NTNU I worked on my master thesis together with Jonas, as part of his PhD research.

First and foremost I would like to thank Jonas for being a part of his project and for everything he has taught me throughout this work. I would like to give a special thanks to Armend and Bjørn Torger for letting me become part of the Microfluidic Research Group. I would also like to thank Nils Refstrup Skov for his contribution to the project, and everyone who have guided me through my studies and research as mentors, friends and family.

Trondheim, May 22, 2016

Ole-Andreas Kvivik Kavli

Sammendrag

Eksosomer er små nanopartikler som skilles ut fra celler og antas å være viktige innen tidlig diagnostikk av blant annet kreft. Interessen for å kunne separere ut slike partikler er derfor stor innenfor point-of-care diagnostikk, men det er mange begrensninger som må overkommes for å kunne lykkes med separasjon av exosomes fra blodprøver. Motivasjonen for dette masterstudiet er å undersøke hvordan akustisk overflatebølge (SAW) basert akustoforese kan benyttes for separasjon av nanopartikler fra en bi-dispers partikkelsuspensjon (mikro- og nanopartikler) i en mikrofluid enhet.

For en mikrofluid kanal plassert mellom to SAW generende interdigitale transdusere (IDTs) vil stående akustiske overflatebølger (SSAW) oppstå i bølgens forplantningsmedium, og trykk-noder og -antinoder vil dannes inne i væsken. Som et resultat vil akustiske stråling fra den stående bølgen påvirker partikler i væsken, avhengig av partikkelstørrelsen og bølgens frekvens. Forskjellige IDT design ble fabrikkert, deres frekvensrespons ble målt, og sammen med en mikrofluidkanal ble de implementert til en akustoforese enhet. Effekten av akustoforese med forskjellige IDT design ble undersøkt for separasjon av bi-disperse polystyren-partikkelprøver.

Målinger av frekvensresponsen for de ulike IDT designene viser til den IDTen med reflektor struktur og 100 μm bølgelengde som den med best effekt. 3,0 μm polystyren partikler ble sortert fra 0,5 μm partikler ved å bruke dette designet, mens 1,0 μm og 0,2 μm polystyren partikler ble kun delvis sortert. 1,0 μm partikler ble sortert ut ved å bruke en IDT med en 50 μm bølgelengde, mens 0,2 μm partiklene ble derimot ikke sortert i samme forsøk. Forskyvninger mellom microfluidic kanalen og IDTene under fabrikasjonen fører til en endring av plasseringen på trykk-nodene og -antinodene i forhold til kanalen. Resultatene for separasjonsenhetene ser lovende ut for utvikling av en potensiell on-chip separasjonsenhet, men for å fortsette med videre studier på SSAW basert separasjon av nanopartikkler må forskyvningen mellom mikrofluid kanalen og IDTene under fabrikasjonen minimeres.

Abstract

Microvesicles secreted from our cells referred to as exosomes contain vital information on our health status and are believed to revolutionize early diagnosis. Therefore, separation of such particles is a growing field within point-of-care diagnostics, however, there are yet many limitations that need to be addressed in able to successfully separate exosomes from blood samples. The motivation for this study is to investigate how surface acoustic waves (SAW) based acoustophoresis may be used for separation of submicron particles from a bidispers particle suspension (micron and submicron sized particles) in a microfluidic device.

For a microfluidic channel aligned between two SAW generating interdigital transducers (IDTs) standing surface acoustic waves (SSAW) will form in the SAW propagating medium, generating pressure nodes and anti-nodes inside the fluid. As a result, acoustic radiation forces will affect particles submerged in the fluid, depending on the particle size and the SAW frequency. IDT designs with different pitch, resonance frequency and reflector structures were fabricated; their frequency response were measured, and they were implemented together with a microfluidic channel to form an acoustophoresis device. Specifically, the effect of acoustophoresis and various IDT designs were investigated for the separation of bidisperse polystyrene particle sample.

Frequency response measurements of the various IDT designs favors the $100\,\mu m$ pitch IDT with reflectors. $3.0\,\mu m$ polystyrene particles were successfully separated from $0.5\,\mu m$ particles using the $100\,\mu m$ pitch IDT design, while $1.0\,\mu m$ and $0.2\,\mu m$ polystyrene particles were only partially separated. The $50\,\mu m$ pitch IDT device did successfully sort out the $1.0\,\mu m$ particles, however, the $0.2\,\mu m$ particles were not centered in the channel and the separation was only partially successful. Misalignments between the microfluidic channel and the IDTs during fabrication proved to be the main challenge for reproducible results, altering the locations of the pressure nodes and anti-nodes in the channel. The results for the devices are promising as a potential on-chip separation technique, however, to continue with further studies on submicron particle separation by SSAW the alignment accuracy has to be improved.

Acronyms

LOC Lab-On-A-Chip

POC Point-Of-Care

SAW Surface Acoustic Wave

SSAW Standing Surface Acoustic Wave

PDMS Polydimethylsiloxane

LiNbO$_3$ Lithium Niobate

IDT Interdigital Transducer

FIDT Focused Interdigital Transducer

SPUDT Single-Phased Unidirectional Transducers

IRB Image Reversal Bake

μ Fluid Viscosity [Pa·s]

ρ_f Fluid Density [kg/m^3]

ρ_s Solid Density [kg/m^3]

ν Solid Phase Velocity [m/s]

ν_f Fluid Phase Velocity [m/s]

$\mathbf{w}_f$ Electrode Finger Width [μm]

f_0 SAW Center Frequency [MHz]

ϕ Acoustic Contrast Factor

V_p Particle Volume [m^3]

p_0 Pressure Field Amplitude [Pa]

λ SAW wavelength [μm]

β_m Compressibility of Medium [Pa^{-1}]

β_f Compressibility of Fluid [Pa^{-1}]

k Wave Vector [m^{-1}]

θ_R Rayleigh Angle [°]

α Radiation Attenuation Coefficient [m^{-1}]

Contents

List of Figures

List of Tables

1 | Introduction

Extracting and manipulation of micron and submicron particles are used in a broad range of research. Especially within medicine and biophysics, extraction of small biomarkers from large samples of biofluids is a crucial and important step in molecular diagnostics. With novel discoveries within research on biological particles, and mapping of genetic variations that lead to specific diseases, submicron biomarkers have become an essential key for early detection of diseases [1, 2]. One example is the exosome, an extracellular vesicle that ranges in size from 10 nm to 200 nm [3, 4, 5]. Cell derived miRNA and proteins, which have shown to be important and accurate biomarkers for diagnosing and early detection for a range of diseases [6, 7, 8], are packed into the protective environment of the exosome [9]. These microvesicles are found freely existing in blood, saliva and other bodily fluids and can hence be extracted in a non-invasive manner. Early detection of diseases have proven to be an important factor for increased survival rate among a range of severe disease, especially for cancer patents [10]. Hence, exploiting exosomes for use within diagnostics purposes might open up to early detection and treatment of severe diseases.

With advancement and development within molecular diagnostics and microscale solutions, lab-on-a-chip (LOC) technology for point-of-care (POC) diagnostics is a rapidly growing field [11]. As an indicator, the global microfluidics market was valued at $3 Billion in 2015 and is expected to grow, mainly driven by the rising demand for microfluidic integrations in POC technology [12]. Scaling down fluidic processes to the microscale offers many significant advantages within LOC devices, for example decreasing the size of the system and samples and chemical reaction time [13, 14]. The development within LOC POC diagnostics devices has opened up to possibilities of inexpensive, user friendly and accurate devices for diagnosing diseases, as well as monitoring treatment and patience responses without the need for visiting hospital or sending results to laboratories [15, 16]. The

modern widespread home pregnancy test is an example of how microfluidics and molecular diagnostiscs have been used to developed an inexpensive, user friendly and personalized POC test.

The ExoChip developed by Kanwar *et. al.* [17], the ExoSearch Chip developed by Zhao *et. al.* [18] and the microfluidic device for immunoisolation and protein analysis of circulating exosomes developed by He *et. al.* [19] are all examples of rapid molecular diagnostic LOC technology exploiting exosomes as biomarkers. However, all of these solutions require highly enriched blood plasma as the exosome containing input sample. The most common technique for extracting blood plasma from whole blood is by centrifugation; a time consuming process which requires a laboratory and trained personnel to operate, and do not always result in high purity isolation of microvesicles [20]. Hence, one can discuss if these solutions are lab-on-a-chip solutions or currently chip-in-a-lab devices [21]. To meet the needs required for a fully functional POC device one need to integrate extraction and detection LOC technology into one, stand-alone device.

There are many existing LOC filtration devices which can be implemented with one of the devices mentioned above. There exists micro sized filters that can filter out micrometer sized particles and cells [22, 23], however, a high pressure field will put a lot of force on the particles trapped in the filter and may lyse cells, contaminating the sample with cell debris or clogging the device. The hemolysis-free blood plasma separation device developed by Son *et. al.* [24] is an example of filtration device without a physical filter, using gravity-assisted cellular sedimentation to filtrate out cells from whole blood. However, this technique requires low pressure conditions and do not meet the requirements as a continuous flow separation device. Zeming *et. al.* real-time modulated nanoparticle separation device show good results in high throughput particle separation using microfluidic technology [25]. The microfluidic device filtrate particles without using any applied force field, by using determined lateral displacement (DLD) microfluidics they have shown to successfully separate particles down to 0.6 µm. For smaller particles diffusion becomes challenging and the group uses a EDL electrostatic model to successfully separate particles down to 51 µm by adding different concentrations of ionic NaCl fluids as buffer. However, sorting of submicron particles below 0.5 µm from blood samples may be problematic for this device since the concentration of NaCl in blood alone is much higher than the one used to decrease the sorting size cut-off. Hence, there are many LOC devices for particle separation, however, many there are still many limitations for separation at the submicron scale.

Label free separation of particles by surface acoustic wave (SAW) acoustophoresis has been successfully demonstrated for filtration of micron sized particles [26, 27, 28, 29]. Destgeer *et. al* claims to successfully have used high frequency traveling SAW for high throughput submicron separations [30]. However, by submicron separation he refers to separating particles with a difference in size of less than one micron. Their device was not used to affect submicron particles, but successfully separated 3.0 μm particles from 3.2 μm particles with a generated frequency of 200 MHz. Shi *et. al.* have proven standing SAW acoustophoresis to be a successful technique in continuous particle separation by size [31]. They managed to separate 0.89 μm particles from 4.17 μm particles. Hence, SAW based acoustophoresis shows promising results as a filtration continuous separation technique for micron and submicron particle separation. In addition the SAW generating interdigital digital transducers (IDTs) and microfluid channels requires little space and can be implemented into a LOC device for POC purposes. The standing surface acoustic waves sort particles purely based on their size and density, so the particles do not need any other labeling, charge, magnetic or biological chaperons. Hence, any buffer solution should not affect the particle sorting. Even though SAW acoustophoresis is a promising technique for micron sized particle separation, little research have been done to separate particles smaller than 0.9 μm. To be able to use SAW acoustophoretic as a mean to separate exosome sized particles from micron sized cells, SAW devices have to be able to separate 0.2 μm particles from larger micron sized particles.

The motivation for this thesis is to investigate, develop and test how acoustophoresis can be used in continuous flow separation to separate micron sized particles from submicron sized particles. The aim is to characterize separation of 3.0 μm particles from 0.5 μm particles and gradually work towards separating 1.0 μm particles from 0.2 μm particles. We will also look into what implications that arise when targeting smaller particles and how IDT design and frequency of the SAWs can play a role in submicron particle manipulation. We also will look into how SAW acoustophoretics can be used as a tool for on-chip separation of micron and submicron particles.

2 | Microfluidics

2.1 Continuum fluid mechanics

A fluid is described as a material that deforms continuously when a nonuniform stress of any magnitude is applied to it. In a continuum description of a fluid flow we look at the motion of individual molecules that makes up the fluid. In continuum mechanics we can describe the velocity and the pressure of the fluid as a function of space and time.

2.2 Newtonian fluid

A fluid where the viscosity μ is independent of the stress, so that the rate of shearing strain is linear to the viscous stress $\tau = \mu \dfrac{dU}{dy}$, is said to be Newtonian. U is the absolute value of the velocity vector $\boldsymbol{U}$ to the fluid.

2.3 Navier-Stokes Equation

The Navier-Stokes equation for a Newtonian fluid is given as:

$$\rho_f \frac{d\mathbf{U}}{dt} + \rho_f \mathbf{U} \cdot \nabla \mathbf{U} = -\nabla p + \nabla \cdot \mu \nabla \mathbf{U} + \sum_i f_i \tag{2.1}$$

where ρ_f is density of the fluid, $\boldsymbol{U}$ is the velocity field of the fluid, μ is the viscosity of the fluid, ∇p is the pressure gradient in the system and f_i is any additional force acting on the fluid. For a suspension of particles in fluid, the additional forces acting on the particles in the fluid will usually be limited to the gravitational force $f_g = \rho_f\,g$, where g is the gravitational constant, only acting in the z-direction. Since μ is a constant in our case, the relation $\nabla \mu \nabla \mathbf{U} = \mu \nabla^2 \mathbf{U}$ holds.

2.4 Laminar Flow

In the continuum model of fluid mechanics, laminar flow is one specific regime. Fluid with a laminar flow regime will have a large momentum diffusion rate, compared to convection rate. There will be no turbulence in a fluid with laminar flow, and the fluid will follow distinct sheets or lamina, referred to as fluid streamlines.

The dimensionless Reynolds number *Re* characterize the flow regime of a fluid system. In a fluid with absolute velocity U, density ρ_f, viscosity μ, and in a system with a characteristic length L, the Reynolds number is defined as:

$$Re = \frac{\rho_f U L}{\mu},$$
(2.2)

which can be deduced from a dimensionless version of the Navier-Stokes equation [32]. *Re* describes the relations between inertial forces and viscous forces; dominant inertial forces compared to viscous forces yields a high Re and vice versa.

Due to this, *Re* also describes the flow characteristics of a fluid system. At *Re* lower than 2300 laminar flow is obtained and viscous forces will be dominant [33].

Stokes flow is a type of fluid flow where viscous forces are dominant compared to advective inertial forces so that $Re \ll 1$ [32]. For microfluidic system the the characteristic length L is typically very small, and the operating fluid flow is in the Stokes flow regime. To give an example, a micro channel with a cross section 100 μm x 100 μm, containing fluid flowing at 100 μmL/h, will result in $Re \sim 1/3$. For this system the cross sectional length 100 μm is chosen as the characteristic length. For Stokes flow, viscous forces dominate over inertial forces, and mixing only occurs due to diffusion when no other external forces act on the system, and Equation (2.1) can be simplified to:

$$\frac{d\hat{\mathbf{U}}}{d\hat{t}} = -\hat{\nabla}\hat{p}$$
(2.3)

Hence, only a change in pressure will change the velocity of the fluid in a typical microfluidic channel.

Because of the laminar nature of microfluidic systems particles suspended in a fluid medium tend to follow the fluid streamlines unless a laateral force acts on them, moving the particles from their original path.

3 | Surface Acoustic Waves

Surface acoustic waves (SAWs), also known as Rayleigh Waves, were first described by Lord Rayleigh in 1885 [34]. Surface acoustic waves propagate on the unbound surface of an elastic solid. For a surface spanning in the xy-plane, a surface acoustic wave will cause a longitudinal motion in the z-direction and transverse motion in the x-direction (Figure 3.1 **A** and **B**). For a material with isotropic properties, the longitudinal and transverse amplitudes will decay exponentially in the negative z-direction (vertically into the surface), and there will be almost no movement of the particle lattice in the xz-plane at a depth equal to the wavelength of the SAW (Figure 3.1 **C**). To show an example, Ristic calculates the vertical displacement of a SAW wave in his book *Principle of Acoustic Devices*: A SAW, generated into a 1 cm wide beam by a 10 mW power device at 100 MHz, will create a surface wave with a 30 μm wavelength, propagating though the beam. With a phase velocity in the material $s = 3 \cdot 10^3$ m/s, the peak vertical displacement will be 10^{-10} m [35, p. 91–98]. Hence SAWs' propagating nature gives it a two dimensional spread over the surface. Because of its low energy loss to vertical displacement, the waves amplitude decays more slowly in the surface plane compared to other type of elastic waves [36].

The SAW frequency, also referred to as the center frequency, is given as:

$$f_0 = \frac{v}{\lambda}.$$ (3.1)

v is the phase velocity of the SAW, which depends on the propagating medium, and λ is the wavelength.

3.1 Generating Surface Acoustic Waves

Surface acoustic waves can be generated on the surface of a piezoelectric crystal by applying a electric potential to an interdigital transducer (IDT), installed on top of
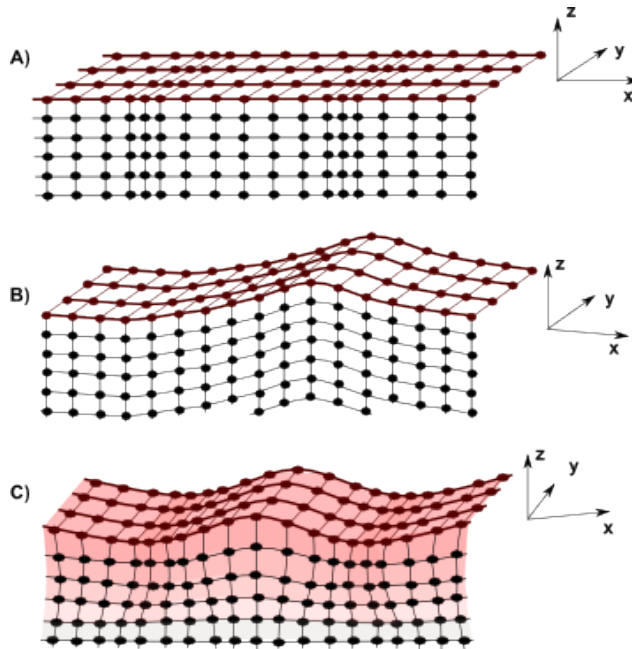
Figure 3.1: **Wave Propagation in Solid**
A) Displacement of lattice elements in an isotropic solid crystal due to longitudinal waves. The red elements symbolize a free surface, i.e. the surface layer. **B)** Displacement of lattice elements in a isotropic solid crystal due to transversal waves. **C)** Displacement lattice elements in a isotropic solid crystal due to a surface acoustic wave. The movement consist of both longitudinal and transverse/shear motion, which are coupled by the boundary surface. The wave amplitude in the negative z-direction decays rapidly, hence there is little or almost no displacement at roughly a wavelengths distance into the solid.
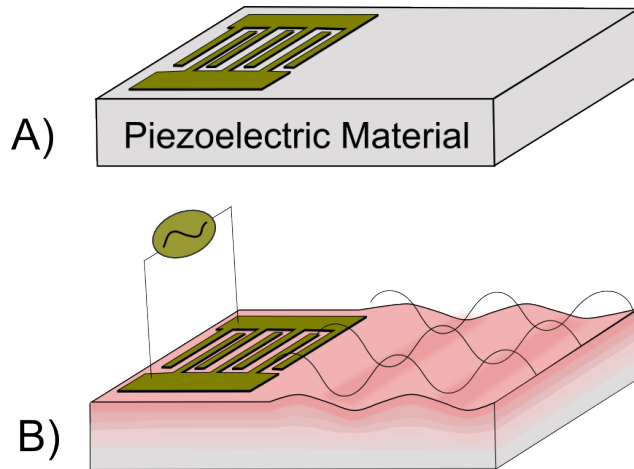
Figure 3.2: **Illustration of IDT Generated SAW**
A) An IDT deposited on top of a piezoelectric crystal, using thin-film deposition.
B) When a sinusoidal voltage signal is applied to the IDT, SAWs are generated on
the surface of the piezoelectric crystal. The wave is propagating in a direction per-
pendicular to the electrode-fingers in the IDT. The wave exponentially decays with
depth into the surface, with a penetration depth usually shorter than the wave-
length of the SAW. The beam width of the wave is equal to the length of the over-
lapping region of electrode fingers on the IDT.

the piezoelectric substrate (Figure 3.2). The IDT can be deposited onto the piezo-
electric crystal by thin-film deposition (described further in Chapter 4), and con-
sists of two sets of overlapping and opposite facing, spatially periodic electrodes
which consists of several electrode fingers in parallel to each other (Figure 3.3).
This way, two neighboring electrode fingers will have opposite polarity in their
electric field when a voltage signal is applied to the electrodes. Because of the
piezoelectric effect, alternative regions of tensile and compression strain between
the electrode fingers, on top of the piezoelectric substrate, will be created when
an alternating current is applied. As a result, a mechanical wave is produced on
the surface of the substrate, generating a surface acoustic wave. Uniform IDTs will
generate a single-phased wave because of the interdigital array with spatially pe-
riodic electrodes. Due to the symmetric structure of the IDT, the generated wave
will propagate in two opposite directions on both sides of the IDT, perpendicular
to the electrode fingers.

The specific properties of the generated SAW will depend on the spatial ge-
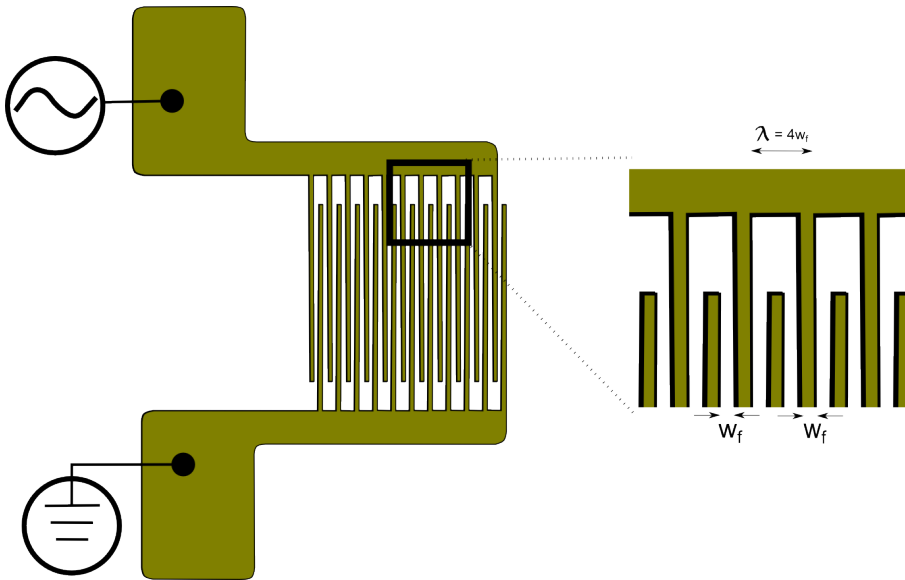
Figure 3.3: **Illustration of a Uniform IDT**
When the width of the electrode spacing and the electrode fingers are equal w_f, the generated SAW will have a wavelength λ equal to $4w_f$. Alternating current is applied to the conductive signal pads.

ometry of the IDT and the applied electrical signal. If the spacing between the electrode fingers are equal to the width of the electrode fingers w_f, the IDTs are uniform, and the elastic strain generated will produce a SAW with a wavelength λ equal to $4w_f$ (Figure 3.3). Hence we can decide the wavelength λ of the generated wave by choosing certain geometrical properties of the IDT. For example: With an electrode finger spacing and width of 25 μm the generated SAW will have a wavelength of 100 μm. For exploratory reasons, if we define the IDT pitch as the width of two electrodes and two spacing, i.e. the length corresponding to the wavelength of the generated SAW. The transducer operates with the highest efficiency when the center frequency, correlated to the pitch and the phase velocity of the medium (see Equation 3.1), is equal to the frequency of the applied alternating voltage signal [37, 36]. Hence, for an optimal device the frequency of the applied signal frequency f_0 should be equal to the frequency of the generated SAW. This frequency is what we will refer to as the resonance frequency of the IDTs.

AS mentioned above, the value of the resonance frequency, resulting in the lowest possible insertion-loss, is correlated to the IDT geometry and the SAW propagating material. For a surface acoustic wave propagating on a typical piezoelectric

material, the phase velocity is 10^3-10^4 m/s [35, 38]. However, this value will vary according to the angle between the direction of the propagating wave and the crystal orientation of the material [39].

3.1.1 Reducing Insertion-Loss

SAW Reflector

As described above, a uniform IDT will create two SAWs propagating in opposite direction. To reduce the insertion loss of the IDT, a SAW reflector can be used to reflect one of these waves in the opposite direction. A SAW reflector, also called reflection gratings, are composed of periodically spaced discontinuities on the piezo-electric SAW propagating surface. To construct these reflection gratings, short-circuited electrode fingers, identical to the ones of the SAW generating IDT, are deposited on the piezoelectric surface. These electrodes are not connected to an electrical potential, nor ground. When a series of reflector electrodes are located at a distance $\lambda/4$ from the closest electrode finger on the IDT, the reflected SAW will have an additive effect to the SAW propagating in the direction away from the reflectors [40].

SPUDTs

Single-Phase Unidirectional Transducers (SPUDTs) can be used to construct low-loss unidirectional SAW transducers [39, 41, 42]. Focusing IDTs (FIDTs), described later on in Chapter 5, have curved electrodes. Instead of adding SAW reflectors to the design, wider reflective electrode fingers are added in between the electrode fingers for reflectance. To propagate the maximum acoustic energy in the forward direction, the geometry of the electrodes and the additional reflectance electrodes have to be carefully adjusted.

3.1.2 Frequency Response

To find the resonance frequency of the IDTs one can investigate the frequency response when a voltage signal of a varying frequency is applied to the electrodes. For a signal with a specific frequency the IDT will create a SAW with a corresponding amplitude, depending on the geometry of the IDT. When two IDTs are facing each other the SAW generated from one (active) IDT will travel to the opposite (passive) IDT. The vibration caused in the piezoelectric surface by the generated SAW will create an electric signal in the passive IDT. This response can be

measured for the specific frequency applied to the active IDT, and a response for a range of frequencies can be mapped. This way one can investigate which frequency causes a SAW with the highest amplitude. Frequency response measurements are usually achieved by using a network analyzer, sweeping over a range of frequencies and recording the measured amplitude at the passive IDT.

3.1.3 Lithium Niobate

Lithium Niobate (LiNbO$_3$) is an anisotropic crystal that possess piezoelectric properties. For a Y-cut 128° oriented LiNbO$_3$ wafer an acoustic wave will have an optimal surface wave velocity and electromechanical coupling coefficient in the X-direction of the saggital XZ–plane. At this orientation, the phase velocity of a SAW wave traveling on a free LiNbO$_3$ surface is v = 3979 m/s [43].

3.2 Leaky SAW

When a SAW carrying surface is bounded to a fluid or a solid there will be a energy transfer between the interfaces, causing an attenuation to the propagating wave [38, 36]. This phenomenon, where a SAW looses energy due to radiation, causes the amplitude of the SAW to decay and results in a leaky SAW. For a solid-fluid interface the SAW will radiate energy into the fluid at an angle, defined as the Rayleigh angle θ_R, which can be described by Snell's law[36, 44]:

$$sin(\theta_R) = \frac{v_f}{v}. \tag{3.2}$$

Here, v_f and v are the phase velocities for the fluid and the SAW propagating surface, respectively. The energy loss for a leaky SAW over a distance x goes as e$^{-\alpha x}$, where α is defined as the attenuation coefficient, given as [36]:

$$\alpha = \left(\frac{\rho_f}{\rho_s}\right)\left(\frac{v_f}{v\lambda}\right)m^{-1} = f\left(\frac{\rho_f}{\rho_s}\right)\left(\frac{v_f}{v^2}\right)m^{-1}, \tag{3.3}$$

where ρ_f and ρ_S are respectively the densities of the fluid and the solid. The radiation energy from the surface acoustic wave is transfered through the surface-fluid interface, causes a longitudinal compression wave in the fluid (Figure 3.4). For anisotropic mediums the attenuation coefficient is proportional to the signal frequency.

The attenuation of the wave is greatly determined by the specific interfacing materials, as we can see from Equation (3.3). For atmospheric air the attenuation
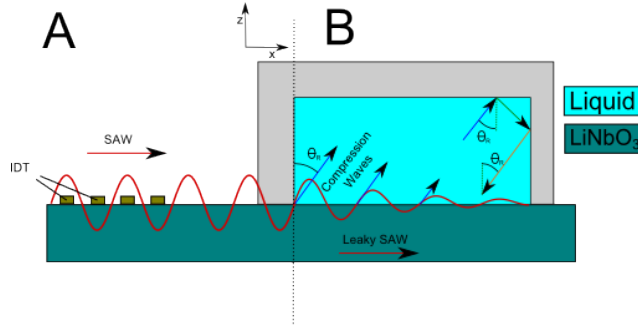
Figure 3.4: **Leaky SAW**
A: A SAW is generated from IDTs and moves across a $LiNbO_3$-Air interface with a very low energy loss. **B:** Due to the high attenuation coefficient for water a leaky SAW occurs at the $LiNbO_3$-Water interface. The radiation energy from the leaky surface acoustic wave causes a longitudinal compression wave in the fluid, at an angle θ_R, described by Snell's law. The compression waves will reflect of the walls of the PDMS chamber, creating a pressure field inside the liquid chamber.

Table 3.1: Values of attenuation coefficient from radiation, α, for $LiNbO_3$-water and $LiNbO_3$-air interfaces are listed. The coefficients for water and air specific frequencies are found in studies from Gedge et. al. [36].The values for 39.8 MHz and 79.6 MHz are calculated from the values of these studies, since the attenuation coefficients are linearly proportional to the frequency (Equation 3.3).

Constant	Medium	Attenuation Coefficient [m^{-1}]	
		39.8 MHz	79.6 MHz
α	Atmospheric Air	0.29	0.59
α	Water	1035	2070

coefficient is small enough to be ignored, while for water it is not (see Table 3.1). This is why SAWs propagating on a surface in atmospheric air will have a low loss of energy. Friction losses from the transverse motion of the fluid will also cause attenuation, however for a $LiNbO_3$-Water interface the leaky effect caused by friction losses is much less than the one caused by radiation [36].

3.3 Standing Surface Acoustic Waves

When two opposite propagating SAWs meet, the constructive interference of two facing waves result in the formation of a standing surface acoustic wave (SSAW).
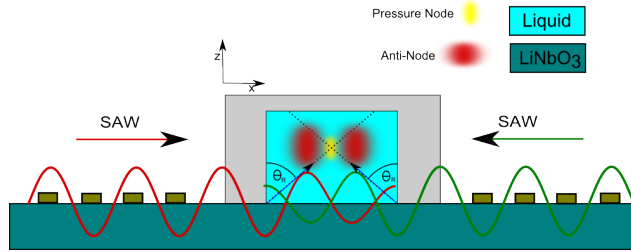
Figure 3.5: **SSAW Generating Pressure Field in Liquid**
Two opposite propagating waves crates a leaky SSAW at the LiNbO$_3$-Liquid inter-
face. The compression waves which are generated inside the liquid will interfere,
generating i pressure field. Pressure nodes and anti-nodes will appear in the same
horizontal location (on the x-axis) as the SSAW anti-node and pressure node, re-
spectively.

For a chamber of liquid located on top of the SAW propagating surface, leaky SSAW
will generate compression waves inside the liquid. For a constrained chamber
geometry these compression waves, generated by the leaky SSAW, will result in a
pressure field inside the chamber. The interference of compression waves creates a
periodic distribution of pressure nodes (zero pressure) and anti-nodes (maximum
absolute pressure amplitude) inside the liquid chamber. The interferance of the
compression wave, and their reflection at the chamber walls, decides the geome-
try of the pressure field, resulting in the nodes and anti-nodes. As demonstrated in
Figure 3.5 the lateral (x-axis in figure) location of the nodes and anti-nodes, gen-
erated by the SSAW inside the fluid chamber, are decided by the Rayleigh angle.
Several studies have been made to simulate the pressure field generated in mi-
crofluidic channels [44, 45, 46]. For a horizontal symmetrical chamber (or channel)
the pressure nodes and anti-nodes in the liquid will appear in the same horizontal
location as the SSAW anti-nodes and nodes, respectively.

3.4   Acoustophoresis

Acoustophoresis is referred to as a method for manipulating matter in a medium
using acoustic waves. When intense sound waves are sent into a medium, an
acoustic radiation pressure field will be created, creating a radiation force that acts
on the matter. In this section we will look into acoustophoresis created inside a
liquid medium due to leaky SSAWs.

3.4.1 Particle manipulation

The pressure fluctuation inside a liquid channel, generated by the SSAW, results in acoustic radiation forces acting laterally on particles obtained in the fluid [47]. A particle moving inside a liquid channel will experience three types of forces in addition to the lateral acoustic radiation force: The viscous force, acting in the opposite direction of the particles velocity relative to the flow stream; gravity, acting downward towards the bottom of the channel; and buoyant forces, acting upwards in opposite direction of the gravity force. In the vertical direction of the channel, gravity and the buoyant forces are similar in magnitude but opposite in direction, hence balancing each other out. The acoustic radiation and viscous force, respectively F_a and F_v, can be expressed as [31, 47]:

$$F_a = -\left(\frac{\pi p_0 V_p \beta_m}{2\lambda}\right)\phi(\beta,\rho)sin(2kx), \tag{3.4}$$

$$\phi(\beta,\rho) = \frac{5\rho_p - 2\rho_m}{2\rho_p + \rho_m} - \frac{\beta_p}{\beta_m}, \tag{3.5}$$

$$F_v = -6\pi\mu r v. \tag{3.6}$$

p_0, V_p, λ, k, x correspond to the pressure field amplitude, particle volume, SAW wavelength, wave vector and distance from a pressure node. While μ, r and v correspond to the medium viscosity, particle radius, and velocity of the particles relative to the fluid. ϕ is the acoustic contrast factor, and depends on the density and compressibility of the medium and the particles, ρ_m, β_m, ρ_p and β_p, respectively. Particles in a liquid will aggregate at pressure nodal lines when ϕ is positive and at pressure anti-nodal lines when ϕ is negative, due to the acoustic radiation force. Both the particles vertical and horizontal position in the channel is affected by the acoustic radiation forces, and the particles positions will not only be manipulated laterally by the nodal points, but also be focused in the vertical plane [44]. However, the acoustic radial force is weaker than the radial radiation force given in Equation (3.4) [48]. Since the acoustic radiation force is proportional to r^3, while the viscous force is proportional r, larger particles experience much larger net force than smaller ones. Hence, larger particles will be acted upon by a bigger force than smaller particles. For particles moving in a laminar flow, an introduced radiation force will act on the particles as an additional force, moving them laterally into different streamlines. This lays a foundation for the principal of acoustophoretic size dependent filtration in microfluidics.

4 | Microfabrication

4.1 Photolithography

Photolithography is a fabrication technique where light is used to pattern structures from a photomask onto a photoresist-coated substrate. The process is illustrated in Figure 4.1, with a silicon wafer as substrate and SU-8 as photoresist. Starting with a substrate, a layer of photoresist is spincoated to a certain thickness on top of the substrate. Light with a specific wavelength and intensity is exposed to the photoresist through a photomask for a period of time. The photomask contains transparent regions where light can go though and non-transparent regions where light is blocked. A photomask has a positive polarity when the pattern is made out of transparent regions while the background is opaque, and vice-versa for a negative photomask. These masks can be designed using the commercial software application AutoCAD. For a positive photomask the light is exposed though the pattern in the mask onto the photoresist. The photons will generate a photochemical reaction in the photoresist, modifying its material properties. A negative photoresist will have its unexposed areas soluble to photoresist developers, while the exposed area will be soluble to the developer for a positive photoresist. Hence, the pattern is either left or removed in the photoresist when the substrate is treated with developer, depending on the specific type of photoresist. Figure 4.1 illustrates photolithography using a negative photoresist.

4.1.1 SU-8 Photoresist

SU-8 is a series of epoxy-based negative photoresists, originally developed for the microelectronics industry by IBM [49]. A SU-8 molecule consists of 8 epoxy resin groups (Figure 4.1 **B**), containing the photo acid generator triarylsulfonium salt. When SU-8 is exposed to light a photochemical reaction occurs when photons
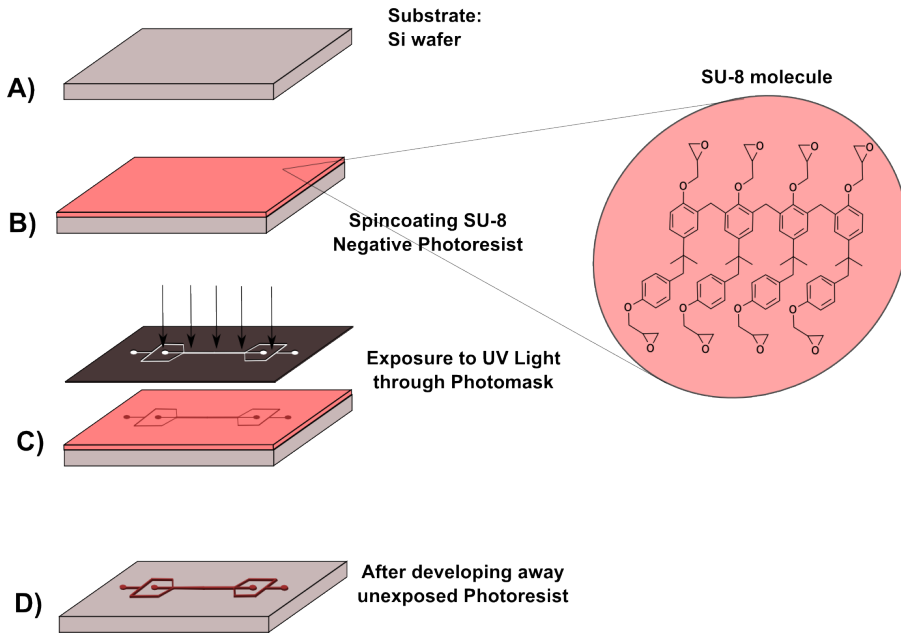
Figure 4.1: **Photolithography Process, Si-wafer and SU-8 Photoresist**
A) A silicon (Si) wafer is treated with oxygen plasma and heated by a dehydration-bake process to remove any contamination and promote dehydration of the wafer. **B)** SU-8 photoresist is spincoated onto the Si wafer to create a uniformly thick layer, and excess solution is evaporated though a soft-bake procedure. **C)** The photomask is brought in contact with the photoresist-coated wafer, and the resist is exposed to UV light though the transparent pattern on the mask. The Si wafer is thermally heated during a post-bake process which causes the exposed SU-8 molecules to cross-link. **D)** A specific photoresist developer for SU-8 removes all the molecules that were not exposed to the UV light, revealing the remaining pattern caused by the cross-linked polymers. An optional hard-bake procedure can be added to improve the stability of the resist.

are absorbed by the salt, creating exafluoroantimonic acid. The acid protonates the epoxide groups in the resin monomer, and will cross-link when treated with heat. The molecules that were not exposed to photons will be developed away by a photoresist developer. Hence, only the cross-linked structures will remain on the substrate. A single photon can start multiple polymerizations in SU-8, making it a chemically amplified resist which require less light intensity. SU-8 has a maximum absorption of light at 365 nm, characterized with the I-line of a mercury (Hg) lamp. Its transparent properties, high chemical and thermal resistance and large aspect ratio of 1:20 makes SU-8 a suitable choice of material for micro fabrication [50, 51, 52] .

4.1.2 Resolution

The minimum feature size of the pattern exposing the photoresist to light is mainly limited by optical diffraction according to the Rayleigh equation [53]:

$$R = k_1 \frac{\lambda}{NA},\tag{4.1}$$

where λ is the wavelength of the illuminating light, NA is the numerical aperture, and k_1 is a constant that depends on the photoresist. A submicron minimum feature size can be achieved when using 360 nm UV light [53].

The quality and resolution of the photomask will also improve the resolution and quality of the structure. Photomasks made out of chrome can contain a finer structure and will be less prone to defects in the mask and its pattern, compared to masks made out of plastic.

The spacing between the photomask and the photoresist-coated substrate also has an effect on the resolution. Proximity lithography occurs when this gap is present, while contact lithography is when the photomask and photoresist is in direct contact. For both methods the mask covers the entire wafer and requires the same light intensity, however the resolution in proximity printing is the square root of the product of wavelength and the gap distance. Hence, contact printing offers the best resolution since the gap distance is approximately zero.

4.2 Thin-Film deposition

Thin-film deposition is the technology of applying a very thin film of material onto a substrate surface. The thickness of the film can be as thin as a few nanometers – the thickness of a few atoms. There are several different techniques of thin film

deposition, usually divided into chemical deposition and physical deposition.

4.2.1 E-beam Evaporation

E-beam evaporation is a Physical Vapor Deposition (PVD) technique, using thermal evaporation. The substrate is loaded into a vacuum chamber with low pressure conditions. Inside the chamber an electron beam is generated from a filament using a high voltage. The beam is aimed at the source material, that is to be deposited onto the substrate, by an electric and magnetic field. The surface atomic layer of the source material will then have sufficient energy to leave the surface (i.e. vaporize) inside the vacuumed chamber. A shutter protects the substrate from the vapor, and is removed when a quart crystal monitor sensor inside the chamber measures the wanted rate of evaporation. When the targeted thickness of the film is achieved the shutter will cover the substrate, once again protecting it from the vapor. The high voltage is turned off, and after the source material has cooled down, the substrate can be unloaded from the chamber or a new deposited can be made to the thin film-covered substrate.

The mean free distance is the average distance an atom or molecule can travel in a vacuum chamber before it collides with another particle thereby disturbing its direction to some degree. The vacuum in the chamber has to be low enough to create a mean free path longer than the distance between the substrate and the source material, which is typically around $1 \cdot 10^{-4}$Torr [54]. Hence, a uniform layer of vaporized particles can be deposited on the substrate at pressure below this threshold.

4.3 Lift-off

Lift-off is a microfabrication method to pattern structures of the nanometer scale on a substrate using a sacrificial material. A lift-off procedure is illustrated in Figure 4.2, using an image reversal photoresist and thin-film evaporation to create a two layer electrode on a LinbO$_3$ substrate. The sacrificial material, such as photoresist, is first deposited and patterned on the substrate, using micro-patterning methods like standard photolithography or etching. The material of interest is then deposited on top of the sacrificial layer, using deposition methods like thin-film E-beam evaporation. When the sacrificial material is removed, only the material deposited directly on the substrate will remain, while the rest will be removed together with the sacrificial material. The method of removal depends on the sacrificial material that is being used.
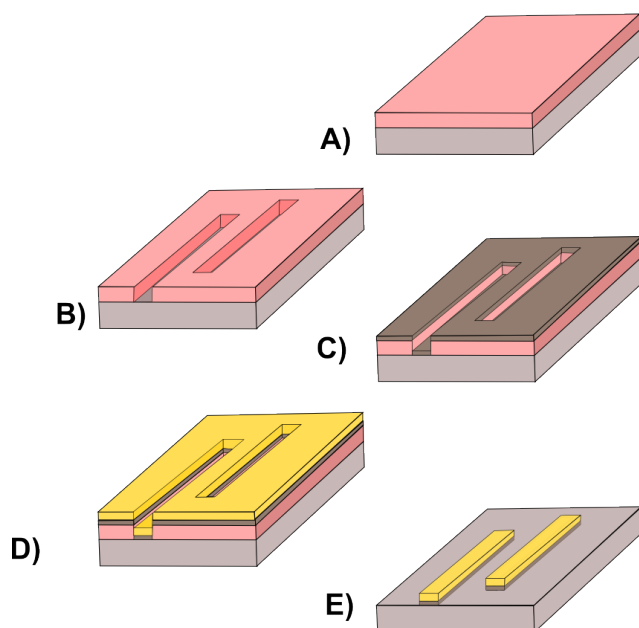
Figure 4.2: **Lift-Off Process**
A) Image reversal photoresist is used as a sacrificial layer, spin-coated on a LiNbO$_3$ wafer. **B)** Photolithography is used to create an invert pattern of choice in the photoresist. **C)** A thin film of metal is deposited uniformly on the photoresist and the uncovered wafer, using E-beam evaporation. **D)** A second thin film of a different metal is deposited uniformly on the first layer of metal, using E-beam evaporation. **E)** The sacrificial layer and its mounted layers of metal is removed by using isopropanol and acetone. The solvents attacks the photoresist that is exposed, dissolving it. The lift-off process is complete when the only structures remaining are the layers of metal that were deposited directly onto the wafer.

The minimum feature size depends on the specific patterning and deposition methods. Our main approach will be on using image reversal photoresist and photolithography as the patterning method, and E-beam evaporation as the thin-film deposition method.

4.3.1 Image Reversal Photoresist

Image reversal photoresist has advantages in lift-off, due to its specific properties. After spincoated to a certain thickness onto a substrate, the resist is exposed though a photomask. The resists behave as an exposed positive resist, and a reversal baking step cross-links the exposed area. The unexposed area remains pho-

toactive. When all of the photoresist is exposed a second time, this time without the photomask (flood exposure), the areas that were not exposed in the first step becomes soluble. After development, the only photoresist remaining will be the areas that were exposed in the first step. These steps are shown in Figure 4.3. The advantage of image reversal photoresist is the undercut feature which is created in the reversal process. The undercut is an advantage since the solvent will have easier access to the resist when covered with additional metal layers. Especially when the thickness of evaporated film is close to or exceeds the thickness of the resist, as shown in Figure 4.3 **E**.Exposure time, reversal baking time, reversal bake temperature and development time are all parameters that will have an effect on the undercut features. There are several recommended protocols that explains the parameters and processes that causes undercuts [55], and hence will not be discussed further in this work.

4.4 Soft lithography

Soft lithography was first introduced in the 1990's to tackle the problem of the then current advanced and expensive microfabrication techniques for the semiconductor industry. The techniques were at that point not suitable for research or use in other disciplines outside of microelectronics. It is a "rapid prototyping" technique where an elastomeric material is used to generate micropatterns, using techniques like replica molding, contact printing or imprinting. A brief description of other soft lithography techniques can be found in the paper of Xia and Whitesides on soft lithography from 1998 [53].

4.4.1 Polydimethylsiloxane

Polydimethylsiloxane (PDMS) is the most common elastomer used in soft lithography. It consists of repeated monomers of organic methyl groups attached to the silicon atoms in the inorganic siloxane group. The polymer has the chemical formula $[SiO(CH_3)_2]_n$, and the repeating siloxane group forms a backbone thoughout the polymer in which the methyl groups are attached to (Figure 4.5 **A**). Depending on the degree of polymerization in the PDMS base, the polymer may be semi-solid (high n) or almost liquid (low n). When mixed with crosslinker agents the PDMS will cure and harden, a process that is catalyzed when thermally treated. Both liquid and hardened PDMS is optically transparent down to about 300 nm, homogeneous and chemically inert. Hence it is a well suitable polymer in soft lithography as the cast for the master mold, especially due to its ability to replicate microscale,
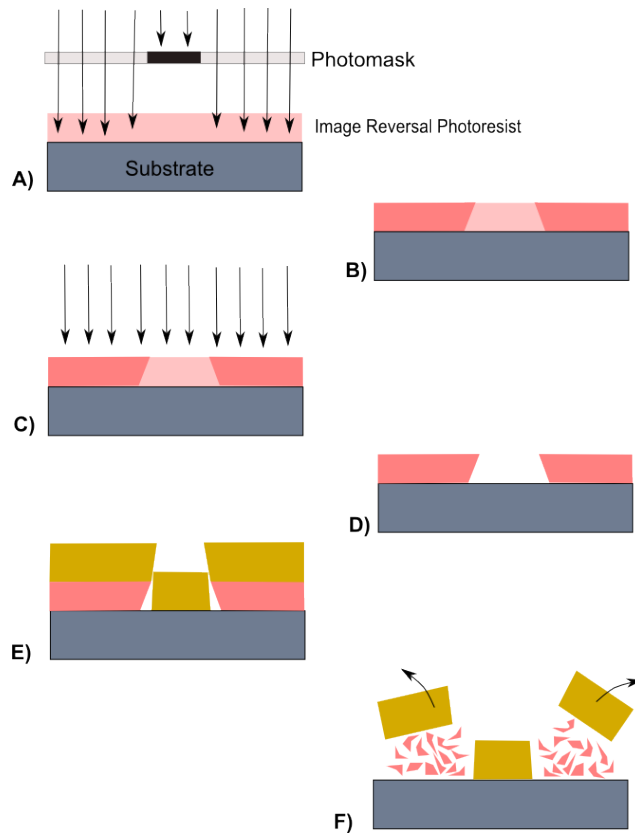
Figure 4.3: **Image Reversal Photoresist**
A) Image reversal resist is spincoated on to a cleaned substrate and exposed to UV light though a photomask, making the exposed area soluble. **B)** The exposed sample is then treated through a reversal bake, which cross-links the polymers in the exposed resist. **C)** The whole sample is then exposed to UV light without using a photomask (flood exposure). The area that were not exposed during the first exposure now becomes soluble. **D)** The now soluble areas are removed using a developer, and an undercut feature is created though the process. **E)** The undercut is important in the lift-off process, since it will expose the photoresist to solvents even after the sample is treated with thin-film evaporation. **F)** Therefore, the film mounted on top of the resist can be removed by exposing the resist to solvents which will remove both the resist and hence its mounted metal layer.

non-planar structures [53]. Another noted property of PDMS is its low change in spacial dimensions during its curing process, with a shrinking ratio of 1.06% when cured at 65 °C for four hours [56].

4.4.2 Replica Molding

Replica molding is a soft lithography method where a self-assembled elastomeric material is used to generate a negative cast of the pattern on a mold with micropatterns. The minimum structure size resolution of replica molding is limited to the size of the self-assembling layer of elastomers and their interactions to the substrates of the master mold, but should allow accurate replications of structures with a resolution down to 100 nm [53]. Therefore, the resolution limiting factor of replica molding is usually the structure size of the master mold. A schematics of the soft lithography replica molding procedure is shown in Figure 4.4, where PDMS is used as the elastomer and the mold is made of SU-8 structures on a Si substrate using photolithography (see Section 4.1). The master mold is silanized to prevent the elastomer polymers sticking to the structures on the mold, and to increase its life-time. The mold is put inside a desiccator together with a small amount of silane. The silane will start to vaporize when the pressure inside the desiccator is reduced. Covalent Si-O-Si bonds will start to form when the vaporized silane reacts with the hydroxyl groups on the surface layer of the substrate. The liquid PDMS and curing agents are poured onto the mold before it is thermally treated in an oven to catalyze the hardening process. When the PDMS is fully hardened it is pealed of the mold. The mold can be reused several times if handled with care. Hence, replica molding is a "rapid prototyping" process where only one master mold is required to fabricate several inexpensive PDMS microfluidics devices.

4.5 Oxygen Plasma Treatment

Oxygen plasma can be achieved in a low pressure chamber by exciting oxygen gas though a supply of energy. A radio frequency (RF) generator applies a high voltage electrical signal to an electrode inside the chamber. The electrons dissociates the oxygen gas molecules, creating high energy oxygen ions. The high energy plasma will bombard any exposed surface inside the chamber. In this section we will look at some of the effects that occur from treating a material surface with RF oxygen plasma, and how they can be used for our purposes.
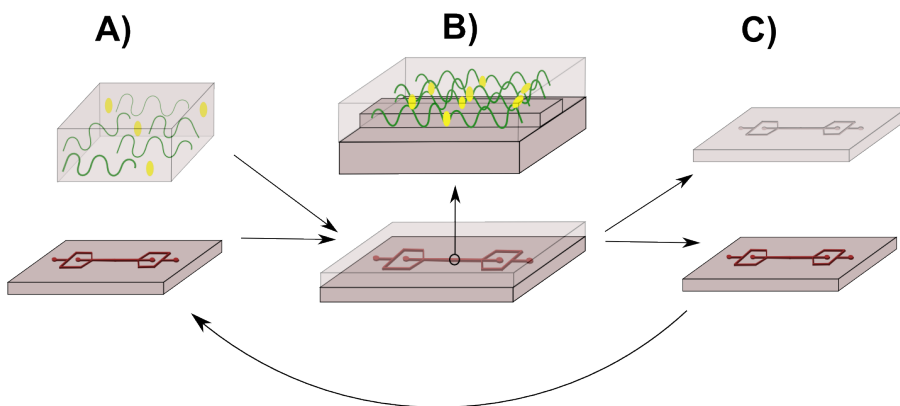
Figure 4.4: **Soft Lithography Replica Molding using PDMS**
A) Top: Liquid silicon elastomer base (PDMS) is mixed with curing agents. Bottom: A SU-8 structure on a Si substrate is used as a master mold, created using standard photolithography. **B)** Top: The liquid PDMS is poured onto the master mold, where it self-assembles on top of the microstructure. The mold is treated prior to this step by silanization to prevent the elastomer from sticking to its surface. Bottom: The liquid PDMS cross-link over time due to the presence of curing agents, creating a solid block with negative microstructures relative to the master mold. **C)** Top: The solid PDMS with the negative structures is pealed of the mold and can be used for further purposes. Bottom: The master mold can be reused, making soft lithography a "rapid prototyping" technique.

4.5.1 Plasma Ashing

Oxygen plasma at low pressure can be used to remove organic material from surfaces. When treated with oxygen plasma a surface will be bombarded with oxygen ions. These ions will fully oxidize organic residues, creating volatile molecules such as CO_2, CO and H_2O [57]. The volatile molecules are removed from the plasma chamber using ventilation systems.

4.5.2 Plasma Bonding

When PDMS is treated with oxygen plasma the most exposed methyl groups at the surface layer, attached to the siloxane backbone, will be oxidized by the oxygen ions. As a result, silanol groups develops at the expense of methyl groups (see Figure 4.5 **B** and **C**), lowering the surface energy of the polymers exposed surface [58].

The oxidation reaction also occurs on the surface of a range of different materials during oxygen plasma treatment, including silicon oxide and lithium niobate [58, 59]. When plasma treated PDMS is brought into contact with one of these plasma treated materials, a tight irreversible seal is created through a condensation reaction [60]. This seal is due to Si-O-R covalent bonds, forming between the two surfaces with the additional release of a water molecule (see Figure 4.5 **D**).The R represents the functional group that is attached to the hydroxyl group located at the surface of the material that is bonding to PDMS.

The total exposure time, the RF power and the pressure inside the chamber during the plasma treatment are important parameters for the bonding to success. If the RF power and the exposure time is too low, or the chamber pressure is too high, the effect on the treated surface may be too low for the bonding to be successful. On the other hand, if the RF power or the exposure time is increased too much the bonding will not be successful either [60]. Hence, its important to find a correct set of parameters to achieve successful plasma bonding.

The additional effect of removing organic molecules from the surface during the plasma treatment (see Section 4.5.1) will bring the surfaces into closer contact, increasing the success of bonding between two plasma treated materials.

Ethanol can be introduced to the treated surfaces as lubricants when aligning the two surfaces. Ethanol will not effect the bonding reaction, only delay it until the liquid is evaporated [44].
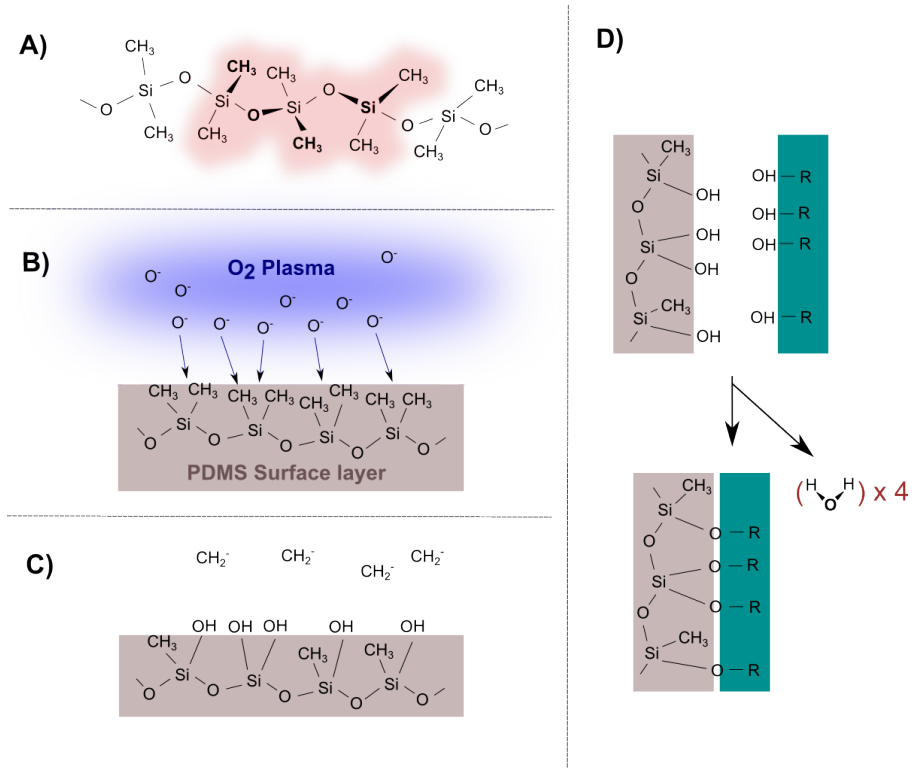
Figure 4.5: **Plasmatreatment of Polydimethylsiloxane (PDMS)**
A) Chemical structure of PDMS, where the repeating monomer unit $SiO(CH_3)$ is marked in pink. The polymer consist of methylgroups attached to a siloxane backbone. **B)** When exposed to oxygen plasma the ionized oxygen will oxidize the methylgroups at the PDMS surface layer. **C)** Methyl ions are released into the air, substituted by hydroxyl groups, and the methyl ions are vented away from the system. **D)** Plasma treated PDMS can form irreversible bonds to other plasma treated surfaces, due to the hydroxyl groups on the surfaces. The surfaces are simple brought into contact immediately after the plasma treatment, creating covalent bonds in a condensation reaction.

4.5.3 Hydrophilic Surfaces

PDMS is natively hydrophobic, hence sealed microfluidic channels are difficult to fill with liquid without applying pressure. When treated with oxygen plasma the PDMS surface will oxidize, creating a high surface energy. Due to this, the surface layer in the microchannels and at the surface of the PDMS, becomes hydrophilic and is hence easier to wet by polar liquids [58]. The surface's hydrophilic abilities will increase with increasing generated RF power and treatment time. A qualitative measurement of the surface's hydrophilic abilities after plasma treatment can be achieved by placing a small drop of water on the surface and measuring its contact angle to the treated surface; A hydrophobic surface will have a large contact angle, while a hydrophilic surface will have a contact angle close to zero. The treated surface can stay hydrophilic for hours when exposed to air, before returning to its native hydrophobic state [61].

5 | Acoustophoretic Device

From the principles of SSAW generated acoustophoresis in microfluidic systems, one can create a device that separates particles according to their size. An illustration of the principle of separation by SSAW is shown in Figure 5.1.

A PDMS channel is aligned on top of a LiNbO$_3$ with a deposited pair of facing IDTs. The channel is aligned so that the center of the channel is located directly in between the two IDTs. When fluid is present in the channel, leaky waves from the SSAW field will generate pressure nodes in the channel.

Particles in water are presented to the channel though inlets in the PDMS. The fluid is driven by a continuous flow, and the particles move in a laminar flow regime, due to the nature of the channel size and flow regime. Because of this the particles stay in a specific flow stream unless acted upon by an external force.

When passing through the SSAW field the particles are acted upon by the acoustic radiation force, introduced by the pressure anti-nodes; depending on size, density and compressibility the particles are moved horizontally in the channel, between the channels side walls, into different streamlines. After passing the SSAW field, the channel guides the particles out though different outlets, depending on the particles new lateral location.

For our purposes, the device will be used for separating polystyrene particles of different size. The specific types and sizes of polystyrene beads are represented in Chapter 6. The density of polystyrene particles are 1050kg/m^3, and the compressibility is 249 TPa^{-1}. The density of water is 997 kg/m^3, and the compressibility is 448 TPa^{-1} [29]. This results in a positive acoustic contrast factor ϕ (Equation 3.5), which means that water dispersed polystyrene particles will move towards the pressure nodes created by the SSAW field.

In this chapter the design of the components for the final device will be described. The separation device consists of two components: The IDTs, fabricated on a LiNbO$_3$ wafer, and a PDMS microchannel. The two components are irre-
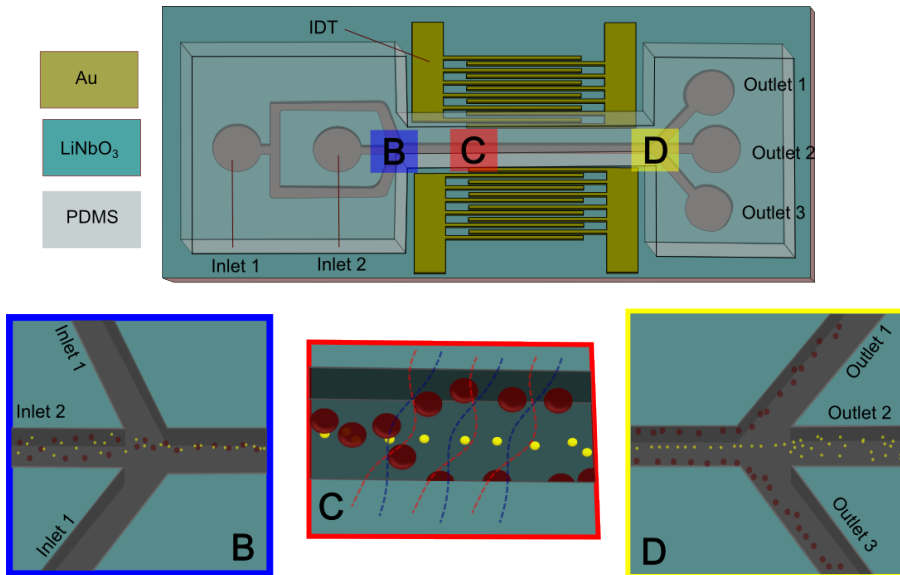
Figure 5.1: **Illustration of Separation Device**
A: The micro channel is fabricated in PDMS, using photolithography and soft lithography. Two gold IDTs are facing each other, fabricated on top of a LiNbO$_3$ surface using photoliography, thin film deposition and lift-off. The two components are irreversible bonded using plasma bonding. **B:** Particles of different size are injected though inlet 2. Water is injected though inlet 1 as sheath flow, focusing the particles in the center of the channel. **C:** The pressure nodes in the channel, created by the SSAW, forces the particles away from the center. The force acting on the particle is proportional to the size of the particles, moving bigger particles faster out from the center than smaller particles. **D:** The smaller particles, which are centered in the middle of the channel, will exit the device through outlet 2. The bigger particles, which are driven out from the center to a different flow stream, are exiting through outlet 1 and outlet 3.
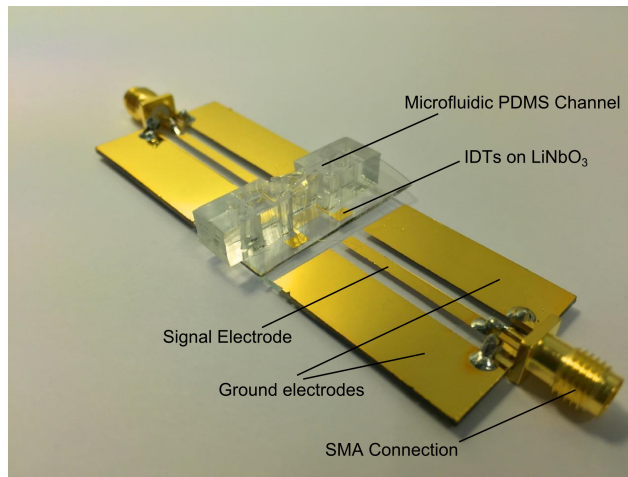
Figure 5.2: **Final Device With IDT$_A$ Design**
The final separation device, consisting of SAW generating IDTs on a LiNbO$_3$ substrate with a PDMS microchannel bonded to it. The separation device is mounted on top of a glasslide covered with gold electrodes, two for ground and one for signal. The SAW generating signal is applied though SMA connections which are soldered onto the gold electrodes. The IDTs are connected to the gold electrodes by wire bonding (not shown in this image).

versible bonded together using plasma bonding, and mounted on top of a glass slide coated with golden electrodes and SMA connectors. The electrodes on the slide is connected to the IDTs by wirebonding.

5.1 Interdigitial Transducers

All the IDT mask designs are constructed in AutoCAD by Jonas M. Ribe. The characteristics of all the different IDT designs are listed in Table 5.1. The spacing between the IDT pair correspond to a defined number of SAW wavelengths to achieve the specific SSAW required: For a centered pressure anti-node the distance is equal to $n\lambda$, the particles will be forced away from the channel center. While for a centered node the distance is equal to $(n + 1/2)\lambda$, and the particles will be focused at the channel center.

The IDTs are fabricated using image reversal photolithography and lift-off by thin film evaporation (see fabrication protocol in Appendix B. The IDTs consist of a 5 nm layer of Ti, deposited on a piece of Y-cut 128° orientated LiNbO$_3$ surface, and a 80 nm layer of Au deposited on top of the Ti. The IDTs are deposited on the

Table 5.1: A characteristics overview of all transducer designs. The top four designs are uniform straight IDTs, while the last two are FIDTs.

Design	Pitch	Theoretical Resonance Frequency	Reflectors	IDT Spacing
IDT_A	100 μm	39.79 MHz	No	2500 μm
IDT_B	100 μm	39.79 MHz	Yes	2500 μm
IDT_C	100 μm	39.79 MHz	Yes	7500 μm
IDT_D	50 μm	79.58 MHz	Yes	2500 μm
$FIDT_A$	100 μm	39.79 MHz	No	1200 μm
$FIDT_B$	50 μm	79.58 MHz	Yes	1500 μm

LiNbO$_3$ in such a way that the direction of SAW propagation is in the X-direction of the saggital XZ-plane.

5.1.1   Uniform IDTs

The first design for the uniform pair of IDTs, IDT_A, have electrode widths and spacing of 25 μm and therefore a 100 μm pitch. The IDT_A design consist of two facing IDTS with a space between them (referred to as the IDT spacing) of 2500 μm. This corresponds to 250 wavelengths of the generated SAWs, resulting in a pressure node at the center of the microfluidic channel when aligned in between the IDTs. The IDT spacing for the IDT_A pair is measured from the edge of the last electrode finger on one IDT to the edge of the closest electrode finger on the opposite IDT. Design IDT_B, IDT_C and IDT_D have a different design in that their IDT spacings are measure from the center of the last electrode on one IDT to the center of the first electrode on the opposite IDT. IDT_B, IDT_C and IDT_D also differs from IDT_A in that there are reflectors added to the designs to decrease insertion-loss in the device. IDT_C differs only from IDT_B in that the IDT spacing is 7500 μm, instead of 2500 μm. IDT_A, IDT_B and IDT_C have the same electrode width and spacing. According to the theory for IDTs (Chapter 3), all of these three designs will have a resonance frequency of 39.79 MHz. AutoCAD designs of IDT_A and IDT_B are shown in Figure 5.3 **A** and **B**, respectively. IDT_D has the same kind of design as IDT_B, except that the electrode spacing and width is 12.5 μm, resulting in a 50 μm pitch. This device will have a theoretical resonance frequency corresponding to 79.58 MHz. The AutoCAD design is shown in Figure 5.3 **C**.
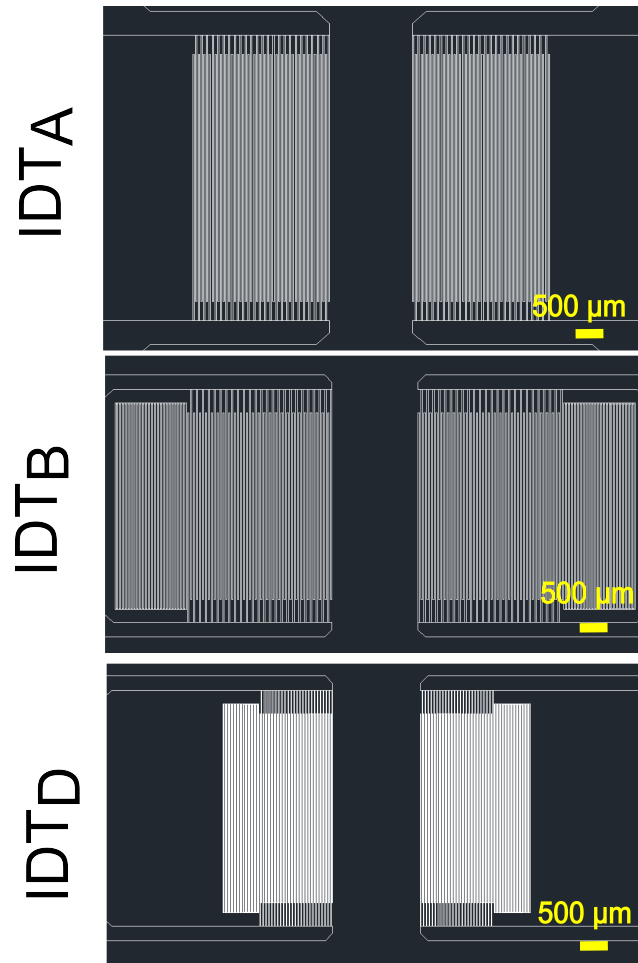
Figure 5.3: **Uniform IDT Design**
IDT$_A$, with a 100 µm pitch, corresponding to a 39.79 MHz resonance frequency.
IDT$_B$ has the same pitch and resonance frequency as IDT$_A$, but additional reflector
electrodes are added to the design. **IDT**$_D$ with a 50 µm pitch, corresponding to a
79.58 MHz resonance frequency. Reflector electrodes are also added to this design.
The spacing between the IDTs in design IDT$_A$, IDT$_B$ and IDT$_D$ are all 2500 µm.
IDT$_C$ is not shown, but is identical to IDT$_B$ except for a IDT spacing of 7500 µm.

5.1.2 Double IDT Device: Focusing and Separating

To improve the separation of particles away from the center of the microfluidic channel, all particles should be centered both laterally and vertically in the channel prior to being acted upon by the pressure nodes [62]. In addition to focusing the particles by sheath flow, one may achieve a better separation efficiency by using a pair of IDTs that focus the particles by acoustophoresis beforehand.

The double IDT pair design consists of two pairs of IDTs: the first pair use SSAWs to center the particles, while the second IDT pair separates the particles. The AutoCAD design for the double IDT device (created by Jonas M. Ribe) is shown in Figure 5.4, together with a optimal aligned microfluidic channel. The IDT pair closest to the inlets are designed so that the two closest electrode fingers on the IDTs are not ground-electrode to signal-electrode, but signal-electrode to signal-electrode, as shown in Figure 5.4 **B**. This way, the generated SSAW will have a phase shift of 180°, generating a pressure anti-nodes at the channel's center. Hence, the particles will be forced towards the center of the channel. The second IDT pair will be located after the first IDT pair. These IDTs will have a ground-electrode and a signal-electrode as the two closest electrode-fingers of the IDTs, as shown in Figure 5.4 **C**. The IDTs will generate a pressure node at the center of the channel, forcing the particles away from the center. The focusing IDTs are 5.2 mm long, while the separation IDTs are 3.2 mm long. There are two designs for the double IDT, one with IDT_B designs and one with IDT_D designs. The triangles and star shapes in the design (Figure 5.4 **A**) are alignment marks, making it easier to align the PDMS channel to the LiNbO$_3$ wafer.

5.1.3 Focused IDTs

A focused IDT (FIDT) consists of curved electrode fingers. Due to the FIDTs conventional structure the SAWs will be focused at a focal point. Two facing identical FIDTs, with a IDT spacing equal to two focal lengths, will generate a higher pressure amplitude at their common focal point. From Equation 3.4 this should result in an increased acoustic radiation force [63].

There are two designs for the FIDTs: The first design, FIDT$_A$, has a 100 μm pitch, hence a theoretical resonance frequency at 39.79 MHz. The second design, FIDT$_B$, is a SPUDT with additional thicker electrodes added to the ground electrode and signal electrode of the two opposite facing FIDTs, respectively. The width of the reflectance electrodes are set to $\lambda/4$, the width of the electrode fingers
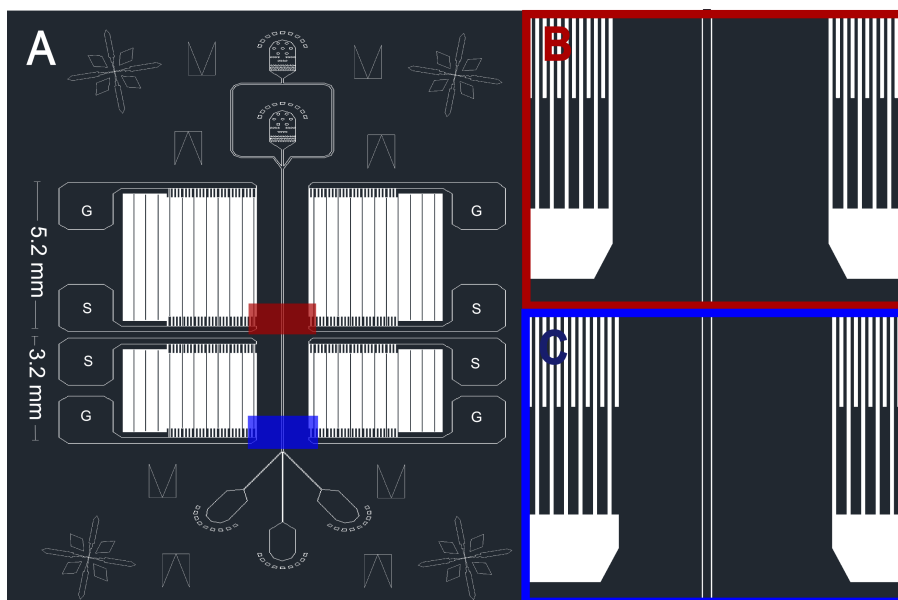
Figure 5.4: **Double IDT Device**
A: 5.2 mm long IDTs with reflectors is located closest to the inlet. These IDTs will create a pressure anti-node at the channel center. The pressure nodes will force the particles towards the center of the channel, hence focusing them. The design of a 60 μm channel is added to the double IDT device design, to show how the IDTs and the PDMS channel should align. Water as sheath flow is injected through the top inlet, and particles though the second inlet. The IDT pair for focusing (**B**) has the closest electrode fingers aligned as signal-electrode to signal-electrode, while the IDT pair for separation (**C**) has the closest electrode fingers aligned as ground-electrode to signal-electrode.
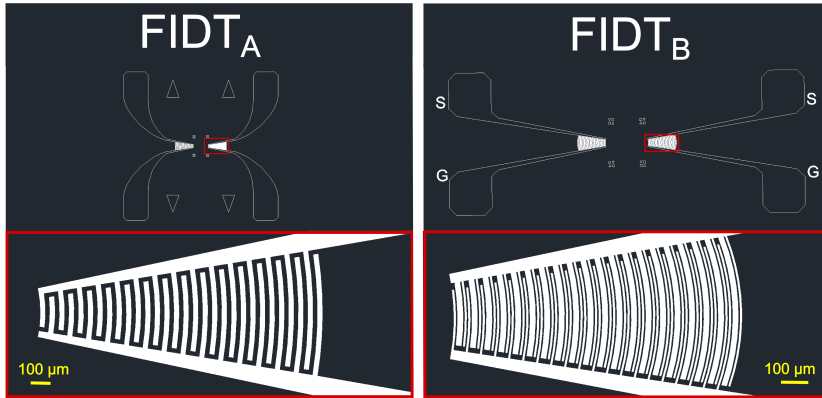
Figure 5.5: **FIDT Design**
FIDT$_A$ has a 100 µm pitch, corresponding to a 39.79 MHz resonance frequency.
FIDT$_B$ is a SPUDT with reflectors. This design has a 50 µm pitch and a 79.58 MHz corresponding resonance frequency.

are $\lambda/8$ and the electrode spacings are set to $3\lambda/16$. FIDT$_B$ has a 50 µm pitch, with a theoretical resonance frequency of 79.58 MHz. Both FIDT pairs are designed so that the focal point is located at half the gap length between the FIDT pair. The IDT spacing is 1500 for the FIDT$_B$, measured from the center of the last electrode on the first FIDT, to the center of the first electrode on the opposite FIDT. FIDT$_A$ has a IDT spacing of 1200 µm, measured from the inner end of each electrode. The FIDT$_A$ and FIDT$_B$ design are shown in Figure 5.5 **A** and **B**, respectively. The triangles in the design are alignment marks.

5.2 Microfluidic Channel

The micro channels are made of PDMS, fabricated using photolithography and soft lithography. The channels are made with Sylgard 184 PDMS-kit, and a detailed fabrication protocol can be found in Appendix B.

The microfluid channel are designed in AutoCAD by Jonas M. Ribe. The design for a 60 µm wide channel is shown in Figure 5.6. This specific design is made for IDT pairs that generate SAWs with a wavelength of 100 µm. When perfectly aligned with the IDT pair, the pressure node (anti-node) will located at the center of the channel, while anti-nodes (nodes) will be located close to the channel walls. An equivalent design with a 30 µm channel width is also made, specifically for IDTs generating SAWs with wavelengths of 50 µm. A third equivalent design with 120 µm
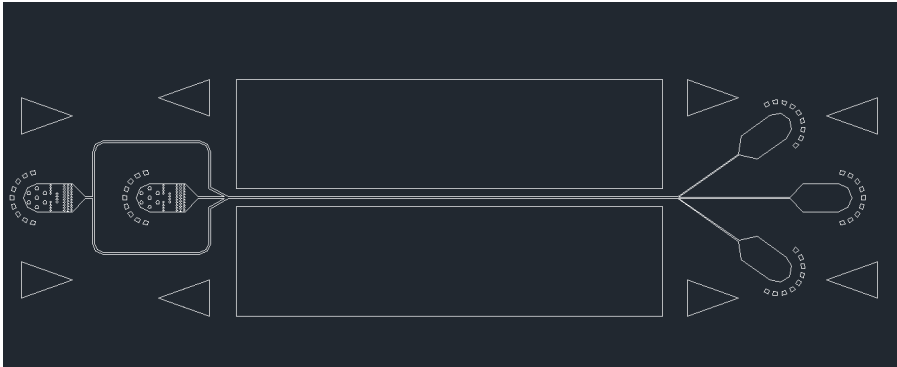
Figure 5.6: **Design PDMS Micro Channel**
AutoCAD drawing of a PDMS design with a 60 µm wide micro channel. The rect-
angles on both sides of the channel and the triangles are helping geometries for
alignment. The channel has two inlets to the left and three outlets to the right.
Particles are inserted though the center inlet (inlet 2) and purifies water is used as
sheat flow, inserted into the side inlet (inlet 1). The micro structures in the inlets
acts like small filters for larger particles. The design has three outlets: the center
outlet (outlet 2) and the two side inlets (outlet 1 and 3).

channel width is made to characterize the effect of several pressure nodes in the
channel. The triangles in the design are alignment marks, complimentary to the
alignment marks on the IDT designs.

There is also a version of all these channels where there are 3 inlets, one for
particles and two separate for the side sheath flows. This is to be able to adjust the
sheath flows differently, to manually center the flow of particles.

5.3   Alignment markers

Both the IDT and microfluidic channel designs have alignments marks. These are
used during the plasma bonding process, to easier align the channel in the center
in between the IDTs. Due to the length of the channel for the focusing and separa-
tion design, an additional photolithography mask is made, consisting only of the
alignment triangles seen in the channel design. After fabricating the two IDT pairs
on LiNbO$_3$ one can use photolithography to create triangles of SU-8 on top of the
LiNbO$_3$. These features can then click in place with the negative triangles in the
PDMS-channel when aligning the components.

5.4   Signal Mount

A microscope glass slide is used as a substrate for the signal mount, with two equal
sections of three gold electrodes. A glass slide was chosen as substrate with an
intention of fitting the final device on a microscope holder. A SMA connection is
soldered onto each side of the slide, connecting the two side-electrodes to ground
and the center electrode to the SAW generating signal (see Figure 5.2). The elec-
trodes on the signal mount are connected to the IDTs by wirebonding.

6 | Experimental Details

The experimental setup is shown in Figure 6.1. 0.5 µm Polystyrene Polybead®
(2.52% solids-latex in 5 mL) and 3.0 µm Polystyrene Polybead® (2.60% solids-latex
in 5 mL) by polyscience were diluted in MQ water, and the solution put into a BD
5 ml syringe. In later experiments 0.21 µm polystyrene (540,600) Suncoast Yellow
(1.05% solids in 10 mL) and 0,96 µm polystyrene (480,520) Dragon Green Fluores-
cence (1% solids in 10 mL) uniform dyed microspheres from Bangs Laboratories
were diluted in MQ water containing 0.1% tween, and injected in a BD 5 ml syringe.
A SCI syringe tube, with a 0.86 mm inner diameter, was connected to the syringe
and filled completely with the solution containing the particles. The syringe tube
was connected to the center inlet, already filled with MQ water in the fabrication
step to keep the micro channels hydrophilic and to prevent air bubbles from being
trapped inside the channel. Another syringe was filled with water and connected
to the sheet flow inlet. Both syringes were mounted on Harvard Apparatus PHD
ULTRA syringe pumps.

A KEYSIGHT 33600A waveform generator, referred to as the signal generator,
generated a sinusoidal wave-signal at a given frequency and intensity. The fre-
quency limit for the signal generator is 80 MHz for this model. The signal was
amplified by a MINI CIRCUITS 15542 Model nr. ZHL-5W-1 amplifier and split into
two BNC cables. The cables are connected to the SMA connectors on the signal
mount. The amplifier was powered by 24 V and 3.0 A. The final acoustophoretic
device was put on the mount of a Olympus IX70 microscope. The microscope has
filters corresponding to the emission peak of the two fluorescence particles, so that
each particle type could be observed separately. A CANON EOS 60D camera and a
Photron FASTCAM SA3 Model 120K high speed camera is connected to the micro-
scope.

The syringe pumps, signal generator and Canon digital camera were all con-
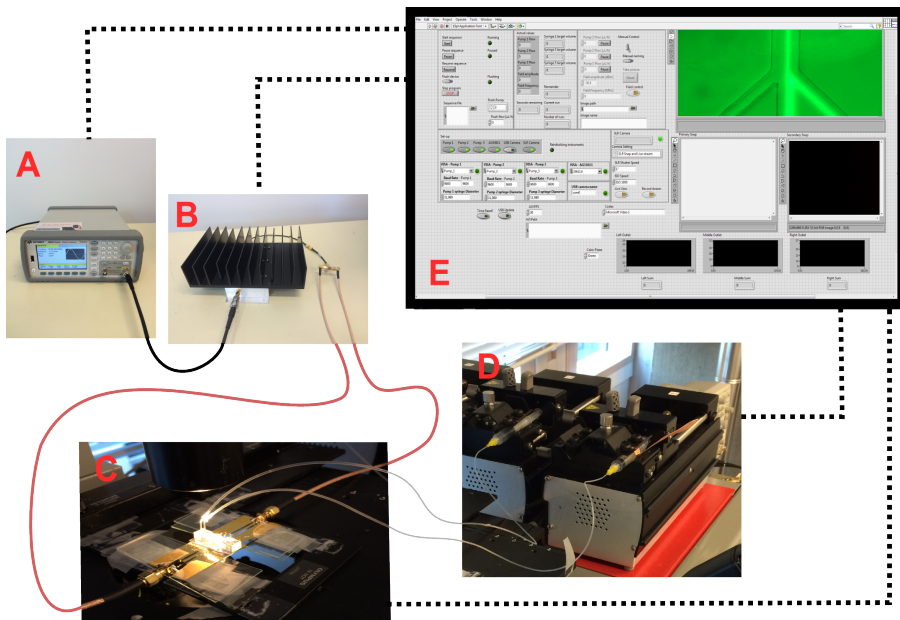
Figure 6.1: **Experimental Setup**
A: A voltage signal is generated by a KEYSIGHT 33600A waveform generator. **B:** The signal is amplified with a MINI CIRCUITS 15542 Model nr. ZHL-5W-1 amplifier, and split into two signals. **C:** The two signals are connected to SMA connectors on either side of a acoustophoretic device, leading the signal through gold electrodes and wirebonding to the IDTs. A CANON EOS 60D camera and a Photron FAST-CAM SA3 Model 120K high speed camera is connected to the microscope, and can transmit images and videos to a computer. **D:** The sample containing the particles, and the sheath flow fluid, are connected to the inlets of the device. The fluid flow is driven by Harvard Apparatus PHD ULTRA syringe pumps. **E:** All device are remotely driven by a graphic user interface, created by Nils Refstrup Skov.

trolled remotely by a graphical user interface, developed by Nils Refstrup Skov [46] as part of his master thesis and as a collaboration project with the Theoretical Microfluidics Group at the Technical University of Denmark and the Microfluidics Research Group at NTNU. Later on, Skov implemented an extension to the program which measures the light intensities at the outlets. Comparing the measurements with the overall light intensity for all outlets, the program computes a quantitative measurement of the concentration of fluorescence particles at each outlet. However, the extension was developed too late in this project to be used for our experiments.

6.1 Network Analyzer

An Agilent E8361A PNA Network Analyzer was used to measure the frequency response of IDT devices. All measurements from the network analyzer were completed by Terje Mathiesen at the Department of Electronics and Telecommunications at NTNU. $.s2p$ files, containing scattering parameters (S-parameters), were extracted from the network analyzer and a written MATLAB script plots the frequency response. The reflectance S-parameters S_{11} and S_{22} are measurements of the signal reflectance at input 1 and a input 2, respectively. While the transmission S-parameters S_{12} and S_{11} measures the signal gain or loss at input 1 for a signal sent in through input 2, and vice versa.

6.2 Frequency Finder

Frequency Finder is a LabVIEW program designed to map the resonance frequency for a device, created by Nils Refstrup Skov [46]. The amplified signal is connected to one of the SMA connections on the device, bonded to one of the IDTs. The other SMA, connected to the complimentary opposite facing IDT, is connected to the oscilloscope. At the graphic user interface the frequency range, signal amplitude and a number N of measuring points are chosen by the user. A signal, with varying frequency within the given range is introduced to the IDT. The oscilloscope measures the signal that is generated in the passive IDT from the SAW that is created by the active IDT. Hence, N number of frequencies and corresponding response I are measured and recorded. The final response measurements are given in mV$_{pp}$, and saved as a CSV file.

The measurements from Frequency Finder were extracted and loaded to a written MATLAB script. The frequency response in voltage gain (dB) was calculated

with respect to the initial generated signal I_0. These measurements were further plotted together with the measurements from the network analyzer. I_0 is equal to 50.230 mV$_{pp}$ (-22 dBm), which was the signal generated at the signal generator. The ZHL-5W-1 data sheet [64] states that the amplification gain is approximately 46 dB for frequencies in the range between 10 and 100 MHz. The oscilloscope measured the signal using a 10X probe in mV$_{pp}$. The voltage peak-to-peak signal, measured at the oscilloscope, was by default twice the value as the peak-to-peak value compared to the peak-to-peak values given at the signal generator. For our purposes the signal amplitude programmed at the signal generator was set as the reference value. The N measurements were plotted as:

$$Y_i(f_i) = 20 \log_{10}\left(\frac{I_i(f_i)}{I_0 \cdot 2 \cdot 10}\right), \text{ for i} = 1,\dots,\text{N} . \tag{6.1}$$

I_i is the frequency response measured at frequency f$_i$, measured in mV. In the denominator the factor 2 is accounting for the peak-to-peak oscilloscope value, which is by default measured as twice the corresponding value generated at the signal generator. The factor 10 is accounting for the 10X probe amplification.

Frequency Finder measures the response at one port (or input) when a signal with different frequency values are sent into the other port, corresponding to the transmission S-parameters S$_{12}$ and S$_{21}$. However, to measure the reflectance S-parameters S$_{11}$ and S$_{22}$ a pulse have to be sent to one port and then the reflectance of the pulse have to measured at the same port. The oscilloscope or signal generator were not capable of sending and measuring signals at the same time, hence Frequency Finder did only measure the S$_{12}$ and S$_{21}$ S-parameters for this experimental setup.

6.3   General Experimental Setup

The device was rigged to the experimental setup. The syringe pumps were set to 200 µL/h for a couple of minutes to reach a steady-state flow of the particles from the inlet, through the separation channel and out of the outlets. When a steady-state flow was achieved, the flow rate was set to a lower rate. Usually 20µl/h – 40 µl/h for the center flow and the double rate for the sheath flow allowed a nice centering of particle flow in the channel. If not, the flow rates were adjusted to center the flow of particles.

The specific resonance frequency for the device was determined using Frequency Finder. The signal was tgenerated with a set frequency equal to the res-

onance frequency, and the signal was measured at the device by the oscilloscope probe to check for unexpected signal-loss in the setup. The effect of the SSAW, and the displacement of particles inside the channel, was observed though the oculars of the microscope or by the high speed camera. The high speed camera and the digital camera were used to record videos and images for the characterization of the separation.

7 | Results and Discussion

Throughout this chapter all results are presented, compared and discussed. The Experimental Adjustments section is added to give an overview of certain limitations and criterion that were made prior to the frequency response, presented in the second section. Results from acoustophoretic experiments are presented in the third section. Additional results found for fabricating techniques and processes are found in Appendix A.

7.1 Experimental Adjustments

Due to observable signal losses for our experimental setup, frequency response measurements of the ZHL-5W1 amplifier were conducted. The measurements were made from connecting the oscilloscope to different sections of the experimental setup and running frequency finder over a range of frequencies, from 20 MHz to 80 MHz. Measurement plots are presented in Figure 7.1.

An oscilloscope probe is used to measure the amplified signal at the IDTs of a device that is connected to the setup. Table 7.1 presents the measured voltage over a 100 μm pitch IDT, for two incoming signals. The signal are generated at -22 dBm and -16 dBm before amplified, both with a frequency of 39.8 MHz. The unit dBm describes the power ratio in decibel (dB) referenced to one milliwatt (mW), and will be used to express the power of the signal throughout this work.

The data sheet for the ZHL-5W-1 amplifier states that the signal will be amplified with 46 dB, when operated at 24 V [64]. This means that a -22 dBm (50.230 mV$_{pp}$) signal should be amplified to 24 dBm (10.022 V$_{pp}$). However, the results from the frequency response show that the gain of the system is frequency dependent. For our system the measured gain for a generated 39.79 MHz signal is 48 dB. Hence, the signal measured at the device should be 26 dBm (12.62 V$_{pp}$). The gain for a 79.8 MHz signal with the same generated amplitude is measured to 42 dB, which
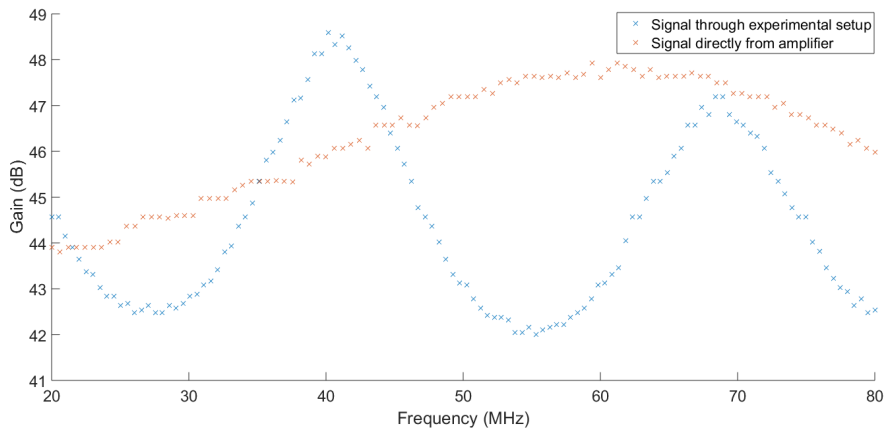
Figure 7.1: **Amplification Frequency Dependency**
Frequency Finder was used to measure the amplified signal for our experimental
setup, over the frequency range of 20 MHz to 80 MHz. The blue curve shows the
measurements when the signal from the amplifier goes straight to the oscilloscope
for measurement readings. The red curve shows the frequency response for the
complete system, when the device is bypassed. All measurements are shown in
dB, compared to the output signal amplitude of the signal generator. The output
signal amplitude is set to -22 dBm, corresponding to 50.230 mV$_{pp}$. When the signal
is sent through the complete experimental setup, the gain is measured to approxi-
mately 48 dB and 42 dB for the respectively frequencies 39.8 MHz and 79.6 MHz.

Table 7.1: Measured amplitude over a 100 μm pitch IDT, for a -22 dBm and a -
16 dBm signal at 39.8 MHz, over a 100 μm pitch IDT. A signal probe, connected to
the oscilloscope, is used to measure the signal. The probe measure the V$_{pp}$ at the
IDTs wire bonding pad, and the signal mount ground plane is used as the probe
reference.

Amplitude generated at signal generator	Measured signal, left IDT	Measured signal, right IDT
-22 dBm	1.22 V$_{pp}$	1.22 V$_{pp}$
-16 dBm	2.50 V$_{pp}$	2.50 V$_{pp}$

Table 7.2: The resonance peak from the frequency response measurements for the straight IDTs: the frequency at the corresponding maximum effect for design IDT_A, IDT_B, IDT_C and IDT_D. IDT_A, IDT_B and IDT_C have a 100 µm pitch, corresponding to a generated SAW with theoretical resonance frequency at 39.79 MHz. IDT_D has a 50 µm pitch, corresponding to a theoretical 79.58 MHz The Frequency Finder response measurement for IDT_C have a difference in value from S_{12} to S_{21} by 1.72 dB.

| | Network Analyzer | | Frequency Finder | |
Design	Resonance Frequency f_r	Response	Resonance Frequency f_r	Response
IDT_A	39.11 MHz	-5.87 dB	NA	NA
IDT_B	38.73 MHz	-4.64 dB	38.82 MHz	-8.59 dB
IDT_C	38.78 MHz	-5.77 dB	38.57 MHz	-5.46/-7.18 dB
IDT_D	78.66 MHz	-7.19 dB	78.54 MHz	-4.09 dB

results in a 20 dBm (6.324 V_{pp}) signal at the device.

A frequency response was measured directly from the signal generator with a -22 dBm (50.230 mV_{pp}) signal output over the same frequency range. The average value for the measurements was 46.72 mV_{pp} with a variance of 0.42, showing that the value is a lower than what is set at the signal generator.

This data presents the difficulty in characterizing the true effect of the signal at the IDTs, and the difficulty in comparing the input effect for different experiments and devices. However, the most important thing to recognize from these measurements is that the signal seems to be equal for both IDTs on the separate sides of the device (Table 7.1). Because of the amplifications frequency dependency, we will only refer to the generated amplitude of the signal throughout this work, set at the signal generator.

7.2 Frequency Response

7.2.1 100 µm pitch IDTs

Frequency response measurements from the network analyzer and Frequency Finder are plotted for uniform IDT designs with 100 µm pitch: IDT_A (Figure 7.2), IDT_B (Figure 7.3) and IDT_D (Figure 7.4). All measurements were obtained without PDMS channels bonded to the devices. An overview of the resonance frequency and the corresponding measured response is shown for the straight IDT designs in Table 7.2.

One can see from the plots that the S_{12} and S_{21} parameters are very symmetri-

Figure 7.2: **Frequency Response IDT$_A$**
The figure presents the magnitude of frequency response for the 100 μm pitch IDT device, over the frequencies range 28 MHz to 48 MHz. The measurements within the outlined red square are shown in the bottom plot. The blue and purple lines shows the S_{11} and S_{22} respectively for input 1 and input 2. A significant drop in reflectance for both inputs are located at 39.20 MHz. The response at this frequency is -33.95 dB for S_{11} and -25.04 dB for S_{22}. The red and yellow lines shows the S_{21} the S_{12} parameter, respectively. Both S_{12} and S_{21} have a very similar response, with a resonance peak at 39.11 MHz. The frequency response at this range is -5.867 dB for both parameters. No Frequency Finder measurements were collected from this device.
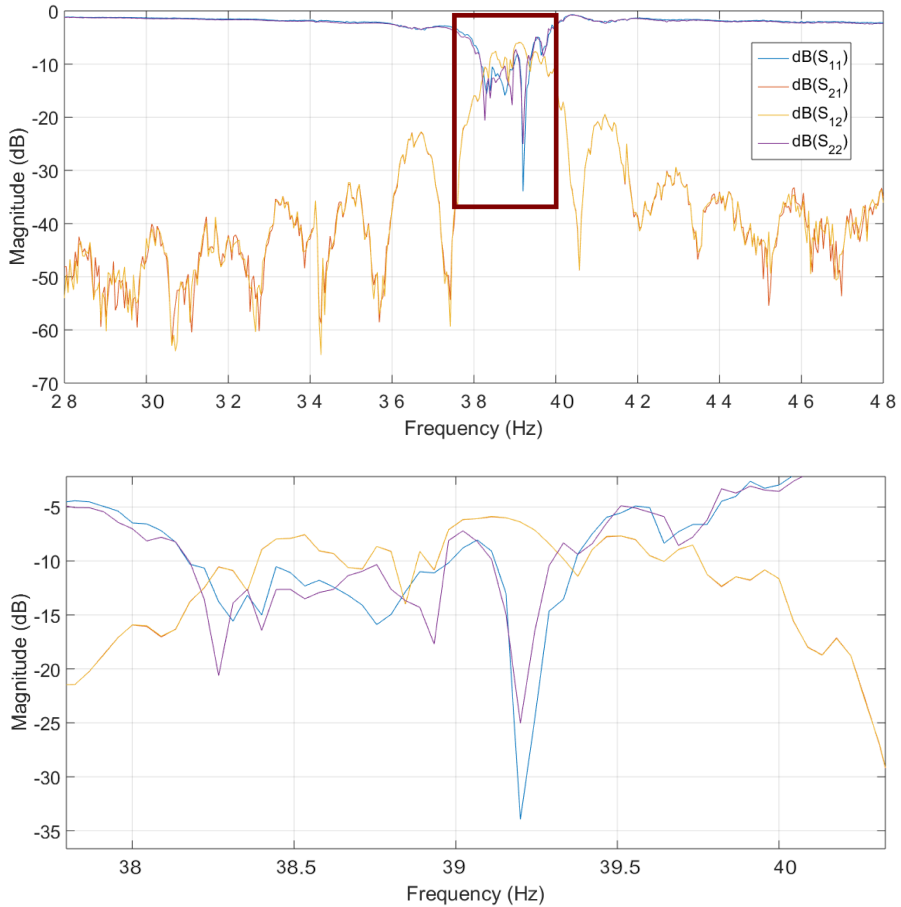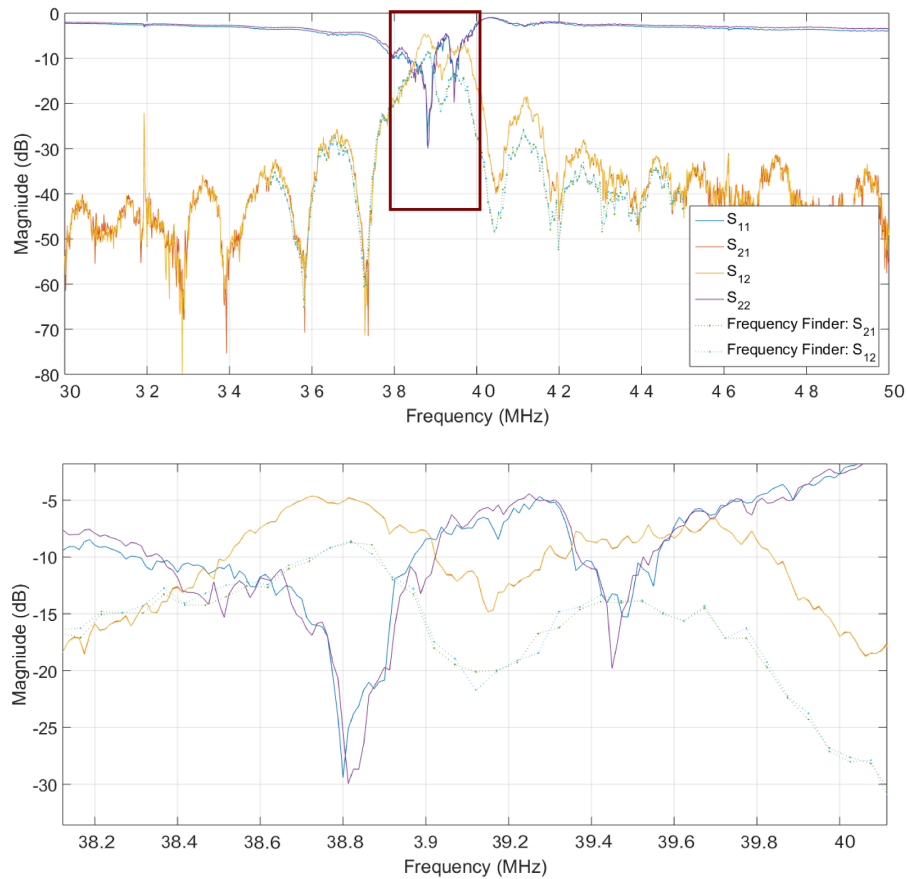
Figure 7.3: **Frequency Response IDT$_B$**
The figure presents the magnitude of frequency response for the 100 μm pitch IDT device with reflectors, over the frequencies range of 28 MHz to 48 MHz. The measurements within the outlined red square are shown in the bottom plot. The blue and purple lines shows the S$_{11}$ and S$_{22}$ respectively for input 1 and input 2. A significant drop in reflectance for both inputs area located at 38.8 MHz. The response at this frequency is -29.4 dB for S$_{11}$ and -29.94 dB for S$_{22}$. The red and yellow lines shows the S$_{21}$ the S$_{12}$ parameter, respectively. Both S$_{12}$ and S$_{21}$ have a very similar response, with a resonance peak at 38.73 MHz. The frequency response at this range is -4.663 dB for both parameters. Additional measurements for S$_{21}$ the S$_{12}$ parameters are found using Frequency Finder for the same device. These are shown in dotted lines, and have a very similar response. A resonance peak for both measurements is found at 38.82 MHz, with a -8.59 dB response.
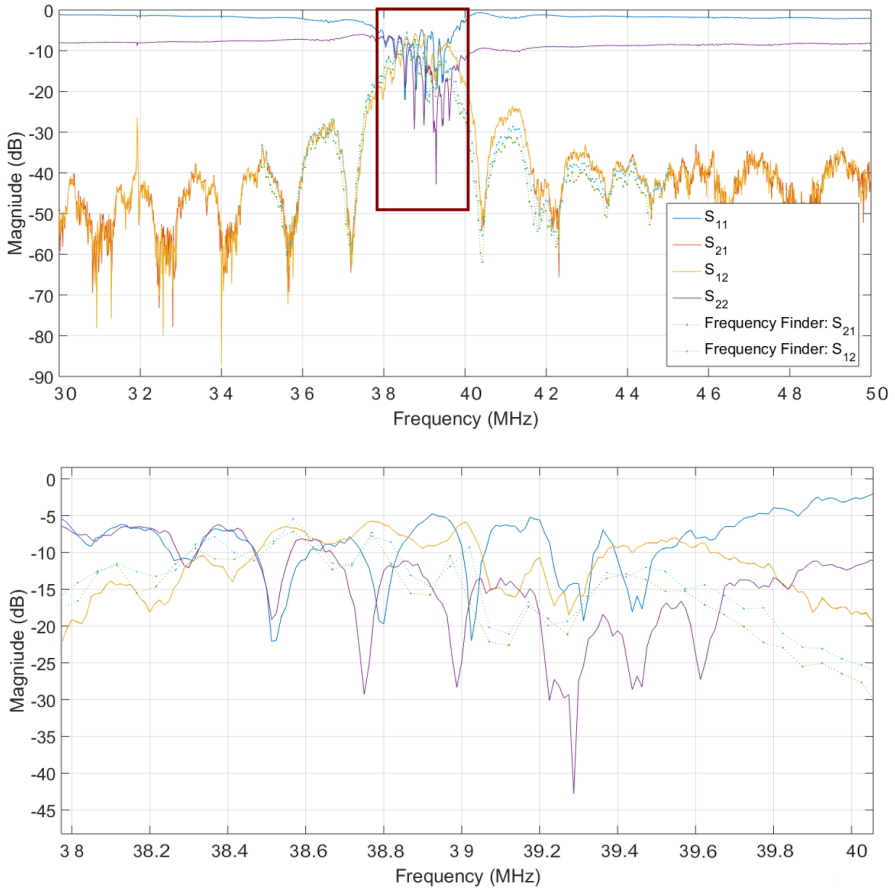
Figure 7.4: **Frequency Response IDT**$_C$

The figure presents the magnitude of frequency response for the 100 μm pitch IDT device with reflectors and additional IDT gap, over the frequencies range of 28 MHz to 48 MHz. The measurements within the outlined red square are shown in the bottom plot. The blue and purple lines shows the S_{11} and S_{22}, respectively for input 1 and input 2. There are several drops in reflectance for both parameters around the are of resonance. However the most significant drops are located at 39.03 MHz and 38.51 MHz for S_{11}, with a response of -22.1 dB. The most significant drop in reflectance for S_{22} is at 39,92 MHz, with a response of -42.80 dB. The response at this frequency is -29.40 dB for S_{11} and -29.94 dB for S_{22}. The red and yellow lines shows the S_{21} the S_{12} parameter, respectively. Both S_{12} and S_{21} have a very similar response, with a resonance peak at 38.78 MHz. The frequency response at this range is -5.77 dB for both parameters. Additional measurements for S_{21} the S_{12} parameters are found using Frequency Finder for the same device. These are shown in dotted lines, and have a very similar response. A resonance peak for both measurements is found at 38.57 MHz, with a -5.46 dB and -7.18 dB response for S_{12} and S_{21}, respectively.

cal for each IDT design, generating the same response for a range of frequencies. All the IDT designs have a resonance frequency which corresponds closely to the theoretical value for their design, This implies that the fabrication protocol works well for these designs, and that the fine micrometer structures of the IDTs are fabricated without defects. From the results one can see that the resonance frequency measured by Frequency Finder is at the most off by 0.49% (For IDT_C) compared to the network analyzer.

The two facing IDTs for the IDT_C design have a difference in response for the Frequency Finder measurements. However, this discontinuity in symmetry do not appear in the network analyzer measurements. For all purposes, the network analyzer measurements should be more accurate for measuring the amplitude of the response, compared to Frequency Finder. This is because the device is coupled directly to the network analyzer when the measurements are computed, so any error should remain only in the device itself. Our experimental setup has a lot more components in the system, in addition to the device itself, that may affect the measured signal. This is demonstrated earlier in this chapter when comparing the measured and theoretical gain for the system.

The reason for the improved response for IDT_B, compared to IDT_A, may be the additional reflectors in the design. However, the IDT_C design, which also have reflectors, measures a lower response compared to the IDT_B design. This may be caused by the spacing between the IDTs, being 5 mm wider than the IDT spacing of design IDT_B. No PDMS was bonded to the devices that were tested for frequency response, and the $LiNbO_3$ surface is only in contact with atmospheric air. With a attenuation coefficient for a leaky 38.76 MHz SAW of approximately 0.29 m^{-1} for air (Table 3.1), the theoretical signal loss over a distance 7500 µm is 100.14% compared to a signal loss for 2500 µm. Hence, the increased IDT spacing can not be the single cause for this loss. The IDT_C design was harder to fabricate on the scribed $LiNbO_3$ wafer, compared to the other designs. Because of the wider design, the IDTs were located close to the edge of the $LiNbO_3$ wafer piece, where more irregularities are present. This could cause a defect in the reflectors, which could explain why the response for IDT_C is lower compared to the other designs with reflectors.

7.2.2 50 µm pitch IDTs

Figure 7.5 shows the measured frequency response for the IDT_D design. All measurements were obtained without the PDMS channels bonded to the devices.

The response of IDT_B is measured from 40 MHz to 90 MHz, where the frequen-
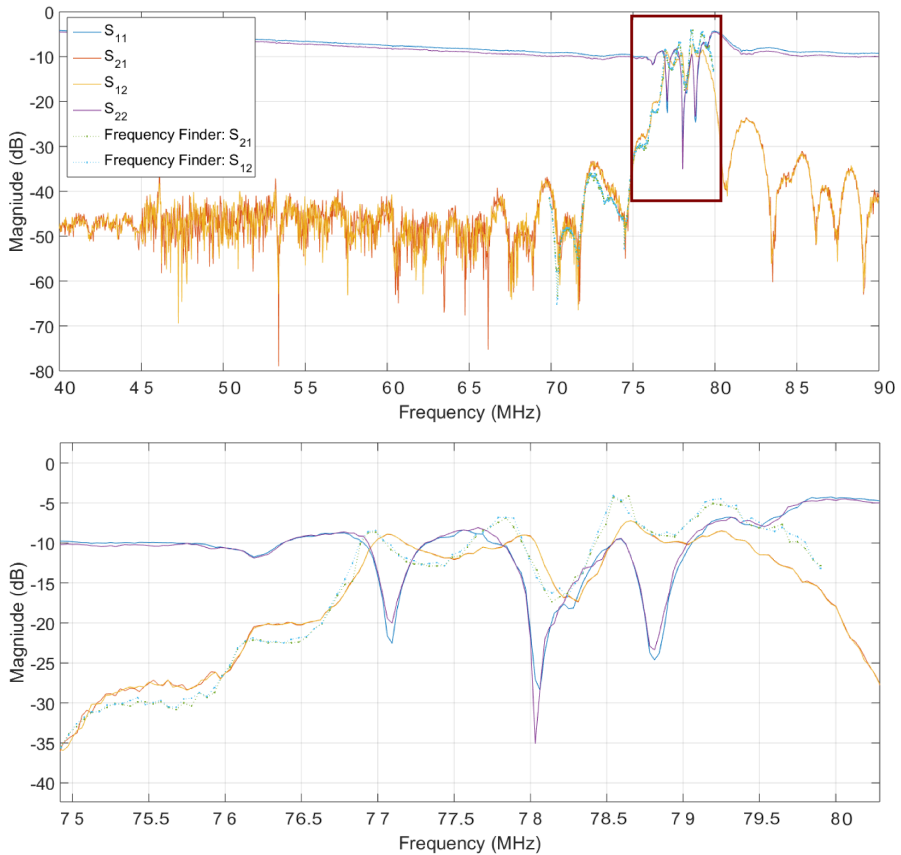
Figure 7.5: **Frequency Response IDT**$_D$

The figure presents the magnitude of frequency response for the 50 μm pitch IDT device with reflectors, over the frequencies range of 40 MHz to 90 MHz. The measurements within the outlined red square are shown in the bottom plot. The blue and purple lines shows the S_{11} and S_{22}, respectively for input 1 and input 2. A significant drops in reflectance is found at 78.06 MHz and 78.03 MHz, respectively for S_{11} and S_{22}. At these frequencies the response is -28.85 for S_{11} and -35.08 dB for S_{22}. The red and yellow lines shows the S_{21} the S_{12} parameter, respectively. Both S_{12} and S_{21} have a very similar response, with a resonance peak at 78.66 MHz. The frequency response at this range is -7.188 dB for both parameters. Additional measurements for S_{21} the S_{12} parameters are found with Frequency Finder for the same device. These are shown in dotted lines, and have a very similar response. The resonance peak for both S_{12} and S_{21} is located at 78.54 MHz, a response of -4.09 dB.

cies of resonance are easily observed by the response peaks in Figure 7.5. The S$_{12}$ and S$_{21}$ parameters are symmetrical, and the data from Frequency Finder are very similar to the data from the network analyzer, as for the 100 μm pitch designs.

Overall, the results favors the IDT$_B$ design when it comes to frequency response. It has the best response at its resonance frequency, compared to the other designs. IDT$_C$ is the least favorable design when comparing the resonance frequency responses, however the response is still comparable to the others. While IDT$_A$ and IDT$_D$ have a very similar response when comparing the resonance frequency response, IDT$_D$ has a recognizable decrease in response magnitude on either side of its resonance frequency. This is also the case for IDT$_C$. In contrary, both IDT$_A$ and IDT$_B$ reaches a plateau in frequency response for frequencies surrounding the resonance frequency. For these designs a small offset in frequency value from the resonance frequency will not have a huge impact on the response.

A change in effect cause by the difference in design of IDT gap measurements for IDT$_A$, compared to the other IDT designs (described in Chapter 5), is not recognized in these results. Hence, we can not conclude how this affects the generated SSAW.

While the frequency response data for all designs look promising, the IDT$_A$, IDT$_B$ and IDT$_D$ designs are further tested as components for the acoustophoretic separation device.

7.2.3 FIDTs

Figure 7.6 and Figure 7.7 show the measured frequency response for the FIDT$_A$ and FIDT$_B$ device. The theoretical resonance frequency is 39.79 MHz and 79.58 MHz, respectively. The range of frequencies, which the response is measured, spans from 29 Mhz to 48 MHz for the FIDT$_A$ device. For the IDT$_B$ device the range spans from 40 MHz to 90 MHz to characterize a broader spectrum of frequency responses than just the frequencies close to the predicted resonance.

For FIDT$_A$ the network analyzer measurements diverts in some sense from the frequency response measured with the Frequency Finder (see Figure 7.6). It should be noted that the measurements are obtained with two different devices; the first devices was damaged before measurements could be obtained from both instruments. The resonance frequency does not correspond for the two measurements. However, a local response peak is located in the Frequency Finder plot at the location of the network analyzer resonance frequency. This response peak at 39 MHz is -28.06 dB, a loss of 1.88 dB compared to the global Frequency Finder resonance
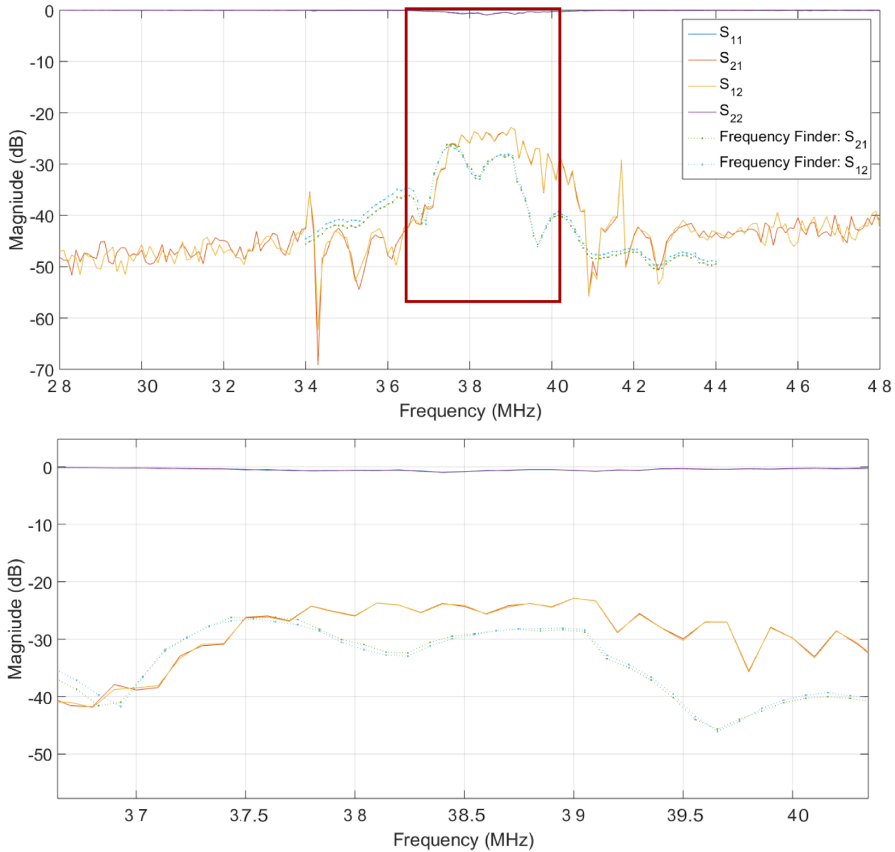
Figure 7.6: **Frequency Respons FIDT**$_A$

The figure presents the magnitude of frequency response for the 100 µm pitch FIDT device, over the frequencies range 28 MHz to 48 MHz. The blue and purple lines shows the S_{11} and S_{22} respectively for input 1 and input 2. A drop in reflectance for both inputs are located at 38,40 MHz. The response in reflectance at this frequency is -0.937 dB for S_{11} and S_{22}. The red and yellow lines shows the S_{21} the S_{12} parameter, respectively. Both S_{12} and S_{21} have a very similar response, with a resonance peak at 39.00 MHz. The frequency response at this range is -22.87 dB for both parameters. The blue and green dotted lines represent the Frequency Finder measurements for S_{12} and S_{21}. Both have a very similar response, with a resonance peak at 37.43 MHz, with a -26.22 dB response.
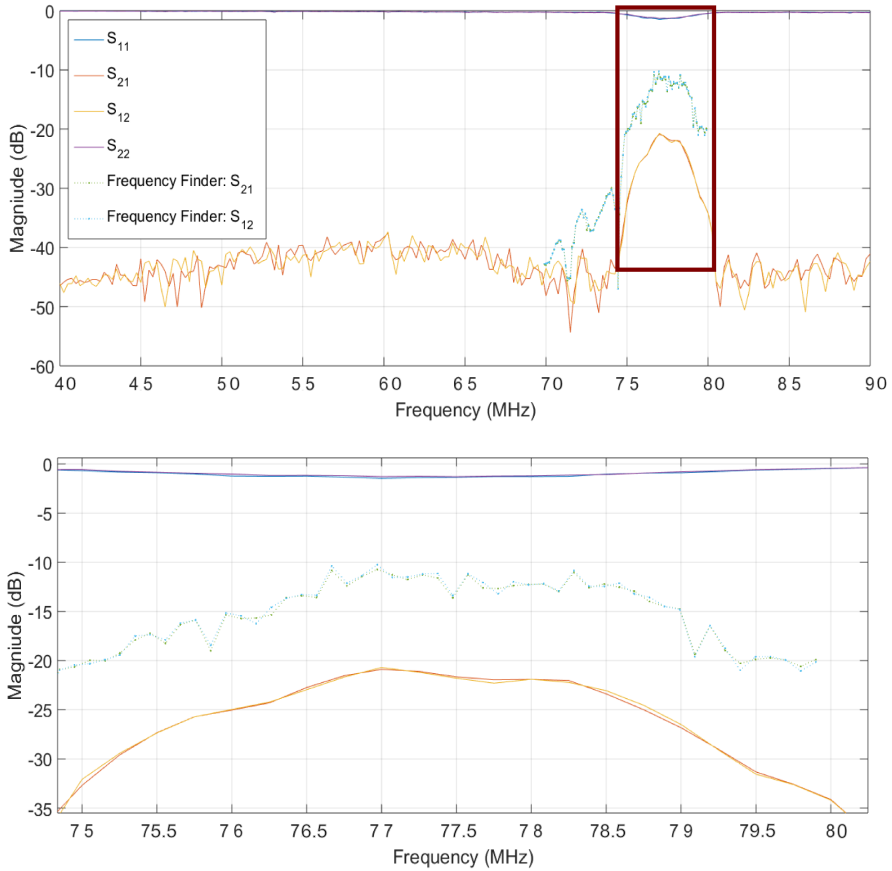
Figure 7.7: **Frequency Response FIDT**$_B$

The figure presents the magnitude of frequency response for the 50 μm pitch SPUDT device, over the frequencies range 40 MHz to 90 MHz. The measurements within the outlined red square are shown in the bottom plot. S_{11} and S_{22} are shown in the blue and red line, respectively for input 1 and input 2. The reflectance for both inputs is at its lowest for 77.50 MHz. The response at this frequency is -1.304 dB for S_{11} and S_{22}. The red and yellow lines shows the S_{21} the S_{12} parameter, respectively. The best frequency response for the network analyzer measurements is found for 77.00 MHz, with a response of -20.70 dB. The dotted lines represent the Frequency Finder measurements for S_{12} and S_{21}. The Frequency Finder measurements are from a different device than the one in which the frequency response of the network analyzer was measured. Both have a very similar response, with a resonance peak at 76.97 MHz. The frequency response at this frequency is -10.24 dB for both parameters.

Table 7.3: The resonance peak (i.e. the frequency at the corresponding maximum effect) from the frequency response measurements for the FIDT$_A$ and FIDT$_B$ designs. FIDT$_A$ has a 100 μm pitch, corresponding to a generated SAW with theoretical resonance frequency at 39.79 MHz. FIDT$_B$ has a 50 μm pitch, corresponding to a theoretical resonance frequency at 79.58.

	Network Analyzer		Frequency Finder	
Design	Resonance Frequency f$_r$	Response	Resonance Frequency f$_r$	Response
FIDT$_A$	39.00 MHz	-22.87 dB	37.43 MHz	-26.22 dB
FIDT$_B$	77.00 MHz	-20.70 dB	76.97 MHz	-10.24 dB

peak.

There are local response spikes in the network analyzer measurements, close to 34 MHz and 42 Mhz. These might be a result of specific implications with the first device, since no such peaks were found in the Frequency Finder measurements for the second device.

The frequency response for the FIDT$_B$ design (Figure 7.7) has a dominant peak around the measured resonance frequency of 77 MHz. This measurement is close to the theoretical resonance frequency of 79.58 MHz. The reflectance parameters S$_{11}$ and S$_{22}$ show only a slightly decrease on either side the resonance frequency.

Comparing FIDT$_A$ to FIDT$_B$, the response for frequencies close to the FIDT$_B$ resonance frequency is more stable and broader than the FIDT$_A$ design. If the signal is set to an offset of the resonance frequency of 0.5 MHz, the response for the FIDT$_A$ design may result in a loss of almost 7 dB. While the biggest loss for a similar frequency offset in the FIDT$_B$ design is less than half of that. The SPUDT design of FIDT$_B$ should theoretically result in a higher efficiency and response, which corresponds to these results.

Compared to the straight IDTs, the resonance peaks of the FIDT designs are not as sharp, but more broad. The resonance response is higher for the straight IDTs than for the FIDTs. This is probably the result of the curved FIDT design, which focuses the SAWs to a centered focal point. It is not the maximum response at this focal point that we are measuring, but the signal that is spread away from the focal point to the passive IDT. Hence, we should not expect a similar response for FIDTs and IDTs. It should also be noted that for a FIDT pair the passive FIDT is used to measure the response of the active FIDT. If instead a IDT was used to measure the response of a FIDT the results would be different, and a more accurate response

would most likely be measured.

7.2.4 Frequency Finder

The properties of Frequency Finder as a tool for obtaining characteristics for the devices should be noted. For our purposes of locating the resonance frequency of a device, the results show that Frequency Finder works well, compared to the measurements obtained from the network analyzer. This comes in handy, since the only additional equipment needed to run Frequency Finder is a LabVIEW license, which is inexpensive compared to a network analyzer. In addition, the simplicity of Frequency Finder allows us to obtain frequency response measurements in our laboratory, without the support of external laboratories or support. Even though the response amplitude from Frequency Finder and the network analyzer does not correspond entirely (Table 7.2 and Table 7.3), Frequency Finder is used in further experiments to find the resonance frequency for individual devices.

7.3 Acoustophoresis by SSAWs

7.3.1 Acoustophoresis Using IDT$_A$

During the first experimental phase of our project, the IDT$_A$ design was used on the acoustophoretic device. SAWs generated from the 100 µm pitch IDTs were tested on 3.0 µm and 0.5 µm Polybead® polystyrene particles. Microscope images of the experiment is shown in Figure 7.8. The signal was generated with an amplitude and frequency of -18 dBm and 39.2 MHz. For this experiment the center particle flow was set to 40 µL/h and the sheath flow to 60 µL/h. One can see that the particles are affected by the SSAW field by observing the change in lateral position. The particles follows a centered streamline when the field is off, while the 3.0 µm particles moves to the right side of the channel when the field is turned on. The 3.0 µm particles are easy to observe (Figure 7.8), while the 0.5 µm particles are only recognized as a density gradient compared to the fluid. The 0.5 µm particles exit through the center outlet when the field is turned on. Because of a pressure node appearing at the center of the channel, the particles are forced towards the anti-nodes located 25 µm to either side. However, most of the 3.0 µm particles move to the right side of the channel. This may be caused by a slight change in pressure of the two outlets during the experiment. A pressure gradient in the lateral direction may force the particles to move slightly to the right side of the channel. When entering the SSAW field they will naturally be moved further towards that side when
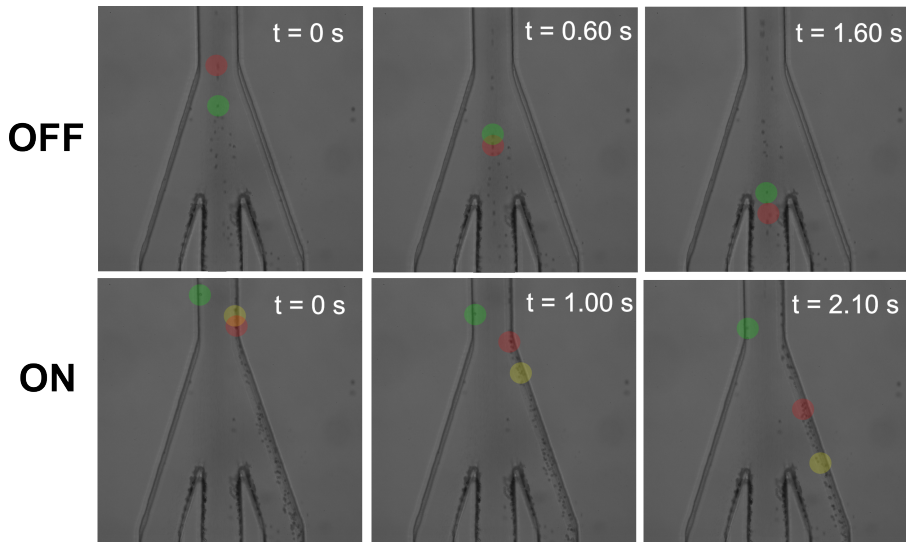
Figure 7.8: **IDT$_A$: Filtration of Particles**
The results show how SSAWs affect 3.0 µm and 0.5 µm particles, generated from a -18 dBm, 39.2 MHz signal. The center particle flow is set to 40 µL/h while the sheath flow is set to 60 µL/h. The channel is 60 µm in height and width, before merging out at the outlet. The highlighted circles follows the path of the marked particles through the time steps. 3.0 µm particles are easily observed, while 0.5 µm particles are only observable as a gray, dense shade. **OFF:** Particles in channel when SSAW field is off, during three time steps. **ON:** When SSAW field is turned on the particles are affected, shown during three time steps.

an anti-node appears in the center of the channel. Another reason for the particles to favor movement towards one side may be a slight offset in alignment between the PDMS channel and the LiNbO$_3$ during plasma bonding. Figure 7.11 illustrates how an offset in alignment can affect the system. If the alignment is off, so that the anti-node is located slightly to the left of the channel center, the initially centered particles will more likely be forced away from the pressure node, towards the right wall.

The IDT$_A$ design was also used to investigate if SSAWs could separate 1.0 µm (Polybead® by polyscience) from the 0.5 µm polystyrene particles. However, it was not possible to distinguish the two different particles in the microscope, both particle types appeared as gray density gradients.

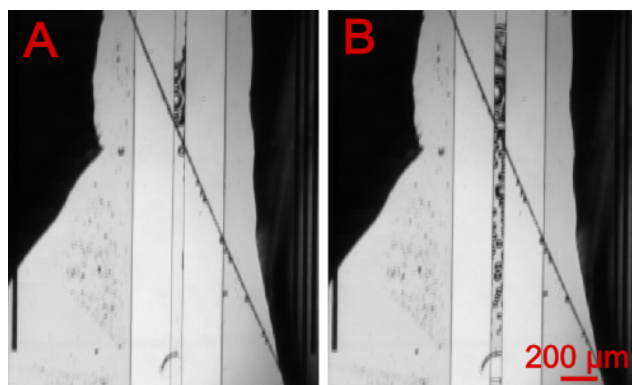Sigma Aldrich 1.0 µm dragon green and 0.2 µm suncoast yellow fluorescence

Figure 7.9: **Bubbles Generated From SAWs**
The images show that bubbles generate in the channel. For this specific experiment, a signal of -16 dBm was generated at the signal generator when the bubbles appeared. Image (**A**) is taken within a second of image (**B**). In addition, the signal made a crack in the LiNbO$_3$, seen as the diagonal line which crosses the channel. For this device the IDT$_A$ device was used. The center particle flow is 40 µL/h while the sheath flow is 60 µL/h.

polystyrene particles were used to trace fluorescence particle streams in the microfluidic channel. However, for our experiment, no significant separation of the particles was achieved when using the IDT$_A$ design. During the experiments, cracks appeared in the LiNbO$_3$ when the output signal from the signal generator exceeded -14 dBm. For some devices bubbles appeared in the channel between the IDT pairs when the generated signal exceeded -16 dBm. The appearance of these bubbles are shown in Figure 7.9. The cracks may result from the combination of a weak LiNbO$_3$ and a high amplitude SAW. No further experiments were performed using the IDT$_A$ design and fluorescence particles.

7.3.2 Acoustophoresis Using IDT$_B$

The frequency response data suggests the IDT$_B$ design as the better choice of device for further testing. From the results in Figure 7.8 one can see that the color highlighted 3.0 µm polystyrene particles have different velocities when separated. The 3.0 µm particles were successfully filtrated from the 0.5 µm particles, however, they do not all follow one distinct streamline. Also, the sorted particles do not have the same velocity, indicating that they are positioned in different vertical and lateral positions in the channel. If the particles were centered both laterally and vertically, prior to arriving at SSAW field, the rate of separation could increase because

the particles are located at the spot of maximum pressure. When the particles are not centered laterally or vertically when arriving at the SSAW field, unequal forces will act on the different particles, and the acoustophoretic sorting might not be optimal. To investigate this further, the double IDT_B device is tested, where a IDT_B design for focusing particles and a IDT_B design for particle separation are located on one single device (see Figure 5.4).

The 5.2 mm long focusing IDTs are designed so that SAWs from one of the IDTs are phase shifted by 180°. This is obtained by opposite wirebonding of the IDTs: Instead of symmetrical wirebonding for both IDTs, the signal and ground signal is switched for one of the IDTs. This switches the polarity of the signal in the periodical electrode fingers, causing a 180° phase shift in the generated SAW. To further understand the theory and the behavior of phase shifted SSAWs and the corresponding pressure nodes, opposite wirebonding of the focusing IDT_B design is investigated. Figure 7.10 show how a -16 dBm signal affects 3.0 μm polystyrene particles. The resonance frequency for the device was found using Frequency Finder, and measured to 38.8 MHz. The channel is 60 μm wide, so with a 180° phase shift one should be able to observe the displacement of the nodes and anti-nodes. With symmetrical wirebonding the two IDTs of the IDT_B design are 180° out of phase, and the particles are centered in the channel (Figure 7.10 **B**). Afterwards, one of the IDTs are opposite wirebonded, resulting in an additional 180° phase shift. With the IDTs now in phase, the pressure node is displaced to the center of the channel. Hence, the particles are separated towards the channel walls (Figure 7.10 **C**). These results show how the pressure nodes and anti-nodes change lateral position when the IDTs are 180° out of phase.

Figure 7.12 show how the focusing and separation IDTs affect the 3.0 μm particles. After the experiment the alignment of the IDTs, relevant to the PDMS channel, was measured using a microscope (Figure 7.13). These measurements, and corresponding alignment offset, are listed for each IDT in Table 7.4.

Comparing Figure 7.12 to the alignment measurements in Table 7.4, one cannot see a significant impact from the alignment offset. The offset is close to 100 μm for all measurements, hence it will not have a significant effect on the pressure node location since the SSAW is spatially periodical for each 100 μm. The biggest offset is at the end of the 3.2 mm separating IDTs, where the pressure nodes should be located 21 μm to the left of the walls. An influence of this alignment offset is not observed when looking at Figure 7.12 **C**, where the impact of the SSAW field on
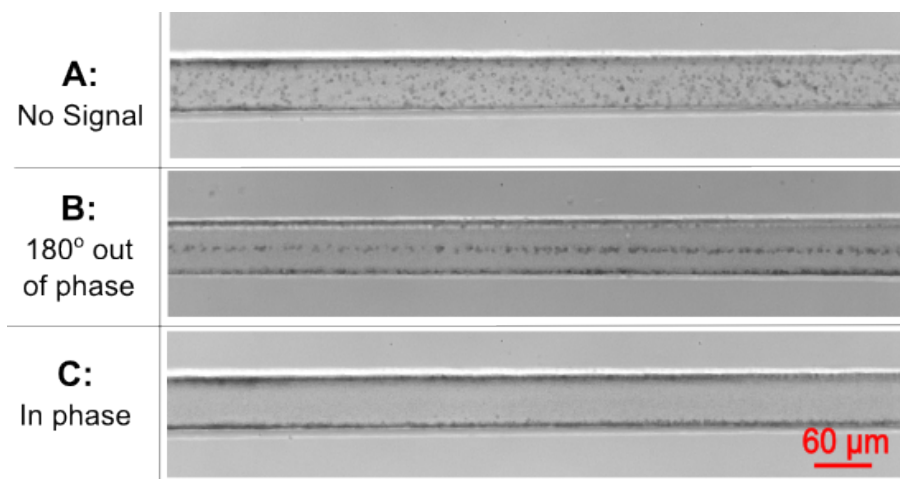
Figure 7.10: **IDT$_B$: Phase Shift and Node Locations**
A: When the signal is off, the 0.5 µm polystyrene particles are randomly distributed in the 60 µm wide channel. **B:** The IDTs are designed to be 180° out of phase, so that a pressure node should appear in the channel center. When the signal is turned on, the particles relocate to the center pressure node. **C:** The same device, and channel location, when the IDTs are opposite wirebonded. The IDTs are now in phase, result in an anti-node in the center of the channel. The signal is generated with a frequency and amplitude of 38.8 MHz and -16 dBm. The flow rate is set to zero, but the particles are still moving towards the outlet, located towards the right side of the images.

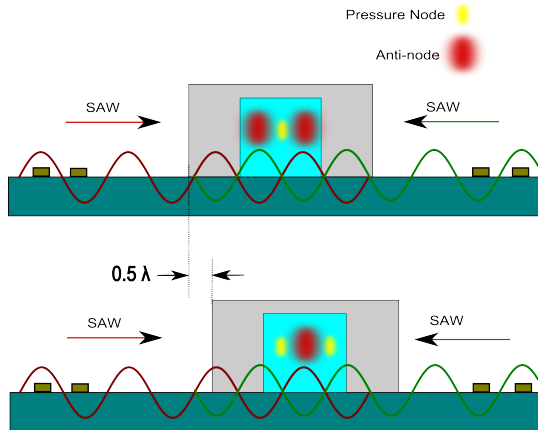Figure 7.11: **Illustration Alignment Offset**
The figure illustrates how misalignment of the microfluidic channel relevant to the IDTs affects the position of the pressure nodes. When an offset of $\lambda/2$ an pressure anti-node appears in the center of the channel instead of a pressure node. Hence, the particles will not be focused at the center, but forced outwards to the pressure nodes. This means that for a SSAW with a wavelength of 50 μm an offset of 24 μm will completely change the function of the device.

particles in this region is shown.

Further, experiments to sort 3.0 μm from 0.5 μm particles were executed with the double IDT$_B$ design shown in Figure 7.14) where particles are traced over time. When the field is off one can observe that the particles move with different velocities. There are particles in the background, out of focus, indicating that the particles are located in different vertical positions in the channel. When the SSAW fields are turned on, the 3.0 μm particles are filtered out through the right inlet, while the 0.5 μm particles continues through the centered outlet. Comparing this result with the results of the single IDT$_A$ device (Figure 7.8), one can see that the particles are more centered vertically, and have an equal velocity when sorted. For this experiment 1 drop of 3.0 μm particle solution and 1 drop of 0.5 μm particle solution were diluted in 1000 μL of MQ water. The same influence on the particles is observed in Figure 7.15, where a higher concentration of particles are sorted. The concentration was increased to 3 drops of 3.0 μm particle solution and 3 drops of 0.5 μm particle solution, diluted in 1000 μL of MQ water. The signal affecting the particles, shown in Figure 7.14 and Figure 7.15, has an amplitude of -18 dBm and -22 dBm, respectively, while both have a frequency of 38.8 MHz. For these exper-
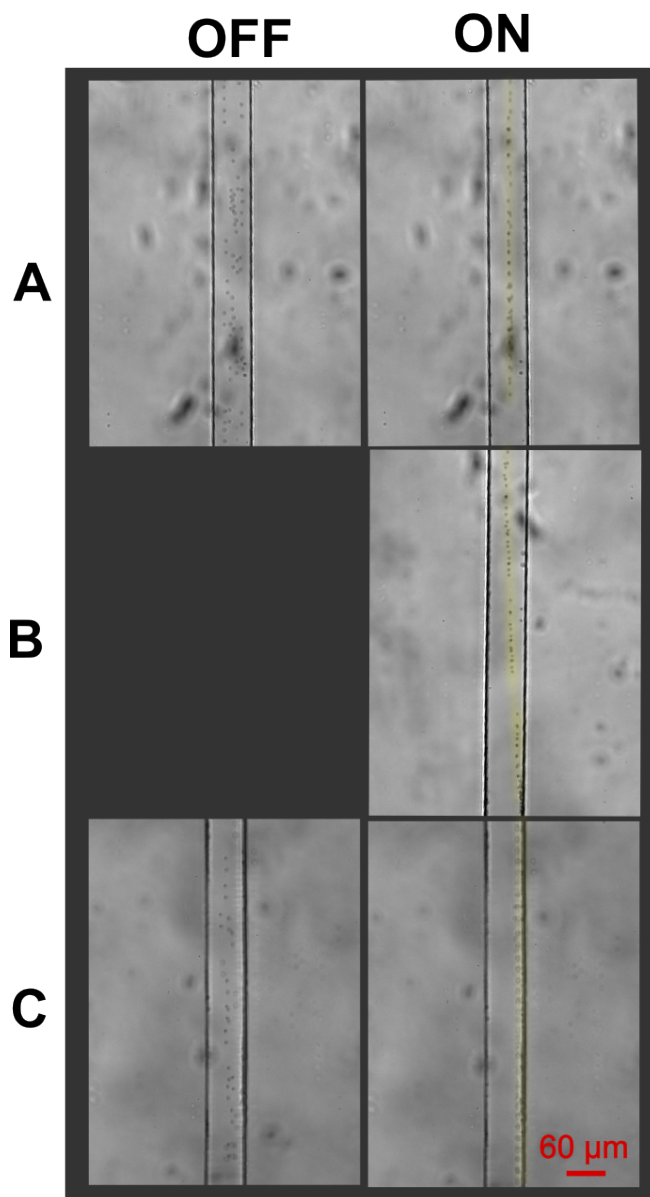
Figure 7.12: **IDT$_B$: Impact on 3.0 µm Particles**
The impact on 3.0 µm particles using a double IDT$_B$ design, where microscope images of the particles in a 60 µm wide channel are taken at three locations in the channel: At the end of the 5.2 mm focusing IDT (**A**), at the start of the 3.2 mm separating IDT (**B**) and at the end of the 3.2 mm separating IDT (**C**). For the images where the SSAW field is turned on, the particle bands are slightly highlighted in yellow. A -16 dBm signal with a frequency of 39.8 MHz is generated at the signal generator, and the flow rate is set to 50 µL/h for center and sheath flow.

Figure 7.13: **Double IDT$_B$ Device: Alignment**
Alignment measurements for the double IDT$_B$ device, with an effect shown in Figure 7.12, were measured using a ZEISS microscope and Carl Zeiss AxioVision Rel. 4.7 software. Several distances between the closest electrode on a IDT to the nearest PDMS feature, are measured for each IDT. The inlet is located to the left of the 5.2 mm focusing IDT, while the outlet is located to the right of the 3.2 mm separating IDT.
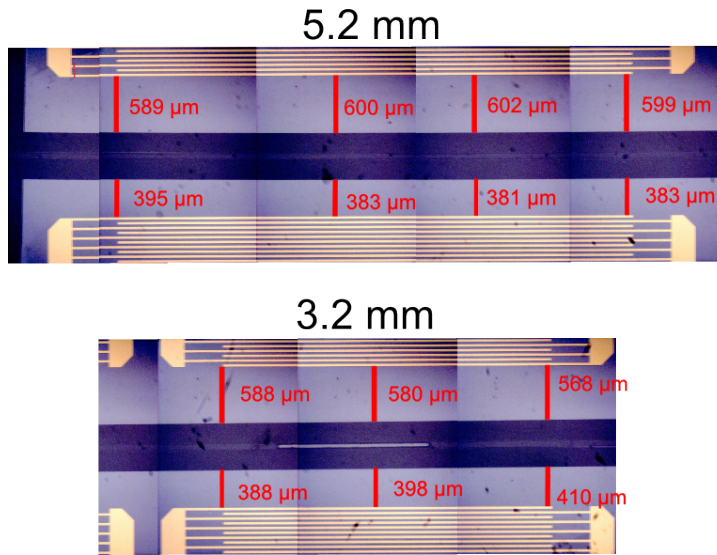
Table 7.4: The alignment measurements for the double IDT$_B$ device, shown in Figure 7.13 are presented. The alignment and pressure node offsets are calculated for all measurements. A negative or positive value for the pressure node offset implies that the pressure node is located to the left or to the right of the optimal site of the pressure node, respectively. The optimal site is the channel center for the focusing 5.2 mm IDT, and at the channel walls for the separating 3.2 mm IDT.

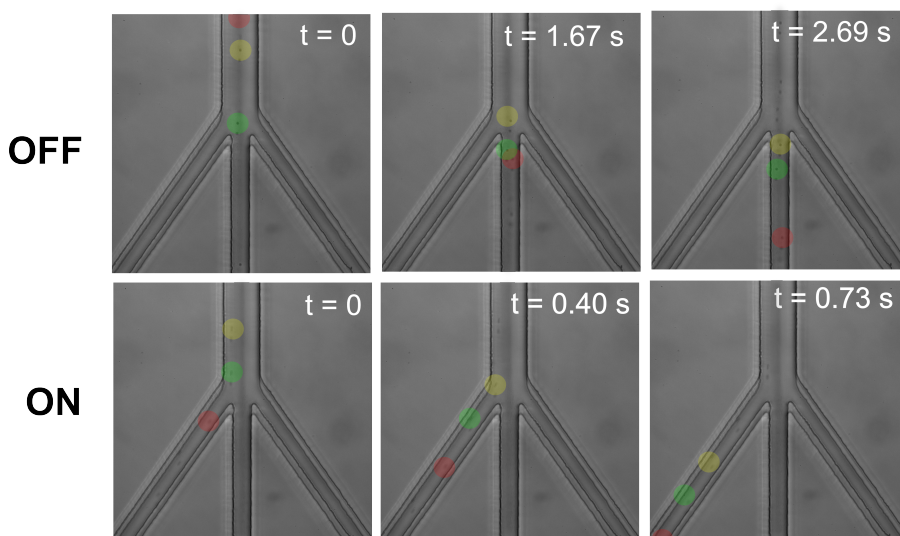| IDT pair	Left Side	Right Side	Alignment offset	Pressure node offset
5.2 mm	395 μm	589 μm	97 μm	-3 μm
5.2 mm	383 μm	600 μm	109 μm	9 μm
5.2 mm	381 μm	602 μm	111 μm	11 μm
5.2 mm	383 μm	599 μm	108 μm	8 μm
3.2 mm	388 μm	588 μm	100 μm	0 μm
3.2 mm	398 μm	580 μm	91 μm	-9 μm
3.2 mm	410 μm	568 μm	79 μm	-21 μm

Figure 7.14: **Double IDT$_B$ Device: Particle Tracing**
The colored dots trace 3.0 μm particles though a time series. **OFF:** The highlighted particle traces show the movement of particles when the field is off. The trace show that the particles have different velocities. **ON:** The particles move at the same velocity, which is observed in the constant distant in between the particles over time. The 0.5 μm particles does not seem affected by the SSAW field, following a straight line out through the center outlet both when the fiels is on and off. The effect from the signal generator is -19 dBm, and the signal's frequency is set to 38.8 MHz. The flow rates are 60 μL/h, 10 μL/h and 70 μL/h for respectively left sheath flow, center particle flow and right sheath flow.

iments a 60 μm wide PDMS channel design with three inlets, one for each sheath flow and one for the center flow, is used. For both experiments the flow rates were set to 60 μL/h, 10 μL/h and 70 μL/h for respectively left sheath flow, center particle flow and right sheath flow. At these flow rates, all particles exited through the center outlet when the fields are off as shown in the figures.

Investigating separation of smaller particles, experiments were performed to characterize how the double IDT$_B$ design affects 1.0 μm and 0.2 μm fluorescence particles. For this experiment 20 μL of 1.0 μm particles and 20 μL of 0.2 μm particles were diluted in 1000 μL of MQ water. Figure 7.16 present the results using a 120 μm wide channel and a -22 dBm signal. The resonance frequency was obtained using Frequency Finder on the 5.2 mm wide focusing IDT, measured to 38.8 MHz. The sheath flow and center particle flow is set to 60 μm and 20 μm, respectively. At the
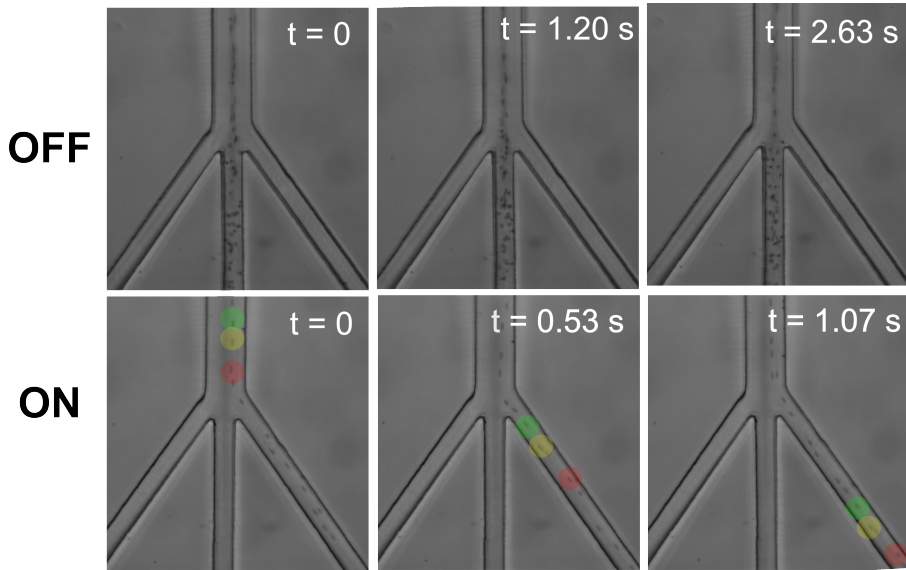
Figure 7.15: **Double IDT$_B$ Device: Particle Tracing of Higher Concentration**
The colored dots trace 3.0 μm particles though a time series. **OFF:** he highlighted particle traces show the movement of particles when the field is off. The traces show how the particles have different velocities. **ON:** The particles move at the same velocity, which is observed in the constant distant between the particles over time. The generated signal has an amplitude of -22 dBm, and the signal frequency is set to 38.8 MHz. The flow rates are 60 μL/h, 10 μL/h and 70 μL/h for respectively left sheath flow, center particle flow and right sheath flow.

end of the focusing IDT (Figure 7.16 **A**) it seems like three nodes have appeared, one at the channel center and two 25 μm on each side of the center. The 100 μm pitch IDTs should produce pressure nodes at a distance of 50 μm apart, hence the centered particle band can not be a result from a pressure node. One explanation for this phenomena might be a result of too high concentration of particles or/and too high flow rate, in addition to an alignment offset. If we assume that the alignment is off to either side by 25 μm, an anti-node should appear at the channel center and pressure nodes 25 μm to either side, as observed. If the flow rate is too high as well as the particle concentration only some particles may be affected enough by the pressure anti-nodes to move towards the pressure nodes. If this is the case, the centered particle band is a result of unaffected particles with a high velocity. Looking at the particle influence of the separation IDT$_B$ (Figure 7.16 **B**) one can observe how the particles are affected alike; some particle have aggregated into particle bands where pressure nodes should not appear.

However, no alignment measurements were taken for this device prior to these measurements. And, even though a 25 μm alignment offset might help explain the additional particle bands, no experimental data can support this statement.

When the SSAW field is off, the 0.2 μm particles seem to have diffused laterally in the channel to a larger degree than the 1.0 μm particles (Figure 7.16 **B**). When the field is turned on, the 0.2 μm particles are clearly affected by the pressure field in some way, but are not following distinct pressure bands compared to the larger particles. This show that the particles are affected differently, due to their difference in size.

Shortly after these images were taken a local debonding of the PDMS and LiNbO$_3$ appeared, and no further experiments were conducted for this specific device. These images show that 1.0 μm particles and 0.2 μm are affected differently. However, some difficulties are presented.

To further analyze how 1.0 μm and 0.2 μm particles are affected, a double IDT$_B$ device with a 60 μm wide PDMS channel was tested. The results are shown in Figure 7.17. The flow rate for the sheath flow and center particle flow is 40 μm and 20 μm, respectively. The generated signal has an amplitude of -16 dBm and a frequency of 38.8 MHz. 20 μL of 1.0 μm particles and 20 μL of 0.2 μm particles were diluted in 1000 μL of MQ water. Two microscopy images were taken of the device to characterize the alignment accuracy, shown in Figure 7.18.

When the SSAW field is on, one can observe from Figure 7.17 that the 1.0 μm
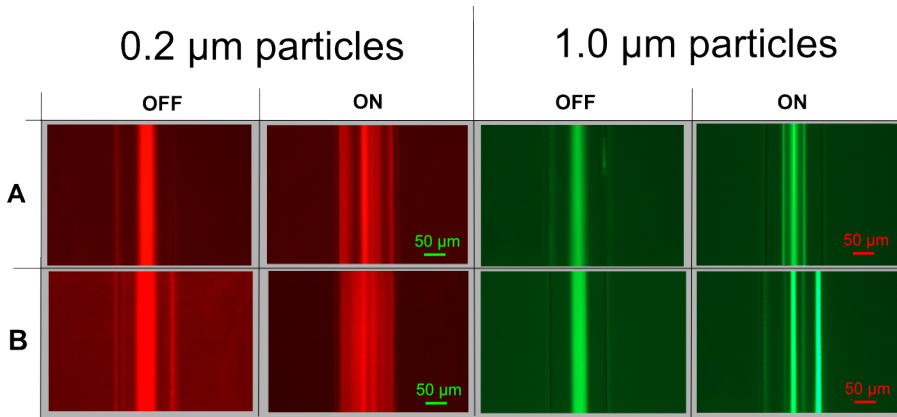
Figure 7.16: **Double IDT$_B$ Device: Particle Manipulation**
120 μm Wide Channel. How 0.2 μm (red) and 1.0 μm (green) particles are affected
at different sections of a 120 μm wide channel:**A** shows the region at the end of the
focusing IDTs, while **B** shows the region at the end of the separation IDTs. The
SSAW is generated from 100 μm pitch IDT$_B$ design, with a generated -22 dBm,
38.8 MHz signal. The flow rate for the centered particle flow and the sheath flow is
20 μL/h and 60 μL/h, respectively.

particles are concentrated in specific particle bands, while the 0.2 μm particles are
spread more laterally within the channel. However, it looks like the concentrated
line of particles only exits though the center outlet. The difference in light intensity
from the particles might be due to a lower concentration of particles entering the
channel when the images waere taken. In addition an external light source, or a
spill of fluorescence particles on the outside of the channel, may add light pollu-
tion to the images, reducing the light intensity and contrast in the images. Hence,
light intensity should not be used as a quantitative measurement for lateral diffu-
sion before eliminating all external light sources.

At the focusing IDT$_B$ (Figure 7.17 **A**) one can see that the 1.0 μm particles are fo-
cused at the center of the channel and approximately 20 μm to the left of the center.
The center line is less concentrated than the left line, and might be a result of high
flow rate and initial particle concentration. At the separation IDTs (Figure 7.17 **B**)
it looks like an anti-node is located at the channel center with two particle bands,
i.e. pressure nodes, on either side. The right particle band is located a bit closer to
the center line than the left band. There is also a particle band located at the left
channel wall. At the outlet (Figure 7.17 **C**) one can clearly see that the particles are
split into several particle aggregation bands. There are two main particle bands,
one that exits through the left outlet and one that partly exits through the center
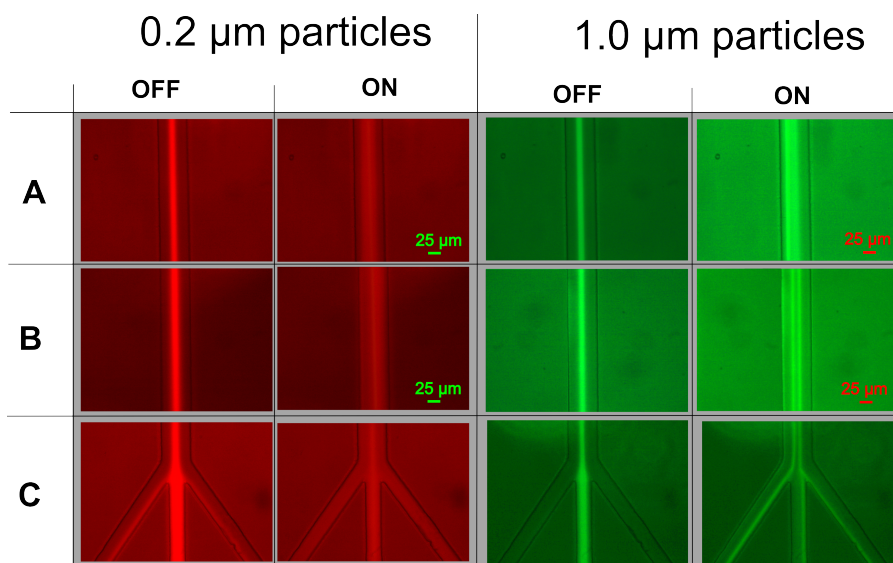
Figure 7.17: **Double IDT$_B$ Device: Particle Manipulation in a 60 μm Wide Channel.** The impact of SSAWs, generated from 100 μm pitch IDT$_B$ design, with a generated -16 dBm 39.8 MHz signal. The microfludic channel is 60 μm wide, and the flow rate for the sheath flow and center particle flow is 40 μm and 20 μm, respectively. The images show how 0.2 μm (red) and 1.0 μm (green) particles are affected at different sections of the channel: **A** show the region at the end of the focusing IDTs, **B** show the region at the end of the separation IDTs, while **C** shows the outlet junction of the channel. Some images were initially very dark, compared to others, and a fluorescence filter in Inkscape was used to adjust the overall brightness for some of these images.
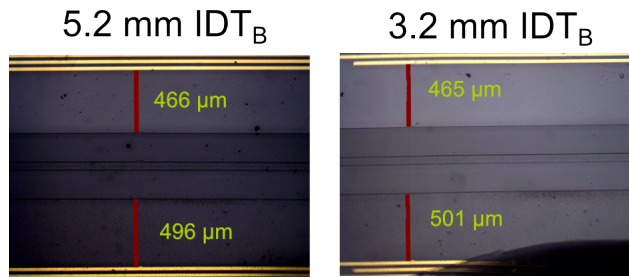
Figure 7.18: **Double IDT$_B$ device: Alignment Accuracy**
The alignment accuracy is measured using Carl Zeiss AxioVision Rel. 4.7. The length from the IDTs to the PDMS feature next to the channel is measured and compared for both IDTs. The inlets are located to the left of the images, while the outlets are located to the right. Measurements are shown for both the 3.2 mm long and the 5.2 mm long IDTBs. The measurements for the 5.2 mm IDTs are close to the end farthest from the inlet, while the measurements for the 3.2 mm IDTs are at the end of the IDT, farthest away from the outlet. The 5.2 mm IDT is shifted approximately 15 µm to the right, hence the pressure nodes should be shifted 15 µm to the left. The 3.2 µm IDT is shifted approximately 18 µm to the right, giving the pressure nodes are shifted 18 µm to the left. The particle impact for this device is shown in figure 7.17.

outlet and partly through the right outlet.

Compared to the 1.0 µm particles, the 0.2 µm particles does not seem to be affected by the SSAW field, since a concentrated line of particles are centered laterally throughout the length of the microfluidic channel.

The measurements in Figure 7.18 show that the alignment between the focusing IDTs and the PDMS channel is off by approximately 15 µm to the right. This might explain the reason why the particle band is off to the left by that same distance from the center of the channel.

For the focusing IDTs, the alignment is off to the right by approximately 20 µm. This means that the pressure nodes should be located approximately 20 µm to the left, closer to the channel center than to the wall. However, the alignment measurements were obtained at the start position of the separating IDTs, while the images in Figure 7.17 **B** are obtained from the end location of the separating IDTs where the alignment measurements may be different. A change in alignment of 5µm–10 µm over the length of the IDTs is plausible when looking at the alignment measurements for a similar device in table 7.4. Either way, the alignment offset does not explain the particle segregation that is observed at the channel center. Another reason may be that the pressure field, generated from the SSAW field, does

not affect all the particles in the channel. A limitation in separation effect when the particle concentration is too high have been discussed earlier. This could explain why there are two particle bands at the outlet; one is due to a pressure node while the other is a high concentration of particles that are not affected by the radiation forces.

Comparing these results with the results in Figure 7.16, the most important observation is how the 0.2 μm particles are differently affected by the SSAW then the 1.0 μm particles. Even though the amplitude is increased from -22 dBm to -16dBm, the 0.2 μm particles does not move much in the lateral direction in Figure 7.17, compared to the results in Figure 7.16. An increased flow rate for the center particle flow is used for the latter experiment, compared to the earlier experiment, which might reduce the time that the particles are acted upon by the radiation force.

7.3.3 Acoustophoresis Using IDT$_D$

From Equation 3.3 (see Section 3.2) one can see that the radiation attenuation constant is proportional to the frequency. This means that more energy is released from the leaky waves, and converted into compression waves, for a device generating SAWs with a higher frequency. Hence, the radiation force will increase when the frequency increases, and the wavelength decreases (see Equation 3.4).

To investigate and characterize how a SSAW, generated from the 50 μm pitch IDT$_D$ design, affect particle separation, 3.0 μm polystyrene particles were inserted in a 60 μm wide channel in between a IDT$_D$ pair. This IDT pair is designed to focus particles, and the two IDTs generate SAWs which are 180° out of phase. The results are displayed in Figure 7.19, and the microscope images are taken towards the end of the IDT, with the outlet orientated towards the bottom of the image. The flow rate is turned off, so that the particles are slowly drifting in the channel, making it is easy to characterize the generated pressure nodes.

The figure show how the SSAW generated pressure nodes, and anti-nodes, are located 25 μm apart. There is an anti-node located slightly to the left of the center, pushing the particles to the pressure nodes on either side. The anti-node seems to alter slightly towards the left as the particles move closer towards the outlet. Figure 7.20 show measurements for the alignment accuracy of this device, where the location of interest of Figure 7.19 is highlighted in orange. The measurements from the figure are listed in Table 7.5. From these values, on can see that the alignment at the center of the figure is off towards the right IDT by approximately 35 μm. With a distance of 25 μm between the nodes, this means that the centered node is off by

Table 7.5: The Alignment measurements for the IDT$_D$ device with an particle impact characterized in Figure 7.19 are presented. The alignment and pressure node offset is calculated for all measurements. A negative or positive value for the anti-node offset implies that the pressure node should be located to the left or to the right of the channel center, respectively.

Location	Left Side	Right Side	Alignment offset	pressure node offset
A	518 μm	472 μm	23 μm	-2 μm
B	526 μm	468 μm	29 μm	+4 μm
C	532 μm	454 μm	39 μm	-11 μm

10 μm to the left. The alignment offset slightly moves towards the right IDT from point **A** to **C**. This fits with the observations from the microscope images of the nodes in Figure 7.19.

To study how an additional 180° phase shift affects the system, one of the IDTs were opposite wirebonded, and 3.0 μm and 0.5 μm particles were inserted intro channel. The result is shown in figure 7.21, where one can see the that the nodes and anti-nodes are displaced 12.5 μm to the side. The flow rate was stopped right before the field was set on, so that the particles are moving slowly towards the outlet. At this low flow rate the 0.5 μm particles are also centered in the particle bands when the SSAW field is turned on. These result show how the 50 μm pitch IDT$_D$ device generates twice as many pressure nodes as the 100 μm pitch IDT over the same channel width. It is also shown how opposite wirebonding can be used as a tool to switch the placement of pressure nodes and anti-nodes for a device. It also presents that with a low flow rate the 0.2 μm particles align in aggregated particle bands. Hence, flow rate is also a parameter that affects the filtration.

For the double 100 μm pitch IDT$_B$ device, all of the fluorescence particles were not forced towards the pressure nodes (Figure 7.16 and Figure 7.17), but some went unaffected straight through the microfluidic channel. To characterize the impact of the IDT$_D$ on smaller particles, an experiment was conducted to study how a double IDT$_D$ device, with twice the frequency, have on 1.0 and 0.2 μm fluorescence polystyrene particles. 20 μL of 1.0 μm particles and 20 μL of 0.2 μm particles were diluted in 1000 μL of MQ water were used for this experiment. Figure 7.22 shows the results, where a 120 μm wide channel was used to observe several nodes and anti-nodes at the same time. The signal was set to -18 dBm, before amplified,
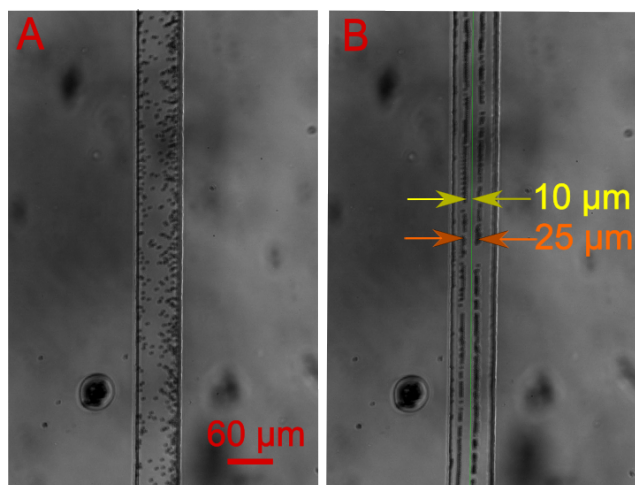
Figure 7.19: **IDT$_D$: Impact on 3.0 µm Particles**
3.0 µm particles are injected into a 60 µm channel and the flow is turned off. **A:**
Particles are moving slowly towards the outlet when the SSAW field is turned off.
B: A -16 dBm signal with a frequency of 77.0 MHz is generated in the signal gener-
ator. The SSAW field generates two discrete pressure nodes with particle bands, in
addition to the particles at the channel walls. The bands, and hence the pressure
nodes, are located 25 µm apart. A pressure node is present, 10 µm to the left of the
center. The center of the channel is marked in green, and the yellow and orange
arrows marks 10 µm and 25 µm, respectively.
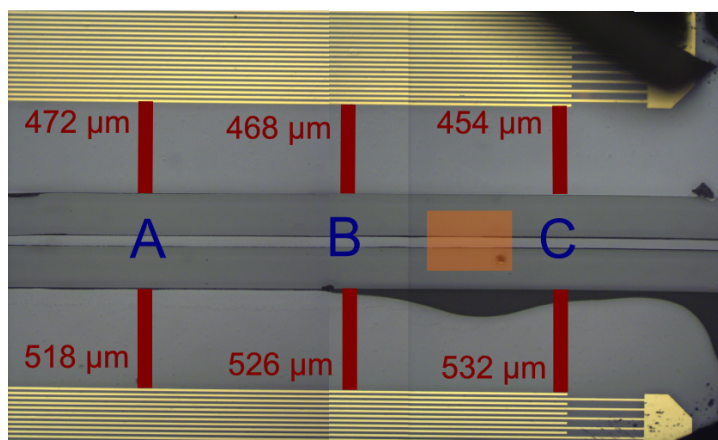
Figure 7.20: **IDT$_D$: Alignment**
The alignment accuracy is found by measuring the length from the IDTs to the
PDMS feature next to the channel, using a ZEISS microscope and Carl Zeiss Axio-
Vision Rel. 4.7 software. The highlighted area show where the microscope images
in Figure 7.19 are located. For references, the inlet is located prior to the location
of point **A** and the outlet is located after point **C**.

and the frequency set to 78.8 MHz. When the field is off, both particle types are
centered in the lateral direction of the channel, and the flow rate is adjusted so
that the particles exits through the center outlet. To achieve this, the center parti-
cle and sheath flow was set to respectively 20 µL/h and 50 µL/h. When the field is
turned on, the 1.0 µm particles appear in distinct particle bands. At the focusing
IDT (Figure 7.22 **B**), the most concentrated particle band is located at the channel
center. This implies the presence of a pressure node, centering the particles. In ad-
dition, a second node is located approximately 20 µm – 25 µm to the right. Between
the same IDTs, the 0.2 µm particles are divided into several particle bands. These
bands are not as concentrated as the 1.0 µm particles, implying that the acous-
tic radiation force have a greater impact on the larger particles. Also, the particle
patterns coincides with what is predicted for the focusing IDT$_B$ device, producing
SAWs with a wavelength of 50 µm. If one pressure node is located at the center of
the channel, the next node should appear 25 µm on both sides of the center, which
coincides with the results if we assume that the alignment is off slightly to the right.

Figure 7.22 **C** shows images of the channel, taken at the end of the separation
IDTs. A pressure node has appeared at the right channel wall, observed clearly for
the 1.0 µm particles. However, the particle band in the center of the channel is still
present. In addition, two less concentrated bands have appeared 20 µm – 25 µm
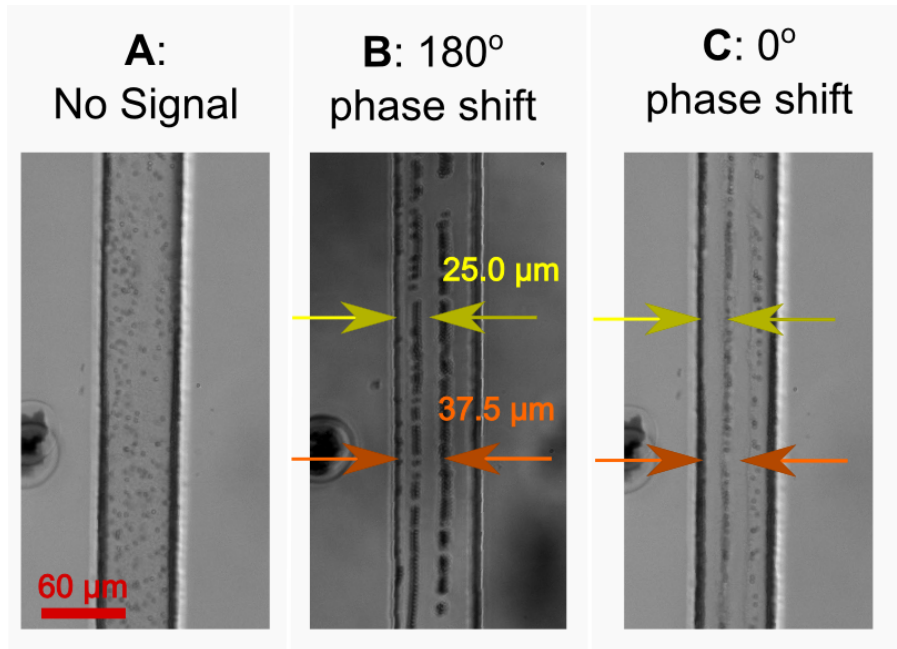
Figure 7.21: **IDT$_D$: Impact of Phase Shift On Nodes**
A: A 60 μm wide channel with 3.0 and 0.5 μm particles when the signal is off. **B:** The impact on the nodes and anti-nodes when the two generated SAWs are out of phase by 180° . The yellow and orange arrows marks 25.0 μm and 37.5 μm, respectively. **C:** The impact of the same device, and channel location, when the IDTs are opposite wirebonded. The IDTs are now in phase, result in a displacement of the nodes and anti-nodes by 12.5 μm. The signal is generated with a frequency and amplitude of 77 MHz and -18 dBm. The flow rate is set to zero, but the particles are still moving slightly towards the outlet (bottom of images).

on each side of the channel center. The 0.2 μm particles have also aggregated into visible bands, but the particle bands are not as distinct as for the larger particles. The separating IDTs produce SAWs with a wavelength of 50 μm, where a anti-node should be located at the center of the channel. Moreover, a pressure nodes should be present at a distance of 12.5 μm on each side of the center. It seems like the separation IDTs have a similar impact on the particles as the focusing IDTs, but the SSAW should have a phase shift so that an anti-node appears at the channel center.

Microscope images of the device were used to measure the distance from the IDTs to the microfluidic channel, shown in Figure 7.23. Comparing the results in Figure 7.22 to the 6th and 10th alignment measurement, one can see the following: Measurement **6** result in a pressure node offset 4 μm to the left of the center line. This corresponds with the change in location of the pressure node in Figure 7.22 **B**. Measurement **10** results in an anti-node, 2 μm to the left of the center line, which also supports the data.

Even though the alignment measurements fits the observed results, it should be noted that there might occur errors in the alignment measurements in Figure 7.23. The images were taken using a ZEISS microscope with a 5X objective. They were, for these measurements, imported into Inkscape. A pixel-to-μm ratio was found for each image, comparing the length of several IDT pitches in pixels to the length of the pitches in μm. The pixel alignment lengths, between the IDTs and the channel features, were converted to μm and the alignment measurements were compared to each other. This way the alignment and pressure node offset could be calculated, resulting in Figure 7.23 **D**. Even though the alignment measurements fit to the data, this method of measuring can produce micrometer scale errors, errors that are crucial for the scale of these devices.

There are several advantages with generating SAWs with higher frequencies. The most important one is that the SAWs that are generated have shorter wavelengths. With half the wavelength one can double the acoustic radiation force on the particles, as seen in Equation 3.4. In addition, SAWs with a higher frequency will generate more nodes and anti-nodes in a channel. By doubling the frequency, one can reduce the channel width by a factor of two. This can lead to smaller devices, or more fine tuned separation.

However, there is a trade-off by going to higher frequencies. When the wavelength decreases, the alignment of the channel and the IDTs become more crucial. An alignment offset by 12.5 μm changes the output of the device severely. From
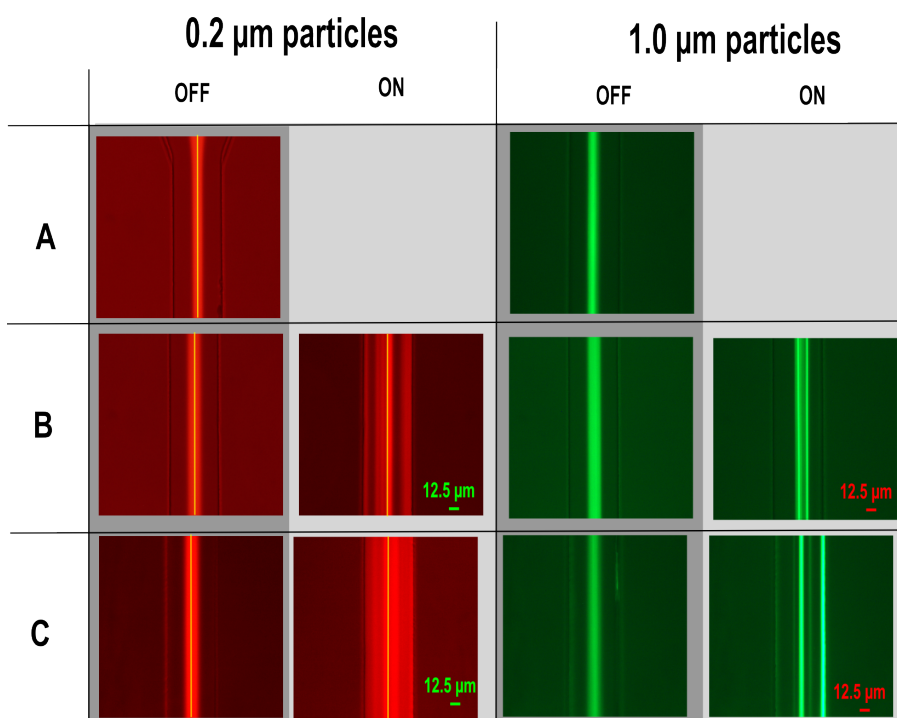
Figure 7.22: **Double IDT$_D$ Device: Particle Manipulation**
The impact of SSAWs on 0.2 μm (red) and 1.0 μm (green) particles, generated by double IDT$_D$ device. The microfludic channel is 120 μm wide, and the center is marked with a yellow or red line. The signal is set to -20 dBm, with a 78.8 MHz frequency. The center particle and sheath flow is 20 μL/h and 50 μL/h, respectively. **A** show the particles right after the inlet, focused only by sheath flow. **B** show how the particles are affected by the 5.2 mm IDT for focusing, while **C** show how they are affected by 3.2 mm IDT for separation.
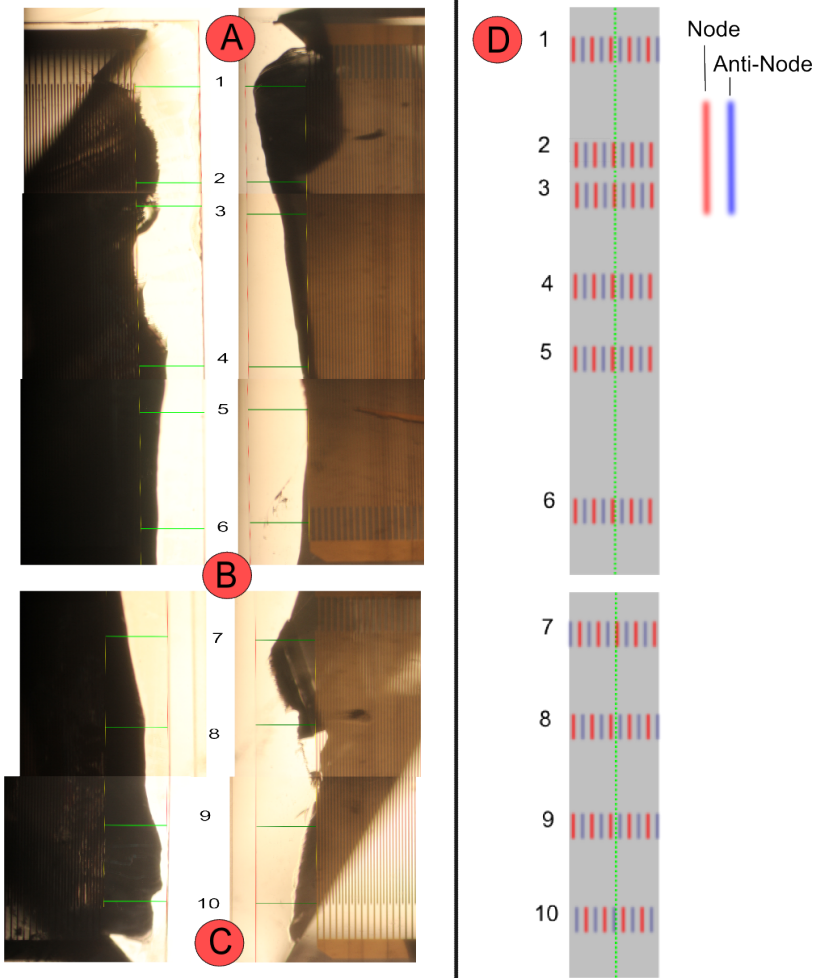
Figure 7.23: **IDT$_D$: Particle Alignment 120 μm Wide Channel**
The left hand side shows microscope images of the IDT$_D$ device. The marks **A**, **B** and **C** refers to the sight where the images of fluorescence particles are taken (shown in more detail in figure 7.22). The measurements are found by measuring the length between the IDTs and the PDMS channel, shown in green lines. Comparing these to the pitch length of the IDTs, the offset in alignment is calculated. **D:** A schematic of the resulting offset in pressure nodes (red bars) and anti-nodes (blue bars), relative to the 120 μm wide channel (gray area) and the channel center (dotted green line). With a 50 μm SSAW, there fit almost 10 nodes and anti-nodes fit inside the width of the channel, resulting in nodes and anti-nodes periodically for every 12.5 μm.

the results one can see how the alignment can vary over the length of the channel. Several 50 µm devices were made during this work, however, the difficulties with alignment resulted in no devices where the nodes and anti-nodes were perfectly aligned.

These results show that the 50 µm pitch IDTs affect the particles as predicted, however, the alignment accuracy has to increase and become more reproducible, before this design can be used for reproducible and precise particle separation.

7.3.4 Acoustophoresis Using FIDTs

A FIDT$_A$ device was tested on 1.0 µm and 0.2 µm particles, shown in Figure 7.24. Compared to the straight 100 µm pitch IDTs, the pressure field should have a greater pressure amplitude at the focal point. The particles were clearly affected by the generated SSAW, and different values of flow rate and signal amplitude were tested to find optimal parameters for particle sorting.

For the FIDT$_A$ design, one can see from Figure 7.24 that finding an optimal flow rate and signal amplitude is crucial for separating the 1.0 µm particles from the 0.2 µm particles. Both particles are affected for all the experiments, although judging from the fluorescence concentration, the 1.0 µm particles are more affected compared to the 0.2 µm particles. No combination of parameters for flow rate and signal amplitude completely separated the bigger particles out to the sides of the channel while leaving the small particles centered. No further experiments were conducted on the FIDT designs due to a main emphasis on the uniform straight IDT, and how the double IDT design affects particles.

While the FIDT$_B$ design was successfully fabricated and tested with the network analyzer, no complementary experiments were performed with the device in time for this work.

Flowrate centerflow

Flowrate sheatflow

Signal Amplitude

Signal ON/OFF

0.2 μm particles

1.0 μm particles

10 μL/h

-20 dBm | OFF | ON

-18 dBm | OFF | ON

50 μL/h | 20 μL/h | 10 μL/h

-16 dBm | OFF | ON | OFF | ON | OFF | ON
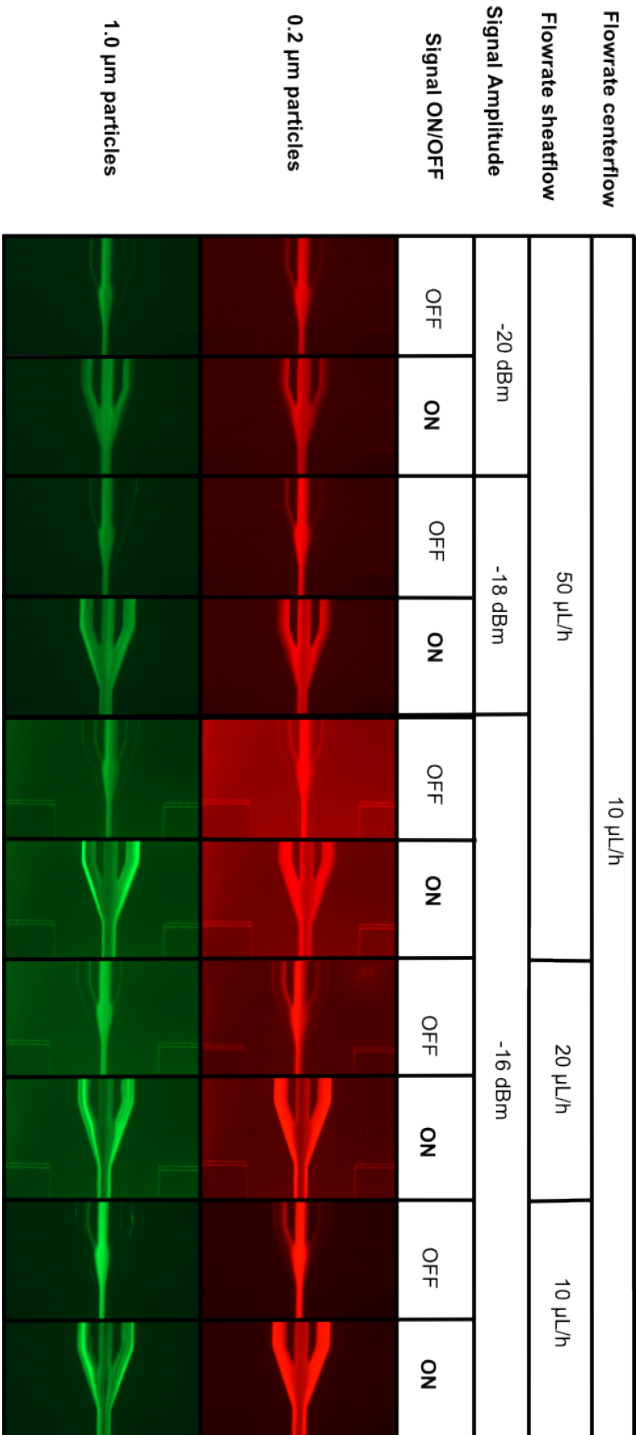
Figure 7.24: FIDT$_A$: Impact on 1.0 μm and 0.2 μm Particles: The microscope images show how to signal amplitudes and flowrates affects the separation of 1.0 μm particles (green fluorescence) and 0.2 μm particles (red fluorescence), at the outlets of the 60 μm wide channel. The amplitude signal recorded is the signal from the signal generator, before it is amplified. The center flow, containing the particles is set to a constant 10 μL/h. The sheath flows, centering the particles in the center flow, is varied.

7.4   Potential as POC Device

The size of the device, and the components needed for the experimental setup, are promising when considering the potential for developing a on-chip filtration device for POC purposes. As of now, all experimental setup needed to run these devices could be implemented in any home or small medical clinic. In addition, Frequency Finder shows how one can make a simple and inexpensive frequency response measurement device with simple laboratory equipment and a computer. The challenge in creating submicron particle separation devices lies in the fabrication techniques, especially in relation to accurate alignment of the IDTs and the microfluidic channel. A successfully reproducible industrial acoustophoretic device could be fabricated by using more rigid material and more advanced industrial microfabrication techniques. If the device was created from one single mold, instead of several processes creating several components, the alignment error would disappear.

8 | Conclusion and Further Work

This thesis investigates how SAWs can be used as a mean of acoustophoretic sorting of micron and submicron particles. A theoretical framework for SAWs, IDTs and microfluidics is presented, and further used to design acoustophoretic devices for sorting particles according to their size. (i) Microfabrication techniques were used to fabricate PDMS microfluidic channels and IDTs with different design, assembled to acoustophoretic particle separation devices. Furthermore, the different IDT designs were investigated and compared by (ii) determining the resonance frequency for the different designs by means of frequency response measurements. (iii) Further experiments were performed, investigating how SAW based acoustophoresis can be used to sort micron and submicron polystyrene particles in water.

First, based on the theoretical framework for generating SAWs, designs of IDTs and microfluidic channels were made. 100 µm pitch IDTs and FIDTs were successfully fabricated using photolihography and lift-off microfabrication techniques. For the 50 µm pitch IDTs and FIDTs, microfabrication parameters were optimized to create the micrometer structures needed for these designs, resulting in an optimized fabrication protocol. The designs were as following: 100 µm pitch IDTs (IDT$_A$), 100 µm pitch IDTs with reflectors (IDT$_B$), 100 µm pitch IDTs with reflectors and a longer IDT spacing (IDT$_C$), 50 µm pitch IDTs with reflectors (IDT$_D$), 100 µm pitch FIDTs (FIDT$_A$) and 50 µm pitch SPUDTs (FIDT$_B$).

Second, the frequency response of the different IDT designs was measured using a network analyzer, and the results for the different designs were compared. The resonance frequencies for the straight IDT designs are consistent with the theoretical resonance frequencies within a range of 1.06 MHz. The network analyzer measurements were used to show that the designs respond as predicted, according to the theoretical framework, pointing to a successful fabrication protocol. IDT$_B$ proves to be the most promising design, with a -4.64 dB signal response at its res-

onance frequency. The Frequency Finder software was created to measure the response of IDTs at specific frequencies. The amplitude of the frequency response measured by Frequency Finder are not accurate when compared to the network analyzer, however, all the resonance frequencies measurements are within 1 MHz of the network analyzer measured resonance frequency. Hence, the Frequency Finder software show good abilities in obtaining resonance frequencies for individual devices.

Third, 3.0 µm and 0.5 µm polybead® polystyrene particles were successfully separated using SAW generated acoustophoresis. Using IDT_A with a generated -18dBm 39.2 MHz signal, the different sized polystyrene particles were separated at a flow rate of 40 µL/h for the center particle flow and 60 µL/h for the sheath flow. A double paired IDT_B device successfully separated 3.0 µm from 0.5 µm particles at a generated -22dBm 38.8 MHz signal, and a flow rate of 10 µL/h for the center particle flow and 60 µL/h and 70 µL/h for the right and left sheath flow. For this device the particles were focused both vertically and laterally after moving through the channel, suggesting an additional focusing effect from the focusing IDT_Bs. Separation of 1.0 µm and 0.2 µm fluorescence polystyrene microspheres were further investigated for the double IDT_B device. The SSAW generated acoustic radiation force constructs particle bands of aggregated particles at the pressure nodes, but the degree of separation is not adequate when compared to separation of the 3.0 µm and 0.5 µm particles. Double paired IDT_D devices were fabricated and used to separate 1.0 µm from 0.2 µm fluorescence polystyrene particles, due to its higher resonance frequency. Misalignment of the microfluidic channel with respect to the IDTs, results in offsets in the location of the nodes and anti-nodes, and becomes an obstacle for successful reproducibility of separation devices. This problem is especially present for making successful acoustophoresis devices with 50 µm pitch IDTs, due to the 12.5 µm distance between the nodes and anti-nodes. For these devices a misalignment of only 10 µm changes the function of the entire device, from separating particles to focusing particles.

An emphasis of quantifying the different efficiency of the different designs should be prioritized for further work. Samples from the different outlets should be collected to measure the concentration of the different sized particles measured. Skov's expansion to the LabVIEW program could be taken into use to get quantitative data on separation efficiency for fluorescence particles. In addition, nanoparticle tracking systems could be used to measure the concentration of different particles from outlet samples.

For the device to successfully separate micron sized particles from submicron sized particles, the limitations in alignment accuracy between the microfluidic channel and the IDTs has to be improved. Techniques to improve the alignment were investigated, but no method resulted in a solution to the problem. Further work should go into investigating methods for accurate alignment of the PDMS channel and the IDTs deposited on LiNbO$_3$, for a reproducible product.

When the requirement for a better alignment accuracy have been met, further studies of how the signal amplitude and frequency affects particles of different size should be looked into. The goal for such a study would be to find signal parameters corresponding to specific size cut-offs, filtrating out particles extending a specific size.

This thesis has contributed in the understanding, fabrication and use of SAW acoustophoresis to separate micron and submicron particles. Microfabricational techniques have been used to successfully fabricate acoustophoretic devices for particle separations. The devices show that micron and submicron particles can be successfully separated by using SSAWs, generating pressure fields in microfluidic channels. The device show promising results in separating 3.0 µm particles from 0.5 µmparticles. The main difficulties lie in alignment accuracy, which have shown to be the main challenge when fabricating reproducible separation devices. A method to improve the alignment accuracy have to be implemented to successfully fabricate reproducible devices for micron and submicron particle separation. This work show that 1.0 µm are more easily to manipulate by SAW based acoustophoresis than 0.2 µm particles. However, our results look promising for the use of SAW acoutophoretics as a mean to separate particles by size. This study has demonstrated how SAW based acoustophoresis can be used as a mean to sort and filter out micron sized particles from submicron particles, and its future potential as an on-chip filtration device for POC purposes.

A │ Additional Results

In this appendix, some of the additional results that were obtained during the project are presented.

A.1 Contact Angle Measurement

The optimized oxygen flow rate and plasma power for PDMS-LiNbO$_3$ plasma bonding was found by measuring the hydrophilic properties of plasma treated PDMS. A technique for measuring the contact angle was developed in our group, and is explained in Appendix C. The optimal oxygen flow rate and plasma power, resulting in the lowest contact angle, was found using 50% (0.4 mbar) oxygen and 50 W RF generator power.

A.2 Image Reversal Bake

No specific complications appeared when fabricating the 100 µm pitch IDTs during standard Image Reversal procedure[1] using image reversal photolithography, thin deposition and lift-off. For the 50 µm pitch, the standard method did not produce discontinuous, and well defined, structures for the electrode fingers. To improve fabrication of these fine structures, the effect of different temperatures at the image reversal bake (IRB) step was investigated. The effect of different exposure doses, during image reversal process, was also investigated. The 12.5 µm wide, curved structures of the FIDT$_B$ were chosen since their structure is more complex than the straight structures of IDT$_D$. First, a change in temperature from 112 °C to 114 °C improved the fabrication for several different exposure doses. Microscope images of the result, after the development step, is shown in Figure A.1).

---

[1] Protocol from NTNU NanoLab Process Database, created by Jonas M. Ribe

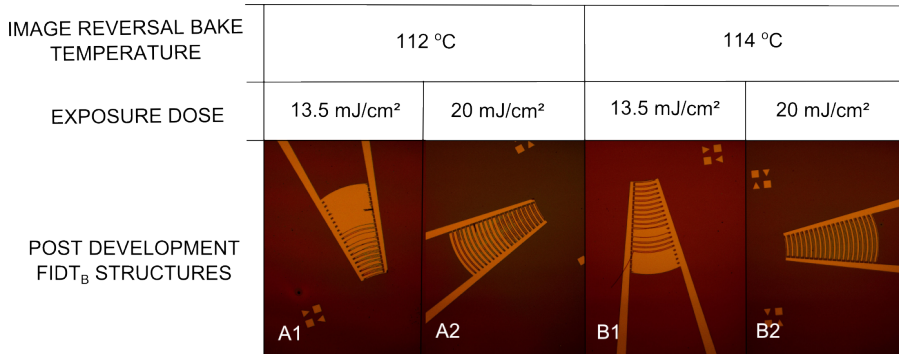| IMAGE REVERSAL BAKE TEMPERATURE	112 ºC		114 ºC	
EXPOSURE DOSE	13.5 mJ/cm²	20 mJ/cm²	13.5 mJ/cm²	20 mJ/cm²
POST DEVELOPMENT FIDT$_B$ STRUCTURES	A1	A2	B1	B2

Figure A.1: **Microscope images, showing the effect of changing image reversal bake temperature and exposure dose during image reversal process for the FIDT$_B$ design: A1** 112 °C Image reversal bake temperature and 13.5 mJ/cm^3 exposure dose, resulting in several pitches in between the electrode fingers that were not developed. **A2** 112 °C Image reversal bake temperature and 20.0 mJ/cm^3 exposure dose. Resulting in better structures where the electrode finger pairs are disconnected from each other. However, the spacing between the thick and thin SPUDT electrode fingers are not developed. **B1** 112 °C Image reversal bake temperature and 13.5 mJ/cm^3 exposure dose, resulting in defined electrode fingers without any observable defects.

Further, different exposure doses were tested using 114 °Cas the IRB temperature. The results are shown in figure A.2, with images of FIDT$_B$ and the uniform IDT$_B$ design for different exposure doses. For the FIDT$_B$ design an exposure dose of 15 mJ/cm^2 resulted in the electrode structures that were not defined, but connected together. Both 30 mJ/cm^2 and 45 mJ/cm^2 show defined structures for the FIDT$_B$ design, however the edge of the structures are not as defined for 45 mJ/cm^2 as for 30 mJ/cm^2. This implies that there is less of an undercut for 45 mJ/cm^2, which might result in a more difficult lift-off. Hence, 30 mJ/cm^2 was chosen as the optimal exposure dose. It should be noted that all dosages gave well defined structures and successful development for the uniform IDT$_B$ design.

These parameters were used to the fabricate the IDT$_B$ (shown in Figure A.2), IDT$_C$, IDT$_D$ and FIDT$_B$ designs that were tested in the network analyzer. The results from the network analyzer indicate that these parameters produce reproducible and well-working IDTs, and the new parameters were implemented as a general protocol for fabrication of all IDT designs on LiNbO$_3$.
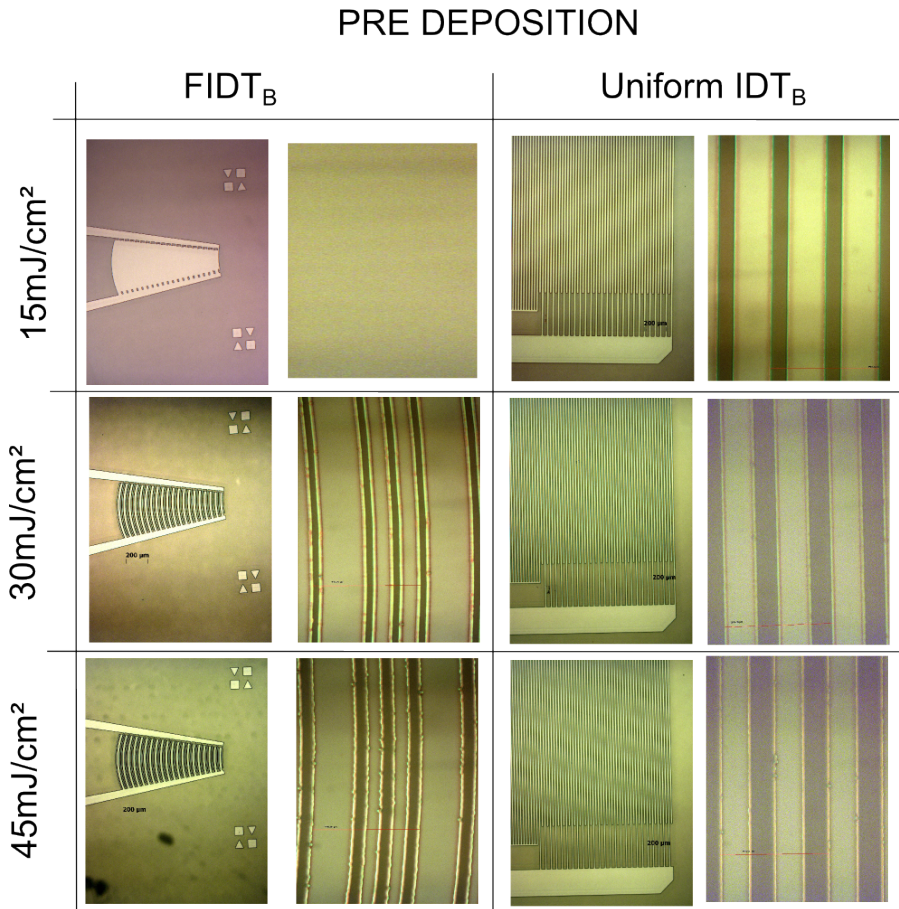
Figure A.2: **Microscope Images, Showing the Effect of Different Exposure Dose**
Microscope images, taken with 5X and 10X objectives, are shown of the curved
$FIDT_B$ design and the uniform IDT_B design after development for 3 different exposure dosages. At 15 mJ/cm^2 the FIDT structures are not defined, but all electrode fingers are connected. For 30 mJ/cm^2 exposure doses the 12.5 μm wide FIDT structures are well defined and successfully developed. When using 45 mJ/cm^2 dosage the structures are also defined, however the edge of the electrode fingers are not as straight as when using a 30 mJ/cm^2 dosage. In addition the edge looks thinner, implying that the undercut is less defined or straighter than with the 30 mJ/cm^2 dosage. The uniform IDT_B structures, with 25 μm wide electrodes, are defined and succesfully developed for all exposure doses.

Table A.1: The difference in length from the center of the channel to the IDT on each side of the channel is calculated from measurements in figure A.3.

	3.2 mm IDT	5.2 mm IDT	5.2 mm IDT
With alignment structures	55μmm	19μmm	48μmm
Without alignment structures	12μmm	65μmm	23μmm

A.3 Alignment

Alignment marks were used to align the PDMS channel and the IDT pairs on the LiNbO$_3$ during plasma bonding. For the regular alignment technique, a couple of drops of ethanol is applied to the LiNbO$_3$ directly after plasma treatment. The PDMS channel is placed on top, with a thin separation layer of ethanol in between. The sample is placed under a Nikon C–PS microscope and the PDMS channel is moved around until the alignment marks align on both pieces. The PDMS is then held in place by hand until the ethanol is evaporated, and the plasma bonding takes place. To evaporate any excess ethanol, the two pieces are put in an oven at 65 °C for 30 minutes.

An additional technique for alignment was tested to improve the alignment precision. After a successful lift-off, the LiNbO$_3$ wafer is cleaned with acetone, ethanol and plasma rinse, before spincoated with SU-8 2050. SU-8 structures are created on top of the triangular alignment marks, using photolithography. No adhesion promoters (like HMDS) were needed for the SU-8 structures to stick to the LiNbO$_3$ wafer. The height of the structures corresponds with the depth of the inverse alignment mark structure in the PDMS channel. When aligning the PDMS channel to the LiNbO$_3$ under the microscope, the SU-8 alignment structures on the LiNbO$_3$ can fit into the inverse alignment structure in the PDMS. Hence, improving alignment of the two pieces. Figure A.3 compares microscope images of devices aligned with and without using additional SU-8 alignment structures. Both devices consists of two IDT$_B$ pairs, and a 60 μm channel.

The distances from the IDTs to the channel feature, shown in Figure A.3, are listed in Table A.1. These measurement are obtained using a ZEISS microscope with a 5X objective and AxioVision Rel. 4.7 software.

According to the results shown in Figure A.3, the additional SU-8 structures for improved alignment of the PDMS channel and the IDTs had no significant effect. Table A.1 show that the best alignment accuracy was found when alignment was executed without any SU-8 structures. There is no reason to conclude that align-
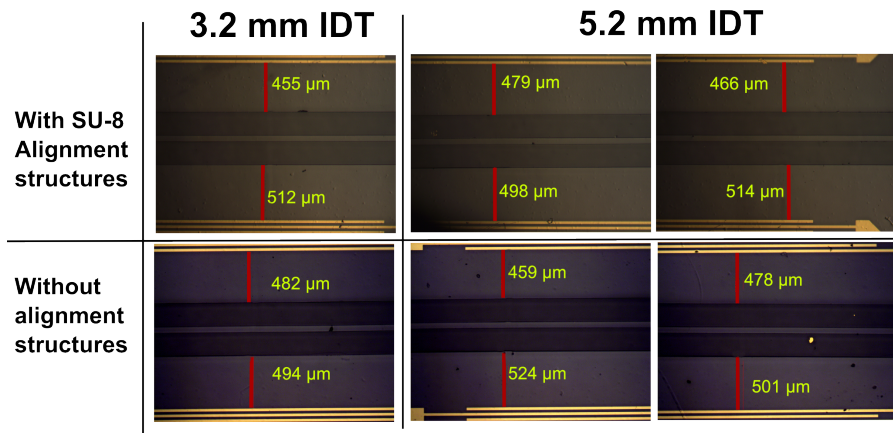
Figure A.3: **Alignment With and Without SU-8 Alignment Structures**
The distances from the IDTs to the PDMS feature is shown for two devices, measured using a ZEISS microscope with a 5X objective and Carl Zeiss AxioVision Rel. 4.7 software. Both are of the two paired IDT$_B$ design and are aligned with a 60 μm PDMS channel. There is one measurement for the 3.2 mm long IDT and two measurements for the 5.2 mm long IDT.

ment features have no effect, only that there was no effect documented for our design. To improve alignment, more alignment structures could be added to achieve the click effect between the layers. The structures should also be located closer to the channel, since the alignment accuracy is most important in between the IDTs. However, adding more features close to the channel would not be possible without affecting the SAWs traduced from the IDTs.

A more stiff PDMS can be created with a 7:1 or 5:1 ratio of PDMS and curing agent. The devices in which alignment accuracy measurements are shown in Figure 7.13 and Figure 7.20 are from PDMS with a 7:1 ratio. The alignment for these devices show no significance alignment accuracy due to a stiffer PDMS.

In Figure 7.14 and Figure 7.15 PDMS channels are made from a 5:1 ratio. Instead of curing at 65°C for 2 hours the PDMS was cured at 45 °C for 6 hours. This to reduce the curing shrinking rate of the PDMS, which increases with temperature. These PDMS micro channels were easier to align with the alignment marks on the LiNbO$_3$, and not much force was needed to keep the alignment in place until the ethanol had evaporated, compared the other PDMS to curing agent ratios. The alignment accuracy was measured for both devices (not presented), but there was no trend towards a significant improvement in misalignment. The change in misalignment throughout the length of the channel was measured to 11 μm for the

device presented in Figure 7.15 and 15 µm for the device presented in Figure 7.14. This implies that the PDMS is less flexible for this PDMS to curing agent ratio. However, there was an alignment offset between the microfluidic channel and the IDTs of approximately 50 µm for both devices. Hence, the alignment error have not improved even though the PDMS is stiffer.

Parts of the PDMS, on either side of the channel, have to be cut away to expose the pads for wire bonding. The wedge bonding needle will not be able to get in contact with the pads if not enough PDMS is removed. For a future design the structure of the IDT bonding pads should be changed so that less PDMS needs to be removed close to the side of the channel.

B | Fabrication Protocols

Fabrication of SAW electrodes on LiNbO$_3$ wafer

Photolithography, thin film deposition and lift-off were done in a ISO-7 clean room, while techniques involving PDMS and the plasma cleaner were done in a ISO-5 clean room.

1. Clean 2" LiNbO$_3$ Wafer:

Wash with Acetone and IPA, before drying with N_2(g).

Treat with oxygen plasma: 50/50 (50 % O_2 oxygen flow/50 W RF Power) for 5 min.

Evaporation bake: 105 °C for 5 min.

2. Spin-coat resist: Resist: AZ 5214 E.

1.4 µm layer of resist: 4000 rpm for 46 s, with a ramp speed of 4000 r/s^2.

Remove any edge bead with ethanol.

3. Softbake:

96 °C for 90 s.

4. Exposure:

A chrome mask is used in a MA6 Maskaligner, using

Photolithography, Hard contact, 50 µm alignment gap.

30 mJ/cm^2 exposure.

5. Image-reversal bake:

112 °C for 120 s.

6.Flood Exposure:

200 mJ/cm^2.

7. Develop:

Developer: AZ726 MIF.

Rinse sample carefully in developer for 40 s.

Rinse with DI and dry with $N_2(g)$.

8. E-beam Evaporation of Ti and Au:

Deposit 5 nm Ti (1 Å/s) and 80 nm Au (5 Å/s).

9. Lift-off and scribing:

Perform lift-off using Acetone and IPA.

Scribe wafer into single SAW electrode devices,

and wash with ethanol before drying with $N_2(g)$.

Scribing can also be performed prior to step 1.

Glass-slide with Au electrodes

1. Clean glass-slide:

Wash with Acetone, IPA and dry with $N_2(g)$.

Plasma cleaner: O_2, 50/50 for 5 min.

2. Tape mask:

Create a mask layer using scotch tape. Leave the areas where the electrodes
are to be deposited clean of tape.

3. E-beam Evaporation of Ti and Au:

Deposit 50 nm Ti (1 Å/s) and 200 nm Au (5 Å/s).

Remove tape, leaving only the metal that is deposited straight on to the glass
slide.

Solder coax plug to Au electrode on glass-slide

Connect female SMA plugs to the Au electrodes on the glass slides for signal inlets
by solder a connection between the signal electrode and the ground electrodes.

Fabrication of Microfluidic Master Mold

1. Clean Si wafer:

Wash with Acetone and IPA, before drying with $N_2(g)$.

Treat with oxygen plasma: 50/50, for 5 min.

Evaporation bake: 110 °C for 5 min.

2. Spin-coat resist:

Photoresist: SU-8 3000.

For a 5 μm layer of resist:

Step 1: 500 rpm for 10 s, with a ramp speed of 250 r/s^2 for 2 s.

Step 2: 2500 rpm for 40 s, with a ramp time of 11 s.

Remove any edge bead using ethanol.

3. Softbake:

95 °C for 15 min.

4. Exposure:

Hard contact, 50 µm alignment gap.

36 mJ/cm^2.

5. Postbake:

65 °C for 60 s.

95 °C for 5 min.

6. Developing:

Developer: MR-DEV 600.

Rinse gently wafer with SU-8 in developer for 4 min, until the structures
are clearly visible.

Rinse in a separate container with developer for 10 s.

Wash with IPA and dry with N_2(g).

7. Silanize wafer:

Put SU-8 mold into desiccator, together with a drop of silane
in a container, turn on and leave for 15 min. Close valve
for vacuum inlet, turn off vacuum and leave for at least 30 min.

Fabricating PDMS microchannels

1. Mix PDMS:

Mix PDMS from Dow Corning's Sylgard 184 two component silicone elastomer
kit with a ratio of 1:10 curing agent (cross-linker) to base (elastomer)
measured using a digital scale. Stirr using a plastic spoon for >5 min.

2. Degas:

Put silanized SU-8 mold in a small petri dish
and pour the PDMS onto the wafer. Put in desiccator
for 30–40 min to remove any bubbles in the PDMS.

3. Bake

Bake for 2 hours at 65 °C.

4. Cut devices out of PDMS:

Cut out the devices of the cured PDMS with a scalpel,
and use a 1.0 µm puncher to punch holes for inlets
and outlets. Remove any PDMS debris device using Scotch tape.

Bond PDMS to SAW device

Put PDMS channel and $LiNbO_3$ containing IDTs into the plasma cleaner, 50/20 for 24 s. Put a drop of ethanol onto the $LiNbO_3$ surface and roughly align PDMS channel on top. Use a microscope to align the features. Put in a oven at 65 °C for 30 min.

Fasten Device to Signal Mount

Use small pieces of double sided Scotch tape to attach the device to the transparent middle part of the Signal Mount not covered with electrodes. Use wedge bonding to wire bond the Au electrode on the glass-slide to the SAW Au electrodes on the $SiNbO_3$ wafer.

C | Manuscript: Contact Angle Measurements Submitted to Chips and Tips

The following manuscript is submitted to Chips and Tips, a forum forum for scientists in the miniaturisation field from the journal Lab on a Chip. The manuscript describes how a PDMS macro lens can be fabricated and used, together with a smartphone, to measure contact angles. This technique was used to obtain the optimal oxygen flow rate and plasma power for plasma bonding, by measuring the contact angle of a drop of water on plasma treated PDMS.

Simple and Low-cost Contact Angle Measurements Using a Smartphone with a PDMS-Lens

Jonas M. Ribe[a], Nils R. Skov[b], Ole-Andreas K. Kavli[a], Armend G. Håti[a], Henrik Bruus[b] and Bjørn T. Stokke[a]

[a] Department of Physics, Norwegian University of Science and Technology, NO–7491 Trondheim, Norway

[b] Department of Physics, Technical University of Denmark, DK–2800 Kongens Lyngby, Denmark

jonas.ribe@ntnu.no

Why Is This Useful?

Contact angle measurements are important for characterizing the wettability of a liquid to a solid surface. In microfluidics they are of special interest as they provide insight into the intermolecular interactions between the sample liquid and the microchannel surface. Contact angle measurements are also important when assembling polydimethylsiloxane (PDMS) devices using oxygen plasma bonding. For optimal bond strength the water contact angle of plasma treated PDMS should be minimized as shown by Bhattacharya S. *et al*.[1] A current hurdle in measuring contact angles is the requirement of a setup that is expensive and non-portable. Here we show a method for measuring contact angles using materials and equipment found in a typical microfluidics lab.

What do I need?

Consumables:
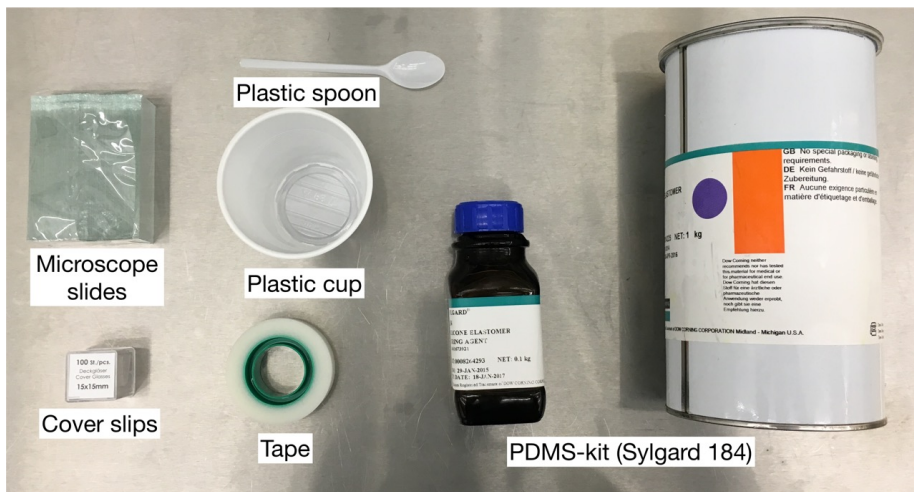
Equipment:

- Smartphone
- Digital scale
- Desiccator with vacuum pump
- Oven
- Syringe pump (*optional*)
- Light source

For measurements:

- Pipette (0.5–3µL)
- Sample (e.g. deionized (DI) water or other liquid sample)

**What do I do?**

Prepare PDMS:

1. Weigh 10:1 PDMS (Sylgard 184) in a plastic cup on the digital scale
2. Mix the PDMS by hand using a plastic spoon
3. Degas the PDMS in a desiccator to remove the bubbles

Make PDMS-lens:

Put drop of PDMS on a cover slip | Cure upside down | Cured PDMS-lens | Mount over smartphone camera
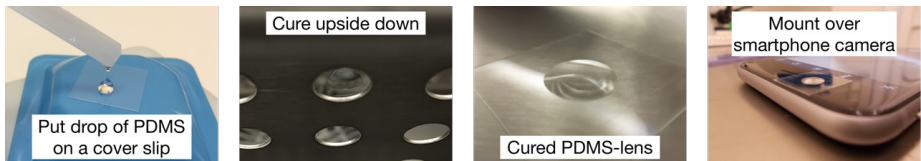
1. Use the tip of the plastic spoon handle (or a pipette) to place a small droplet of uncured PDMS in the center of a glass cover slip. Repeat with various amounts of PDMS to obtain lenses with varying magnification.
2. Mount the cover slips upside down (e.g. between two glass slides) and cure the PDMS hanging at 70°C for 15min. Longer curing times might be necessary, if the drop is relatively large .
3. Center the PDMS-lens over the camera of your smartphone and fixate it using tape.
4. Test the focus of your camera. For our camera setup the best images were captured with lenses that focus around 2cm.
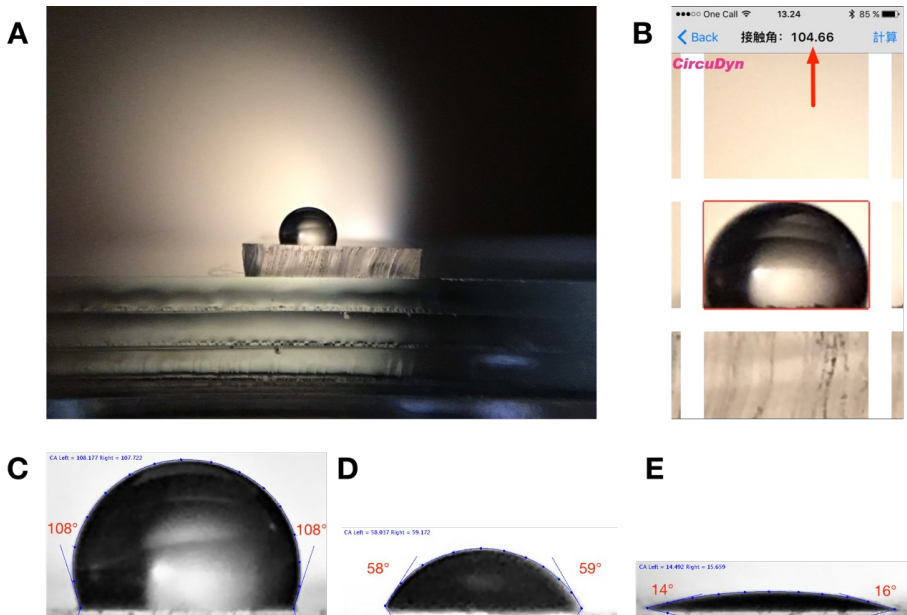
Contact angle measurements:
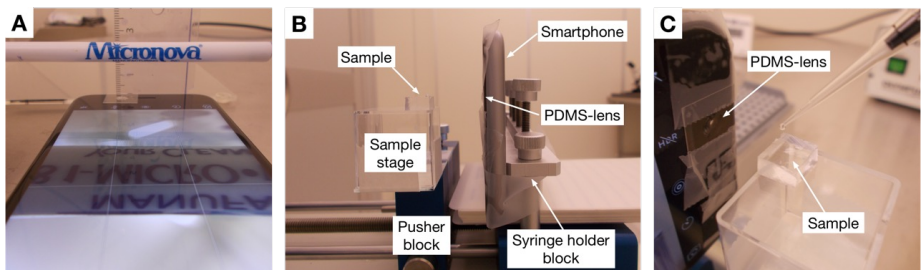
Smartphone contact angle setup: A: Focus test of PDMS lens. **B:** Smartphone mounted on syringe pump. The PDMS-lens is mounted on the front facing camera of an iPhone 6S and the sample is centered in front of the lens. The sample is mounted on the pusher block of a syringe pump which can be moved to adjust the focus.

1. Make a sample stage preferably using a syringe pump or some other system you can move. We mounted the smartphone on the syringe holder block with the camera pointing towards the pusher block. Make a sample holder on the pusher block using glass slides or other consumables found in the lab. Align the center of the stage with the center of the camera. *Tip: aligning is easier if done using the sample you want to measure. Put the sample on the block and move it into focus by releasing the pusher block and sliding it away/towards the camera. Increase the height of the stage until the top of the sample is centered in the camera.*
2. Place the light source behind the sample and illuminate the stage evenly. *Tip: put the sample stage in front of a white wall and light up the wall for a homogenous background and optimal contrast.*
3. Place a small drop (0.5–3µL) of DI water on top of the sample using a pipette. Place the drop near the sample edge closest to the camera.
4. Move the sample edge into focus. Block out ambient light in the room.
5. Measure the contact angle of the drop in the image e.g. using ImageJ[2] software with a plugin for contact angle

measurements[3] or get a rough estimate using an app on your smartphone.[4]

Contact angle measurements of water on PDMS: A) Raw image from iPhone 6S front-facing camera with PDMS-lens. B) Direct measurement using app on smartphone (based on θ/2 calculation) C-E) ImageJ measurements using DropSnake plugin. Unmodified PDMS (C) and PDMS treated with oxygen plasma with increasing intensity(D-E).

What else should I know?

The focal length of the PDMS-lens is determined by the volume of PDMS used as described by Lee *et al*.[5] However, it is difficult to control the volume of PDMS using a pipette due to the high viscosity of PDMS. We recommend making a range of lens sizes and testing them on your smartphone camera to see which gives the right focal length. If your digital scale has milligram precision you can measure the amount of PDMS used for each lens. The mass of each PDMS-lens is typically less than 10mg. You can decrease the focal length further by adding PDMS to an already cured lens. Modern smartphones have both a rear-facing and a front-facing camera and in our experience the drop focusing was easier when using the front facing camera. The images taken here were captured with an iPhone 6S from Apple using the front-facing camera with a 5MP sensor. The weight of the cured PDMS lens was 7mg.

Tip: you can also remove the PDMS-lens from the cover slip and place it directly on your camera. Although, it might be more difficult to center.

Calculating contact angles from images of sessile drops can be done using a range of techniques.[6] If the drop volume is small and the contact angles are not extreme, we can generally neglect droplet distortion due to gravitational effects. Extrand and Moon[7] calculated that gravitational effects can be neglected for a water droplet sitting on a hydrophilic surface (θ=5°) if its volume is less than 5μL and less than 2.7μL on a hydrophobic surface (θ=160°). If we assume the drop to be spherical, the contact angle can be estimated by multiplying the angle between the base and the height of the droplet by 2. This is referred to as the θ/2-method and is implemented by e.g. the Contact Angle Measurement app[4] for iOS. Sessile drop measurements are generally limited by the experimental setup and operator error, but typically has a precision of ±3°.[8] Image-processing algorithms relying on curve fitting of the droplet outline can enhance reproducibility. ImageJ[2] with DropSnake-plugin[3] uses active contours (energy minimization) to track the outline of the drop and calculate contact angles. This increases precision, but is slower and currently requires analysis on a separate computer.

References

1. S. Bhattacharya, A. Datta, J. M. Berg and S. Gangopadhyay, *J. Microelectromech. S.*, 2005 **14**, 590–597

2. ImageJ software

3. DropSnake ImageJ-plugin for contact angle measurements

4. Contact Angle Measurement iOS app (*Japanese*)

5. W. M. Lee, A. Upadhya, P. J. Reece, and T. G. Phan, *Biomed. Opt. Express*, 2014, **5**, 1626–1635

6. Y. Yuan and T. R. Lee, *Surface Science Techniques*, Springer, Berlin/Heidelberg, 2013, **51**, 3–34.

7. C. W. Extrand and S. I. Moon, *Langmuir*, 2010, **26**, 11815–11822.

8. A.F. Stalder, G. Kulik, D. Sage, L. Barbieri and P. Hoffmann, *Colloids and Surfaces A: Physicochem. Eng. Aspects*, 2006, **286**, 92–103.

Bibliography

[1] Ju-Hee Kang, Brit Mollenhauer, Christopher S Coffey, Jon B Toledo, Daniel Weintraub, Douglas R Galasko, David J Irwin, Vivianna Van Deerlin, Alice S Chen-Plotkin, Chelsea Caspell-Garcia, et al. Csf biomarkers associated with disease heterogeneity in early parkinson's disease: the parkinson's progression markers initiative study. *Acta Neuropathologica*, pages 1–15, 2016.

[2] Raghu Kalluri. The biology and function of exosomes in cancer. *Journal of Clinical Investigation*, 126(4):1208–1215, 04 2016.

[3] Douglas D. Taylor and Cicek Gercel-Taylor. Microrna signatures of tumor-derived exosomes as diagnostic biomarkers of ovarian cancer. *Gynecologic Oncology*, 110(1):13 – 21, 2008.

[4] Alexander V. Vlassov, Susan Magdaleno, Robert Setterquist, and Rick Conrad. Exosomes: Current knowledge of their composition, biological functions, and diagnostic and therapeutic potentials. *Biochimica et Biophysica Acta (BBA) - General Subjects*, 1820(7):940 – 948, 2012.

[5] Benoit Fevrier, Didier Vilette, Fabienne Archer, Damarys Loew, Wolfgang Faigle, Michel Vidal, Hubert Laude, and Graça Raposo. Cells release prions in association with exosomes. *Proceedings of the National Academy of Sciences of the United States of America*, 101(26):9683–9688, 2004.

[6] Taixue An, Sihua Qin, Yong Xu, Yueting Tang, Yiyao Huang, Bo Situ, Jameel Inal, and Lei Zheng. Exosomes serve as tumour markers for personalized diagnostics owing to their important role in cancer metastasis. *Journal of Extracellular Vesicles*, 4(0), 2015.

[7] Xi Chen, Yi Ba, Lijia Ma, Xing Cai, Yuan Yin, and more. Characterization of microRNAs in serum: a novel class of biomarkers for diagnosis of cancer and other diseases. *Cell Res*, 18(10):997–1006, oct 2008.

[8] Dali Zheng, Shadi Haddadin, Yong Wang, Li-Qun Gu, Michael C Perry, Carl E Freter, and Michael X Wang. Plasma micrornas as novel biomarkers for early detection of lung cancer. *Int J Clin Exp Pathol*, 4(6):575–586, 2011.

[9] Lesley Cheng, Robyn A Sharples, Benjamin J Scicluna, and Andrew F Hill. Exosomes provide a protective and enriched source of mirna for biomarker profiling compared to intracellular and cell-free blood. *Journal of extracellular vesicles*, 3, 2014.

[10] Cancer statistics, 1996. "http://onlinelibrary.wiley.com/doi/10.3322/canjclin.46.1.5/full", 2010.

[11] TriMark Publications. Point of care diagnostic testing world markets. Technical report, April 2016.

[12] *Microfluidics Market by Material (Polymer, Glass, Silicon) Application (Pharmaceutical (Genomics, Proteomics, Capillary Electrophoresis) Diagnostic (Clinical, Environmental, Industrial) Drug Delivery (Inhaler, Micropump)) - Global Forecast to 2020*. Research and Markets, 2015.

[13] Andrea W. Chow. Lab-on-a-chip: Opportunities for chemical engineering. *AIChE Journal*, 48(8):1590–1595, 2002.

[14] Klavs F Jensen. Microreaction engineering—is small better? *Chemical Engineering Science*, 56(2):293–303, 2001.

[15] Vladimir Gubala, Leanne F Harris, Antonio J Ricco, Ming X Tan, and David E Williams. Point of care diagnostics: status and future. *Analytical chemistry*, 84(2):487–515, 2011.

[16] Joseph Wang. Electrochemical biosensors: towards point-of-care cancer diagnostics. *Biosensors and Bioelectronics*, 21(10):1887–1892, 2006.

[17] Shailender Singh Kanwar, Christopher James Dunlay, Diane M Simeone, and Sunitha Nagrath. Microfluidic device (exochip) for on-chip isolation, quantification and characterization of circulating exosomes. *Lab on a Chip*, 14(11):1891–1900, 2014.

[18] Zheng Zhao, Yang Yang, Yong Zeng, and Mei He. A microfluidic exosearch chip for multiplexed exosome detection towards blood-based ovarian cancer diagnosis. *Lab Chip*, 16:489–496, 2016.

[19] Mei He, Jennifer Crow, Marc Roth, Yong Zeng, and Andrew K Godwin. Integrated immunoisolation and protein analysis of circulating exosomes using microfluidic technology. *Lab on a Chip*, 14(19):3773–3780, 2014.

[20] A Liga, ADB Vliegenthart, W Oosthuyzen, JW Dear, and M Kersaudy-Kerhoas. Exosome isolation: a microfluidic road-map. *Lab on a Chip*, 15(11):2388–2394, 2015.

[21] Aaron M Streets and Yanyi Huang. Chip in a lab: Microfluidics for next generation life science research. *Biomicrofluidics*, 7(1):011302, 2013.

[22] Timothy A Crowley and Vincent Pizziconi. Isolation of plasma from whole blood using planar microfilters for lab-on-a-chip applications. *Lab on a Chip*, 5(9):922–929, 2005.

[23] J. de Jong, R. G. H. Lammertink, and M. Wessling. Membranes and microfluidics: a review. *Lab Chip*, 6:1125–1139, 2006.

[24] Jun Ho Son, Sang Hun Lee, Soongweon Hong, Seung-min Park, Joseph Lee, Andrea M Dickey, and Luke P Lee. Hemolysis-free blood plasma separation. *Lab on a Chip*, 14(13):2287–2292, 2014.

[25] Kerwin Kwek Zeming, Nitish V Thakor, Yong Zhang, and Chia-Hung Chen. Real-time modulated nanoparticle separation with an ultra-large dynamic range. *Lab on a Chip*, 16(1):75–85, 2016.

[26] Jonathan D. Adams and H. Tom Soh. Tunable acoustophoretic band-pass particle sorter. *Applied Physics Letters*, 97(6), 2010.

[27] Patrick Thévoz, Jonathan D Adams, Herbert Shea, Henrik Bruus, and H Tom Soh. Acoustophoretic synchronization of mammalian cells in microchannels. *Analytical chemistry*, 82(7):3094–3098, 2010.

[28] Filip Petersson, Lena Åberg, Ann-Margret Swärd-Nilsson, and Thomas Laurell. Free flow acoustophoresis: microfluidic-based mode of particle and cell separation. *Analytical chemistry*, 79(14):5117–5123, 2007.

[29] Rune Barnkob. Physics of microparticle acoustophoresis. 2012.

[30] Ghulam Destgeer, Byung Hang Ha, Jin Ho Jung, and Hyung Jin Sung. Submicron separation of microspheres via travelling surface acoustic waves. *Lab on a Chip*, 14(24):4665–4672, 2014.

[31] Jinjie Shi, Hua Huang, Zak Stratton, Yiping Huang, and Tony Jun Huang. Continuous particle separation in a microfluidic channel via standing surface acoustic waves (ssaw). *Lab on a Chip*, 9(23):3354–3359, 2009.

[32] Brian Kirby. *Micro- and Nanoscale Fluid Mechanics*. Cambridge University Press (CUP), 2009.

[33] JP Holman. Heat transfer, 9th, 2002.

[34] John William Strutt. On waves propagated along the plane surface of an elastic solid. *Proceedings of the London Mathematical Society*, 17(1):4–11, 1885.

[35] Velimir M Ristic. *Principles of acoustic devices*. John Wiley & Sons, Inc., 1983.

[36] Michael Gedge and Martyn Hill. Acoustofluidics 17: Theory and applications of surface acoustic wave devices for particle manipulation. *Lab on a Chip*, 12(17):2998, 2012.

[37] A.V. Mamishev, K. Sundara-Rajan, Fumin Yang, Yanqing Du, and M. Zahn. Interdigital sensors and transducers. *Proceedings of the IEEE*, 92(5):808–845, may 2004.

[38] Richard M White. Surface elastic waves. *Proceedings of the IEEE*, 58(8):1238–1276, 1970.

[39] J.J. Campbell and W.R. Jones. A method for estimating optimal crystal cuts and propagation directions for excitation of piezoelectric surface waves. *IEEE Transactions on Sonics and Ultrasonics*, 15(4):209–217, oct 1968.

[40] Colin Campbell. *Surface acoustic wave devices for mobile and wireless communications*. Academic press, 1998.

[41] PV Wright. The natural single-phase unidirectional transducer: a new low-loss saw transducer. In *IEEE 1985 Ultrasonics Symposium*, pages 58–63. IEEE, 1985.

[42] C Hartmann, P Wright, E Garber, and R Kansy. An analysis of saw interdigital transducers with internal reflections and the application to the design of single-phase unidirectional transducers. *IEEE 1982 Ultrasonics Symposium*, pages 40–45.

[43] Kimio Shibayama, K. Yamanouchi, H. Sato, and T. Meguro. Optimum cut for rotated y-cut linbo3crystal used as the substrate of acoustic-surface-wave filters. *Proceedings of the IEEE*, 64(5):595–597, May 1976.

[44] Jinjie Shi, Shahrzad Yazdi, Sz-Chin Steven Lin, Xiaoyun Ding, I-Kao Chiang, Kendra Sharp, and Tony Jun Huang. Three-dimensional continuous particle focusing in a microfluidic channel via standing surface acoustic waves (ssaw). *Lab on a Chip*, 11(14):2319–2324, 2011.

[45] Nitesh Nama, Rune Barnkob, Zhangming Mao, Christian J Kähler, Francesco Costanzo, and Tony Jun Huang. Numerical study of acoustophoretic motion of particles in a pdms microchannel driven by surface acoustic waves. *Lab on a Chip*, 15(12):2700–2709, 2015.

[46] Nils Refstrup Skov. Surface acoustic waves in microfuidic devices: Simulation and instrumentation. Master's thesis, Technical University of Denmark, 3 2016.

[47] Martyn Hill and Nicholas R Harris. Ultrasonic particle manipulation. In *Microfluidic technologies for miniaturized analysis systems*, pages 357–392. Springer, 2007.

[48] Steven M Woodside, Bruce D Bowen, and James M Piret. Measurement of ultrasonic forces for particle–liquid separations. *AIChE journal*, 43(7):1727–1736, 1997.

[49] H Lorenz, M Despont, N Fahrni, N LaBianca, P Renaud, and P Vettiger. Su-8: a low-cost negative resist for mems. *Journal of Micromechanics and Microengineering*, 7(3):121, 1997.

[50] Microchem. *Datasheet SU–8 3000, Permanent Epoxy, Negative Photoresist*.

[51] J Liu, B Cai, J Zhu, G Ding, X Zhao, C Yang, and D Chen. Process research of high aspect ratio microstructure using su-8 resist. *Microsystem Technologies*, 10(4):265–268, 2004.

[52] Suman Mitra and Sushanta K. Chakraborty. *Microfluidics and Nanofluidics Handbook: Fabrication, Implementation, and Applications*, chapter 8.2, pages 233–238. CRC Press, 2011. ISBN:978-1-4398-1672-1.

[53] Younan Xia and George M. Whitesides. Soft lithography. *Angewandte Chemie International Edition*, 37(5):550–575, 1998.

[54] KSKS Sree Harsha. *Principles of vapor deposition of thin films*, chapter 5.2, page 368. Elsevier, 1 edition, 2005.

[55] Microchemicals. *Lift-off Processes with Photoresists*.

[56] Seok Woo Lee and Seung S. Lee. Shrinkage ratio of PDMS and its alignment method for the wafer level process. *Microsystem Technologies*, 14(2):205–208, may 2007.

[57] W Petasch, B Kegel, H Schmid, K Lendenmann, and H.U Keller. Low-pressure plasma cleaning: a process for precision cleaning applications. *Surface and Coatings Technology*, 97(1–3):176 – 181, 1997.

[58] David C. Duffy, J. Cooper McDonald, Olivier J. A. Schueller, , and George M. Whitesides*. Rapid prototyping of microfluidic systems in poly(dimethylsiloxane). *Analytical Chemistry*, 70(23):4974–4984, 1998. PMID: 21644679.

[59] MMR Howlader, T Suga, and MJ Kim. Room temperature bonding of silicon and lithium niobate. *Applied physics letters*, 89(3):31914–31914, 2006.

[60] Shantanu Bhattacharya, Arindom Datta, J.M. Berg, and S. Gangopadhyay. Studies on surface wettability of poly(dimethyl) siloxane (pdms) and glass under oxygen-plasma treatment and correlation with bond strength. *Microelectromechanical Systems, Journal of*, 14(3):590–597, June 2005.

[61] Say Hwa Tan, Nam-Trung Nguyen, Yong Chin Chua, and Tae Goo Kang. Oxygen plasma treatment for reducing hydrophobicity of a sealed polydimethylsiloxane microchannel. *Biomicrofluidics*, 4(3):032204, 2010.

[62] Zhangming Mao, Yuliang Xie, Feng Guo, Liqiang Ren, Po-Hsun Huang, Yuchao Chen, Joseph Rufo, Francesco Costanzo, and Tony Jun Huang. Experimental and numerical studies on standing surface acoustic wave microfluidics. *Lab Chip*, 16(3):515–524, 2016.

[63] S. K. R. S. Sankaranarayanan and V. R. Bhethanabotla. Numerical analysis of wave generation and propagation in a focused surface acoustic wave device for potential microfluidics applications. *IEEE Transactions on Ultrasonics, Ferroelectrics, and Frequency Control*, 56(3):631–643, March 2009.

[64] Minicircuits, P.O. Box 350166, Brooklyn, NY 11235-0003. *ZHl-5W-1: Coaxial High Power Amplifier*.